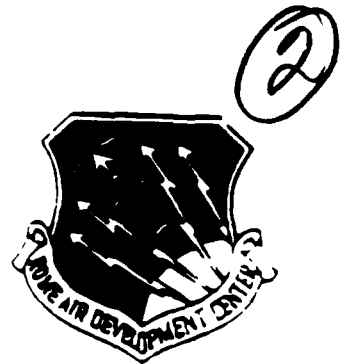


RADC-TR-90-256
Final Technical Report
August 1990

AD-A227 163

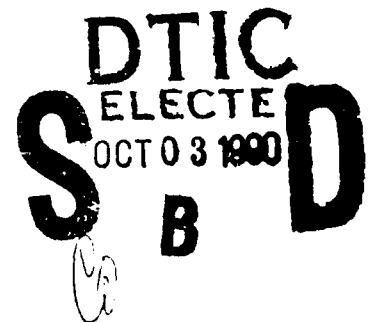


HYBRID OPTICAL PROCESSOR

Dove Electronics, Inc.

J.F. Dove, F.T. S. Yu, C. Eldering

APPROVED FOR PUBLIC RELEASE; DISTRIBUTION UNLIMITED.



Rome Air Development Center
Air Force Systems Command
Griffiss Air Force Base, NY 13441-5700

This report has been reviewed by the RADC Public Affairs Division (PA) and is releasable to the National Technical Information Service (NTIS). At NTIS it will be releasable to the general public, including foreign nations.

RADC-TR-90-256 has been reviewed and is approved for publication.

APPROVED:



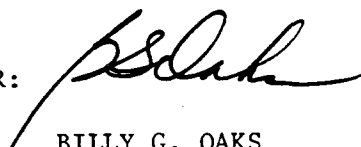
PETER D. GIANINO
Project Engineer

APPROVED:



HAROLD ROTH
Director of Solid State Sciences

FOR THE COMMANDER:



BILLY G. OAKS
Directorate of Plans & Programs

If your address has changed or if you wish to be removed from the RADC mailing list, or if the addressee is no longer employed by your organization, please notify RADC (ESO) Hanscom AFB MA 01731-5000. This will assist us in maintaining a current mailing list.

Do not return copies of this report unless contractual obligations or notices on a specific document require that it be returned.

REPORT DOCUMENTATION PAGE			Form Approved OPM No. 0704-0188	
<small>Public reporting burden for this collection of information is estimated to average 1 hour per response, including the time for reviewing instructions, searching existing data sources, gathering and maintaining the data needed, and reviewing the collection of information. Send comments regarding this burden estimate or any other aspect of this collection of information, including suggestions for reducing the burden, to Washington Headquarters Services, Directorate for Information Operations and Reports, 1215 Jefferson Davis Highway, Suite 1204, Arlington, VA 22202-4302, and to the Office of Information and Regulatory Affairs, Office of Management and Budget, Washington, DC 20503.</small>				
1. AGENCY USE ONLY (Leave Blank)		2. REPORT DATE August 1990		3. REPORT TYPE AND DATES COVERED Final Jul 87 - Jul 90
4. TITLE AND SUBTITLE HYBRID OPTICAL PROCESSOR			5. FUNDING NUMBERS C - F19628-87-C-0086 PE - 61102F PR - 2305 TA - J7 WU - 32	
6. AUTHOR(S) J.F. Dove, F.T.S. Yu, C. Eldering				
7. PERFORMING ORGANIZATION NAME(S) AND ADDRESS(ES) Dove Electronics, Inc. 227 Liberty Plaza Rome NY 13440			8. PERFORMING ORGANIZATION REPORT NUMBER N/A	
9. SPONSORING/MONITORING AGENCY NAME(S) AND ADDRESS(ES) Rome Air Development Center (ESO) Hanscom AFB MA 01731-5000			10. SPONSORING/MONITORING AGENCY REPORT NUMBER RADC-TR-90-256	
11. SUPPLEMENTARY NOTES RADC Project Engineer: Peter D. Gianino/ESO/(617) 377-5119				
12a. DISTRIBUTION/AVAILABILITY STATEMENT Approved for public release; distribution unlimited.			12b. DISTRIBUTION CODE	
13. ABSTRACT (Maximum 200 words) Recent advances of programmable spatial light modulators (SLM) have permitted the synthesis of hybrid signal processors for various computational needs. In accordance with this research program we have developed and synthesized various types of hybrid optical architectures capable of performing tasks such as: multiple matrix computation, hybrid optical computing, optical binary adder, optical perfect shuffle, application of associative memory to symbolic substitution, acousto optic joint transform correlator for space integration and frequency shift keying applications, hard clipping joint transform correlator, and programmable multichannel optical correlator for automatic scanning image detection. The basic architecture of these hybrid optical processors is a microcomputer-based design utilizing various types of spatial light modulators. The configuration of these hybrid optical architectures and discussion of the operation of these systems are presented. The performance of this research program is consistent with proposed research programs supported by the USAF.				
14. SUBJECT TERMS Hybrid Optical Processor, Multiple Matrix Computation, Hybrid Optical Computing Optical Binary Adder			15. NUMBER OF PAGES 114	
			16. PRICE CODE	
17. SECURITY CLASSIFICATION OF REPORT UNCLASSIFIED	18. SECURITY CLASSIFICATION OF THIS PAGE UNCLASSIFIED	19. SECURITY CLASSIFICATION OF ABSTRACT UNCLASSIFIED	20. LIMITATION OF ABSTRACT UL	

HYBRID OPTICAL PROCESSOR

FINAL REPORT

TABLE OF CONTENTS

1.	INTRODUCTION.....	1
2.	SUMMARY AND OVERVIEW.....	1
	2.1 HYBRID PROCESSOR FOR MULTIPLE-MATRIX MULTIPLICATION..	2
	2.2 HYBRID OPTICAL COMPUTING.....	3
	2.3 OPTICAL PERFECT SHUFFLE.....	6
	2.4 OPTICAL BINARY ADDER.....	7
	2.5 APPLICATION OF ASSOCIATIVE MEMORIES TO SYMBOLIC SUBSTITUTION.....	9
	2.6 ACOUSTO-OPTIC SPACE INTEGRATOR.....	9
	2.7 MFSK SIGNAL DETECTION.....	10
	2.8 HARD-CLIPPING JOINT TRANSFORM CORRELATOR.....	11
	2.9 PROGRAMMABLE MULTI-CHANNEL OPTICAL CORRELATOR.....	13
	2.10 WHITE-LIGHT PSEUDOCOLOR ENCODING.....	16
	2.11 PHASE CONJUGATION JOINT TRANSFORM CORRELATOR.....	16
	2.12 PHASE MEASUREMENT BY FRINGE-SCANNING.....	17
	2.13 SYMBOLIC LOGIC PROCESSOR USING CASCADED LIQUID CRYSTAL TELEVISIONS (LCTVs).....	17
	2.14 JOINT FOURIER TRANSFORM PROCESSOR.....	18
	2.15 HOLOGRAPHIC ASSOCIATIVE MEMORY USING A MICRO-CHANNEL SPATIAL LIGHT MODULATOR.....	18
	2.16 A HYBRID-OPTICAL NEURAL NETWORK.....	18
	2.17 OPTICAL DISK BASED NEURAL NETWORK.....	19
3.	CONCLUSIONS.....	19
4.	LIST OF PUBLICATIONS RESULTING FROM THIS SUPPORT.....	20

LIST OF FIGURES

FIGURE 1	A HYBRID OPTICAL PROCESSOR FOR OPTICAL COMPUTING SLM1-slm3, SPATIAL LIGHT MODULATORS; CL ₁ -CL ₄ , CYLINDRICAL LENSES; L ₁ AND L ₂ , LENSES.....	3
FIGURE 2	AN ELECTRO-OPTICAL PROCESSOR. L's-LENSES; P's-POLARIZERS.....	4
FIGURE 3	AN ELECTRO-OPTICAL SYMBOLIC LOGIC PROCESSOR.....	5
FIGURE 4	AN ELECTRO-OPTICAL DISCRETE LINEAR TRANS- FORMATION PROCESSOR. L's-LENSES; P's-POLARIZERS....	6
FIGURE 5	OPTICAL PERFECT SHUFFLE SYSTEM: S ₁ AND S ₁ , INPUT DATA; L ₁ AND L ₁ LENSES; H, FILTERING GRATING.....	7
FIGURE 6a	INPUT DATA TO OPTICAL PERFECT SHUFFLE ARCHITECTURE..	8
FIGURE 6b	THE SHUFFLED VERSION OF THE INPUT DATA.....	8
FIGURE 7	AN OPTICAL SET-UP FOR 4-BIT PARALLEL HALF-ADDER. A, B, INPUTS; M ₁ , M ₂ , MIRRORS; P ₁ , P ₂ , P ₃ , POLARIZERS.....	8
FIGURE 8	OPTICAL SETUP FOR AN ACOUSTO-OPTIC SIGNAL CORRELATOR. AO ₁ AND AO ₂ -CELLS; L ₁ AND L ₂ - TRANSFORM LENSES; L ₂ AND L ₄ -MAGNIFYING LENSES; S-SQUARE-LAW CONVERTER; BS-BEAM SPLITTER.....	10
FIGURE 9	THE OUTPUT CORRELATION PEAKS OBTAINED WITH THE SETUP OF FIGURE 1.....	10
FIGURE 10	MULTICELL, MULTIFREQUENCY ACOUSTO-OPTIC JOINT TRANSFORM CORRELATOR: AO _{0-n-1} , ACOUSTO-OPTIC CELLS: L ₁ AND L ₃ TRANSFORM LENSES: L ₂ AND L ₄ MAGNIFICATION LENSES: S SQUARE-LAW CONVERTER; BS, BEAM SPLITTER; F, SPATIAL FILTER; G, GRATING...	11
FIGURE 11	THE SCHEMATIC OF A PROGRAMMABLE HARD-CLIPPING JOINT TRANSFORM CORRELATOR; L's-LENSES; BS-POLARIZING BEAM SPLITTER.....	13
FIGURE 12	A MULTI-CHANNEL OPTICAL CORRELATOR USING AN ADDRESSED LCTV. L ₁ AND L ₂ , COLLIMATING SYSTEM; L ₃ AND L ₅ , TRANSFORM LENSES; L ₃ , MAGNIFYING LENS; P ₁ AND P ₂ , POLARIZERS; BS, BEAM SPLITTER; M, MIRROR.	

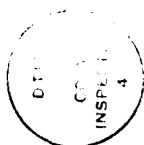
I. Introduction

We have, in the past 27-month period, completed several major tasks of our research on hybrid optical processor programs. Our tasks were completed in a manner consistent with proposed research programs supported by the United States Air Force, Rome Air Development Center at Hanscom Air Force Base, under contract number F19628-87-C-0086. Results have been published, in part, in technical literature and have been presented at scientific conferences.

Copies of these papers are included in this report to provide concise documentation of our research efforts. In the following sections, we shall give an overview of our research work done during the period 1 July 1987 to 30 July 1990. Publications resulting from this effort are included at the end of this report as appendices.

II. Summary and Overview

Recent advances of programmable spatial light modulators (SLM) have permitted the synthesis of hybrid signal processors for various computational needs. In accordance with this research program we have developed and synthesized various types of hybrid optical architectures capable of performing tasks such as: multiple matrix computation, hybrid optical computing, optical binary adder, optical perfect shuffle, application of associative memory to symbolic substitution, acousto optic joint transform correlator for space integration and frequency shift keying applications, hard clipping joint transform correlator, and programmable multi-channel optical correlator for automatic scanning image detection. The basic architecture of these hybrid optical processors is a microcomputer-based design utilizing various types of spatial light modulators. The configuration of these hybrid optical architectures and discussion of the operation of these systems are presented. The performance of this research program is consistent with the proposed research programs supported by the United States Air Force, Rome Air Development Center at Hanscom Air Force Base under contract number F19628-87-C-0086.



Accession For	
NTIS GRA&I	<input checked="" type="checkbox"/>
DTIC TAB	<input type="checkbox"/>
Unannounced	<input type="checkbox"/>
Justification	
By _____	
Distribution/	
Availability Codes	
Dist	Avail and/or Special
A-1	

2.1 Hybrid Processor for Multiple-Matrix Multiplication

We have developed two hybrid optical architectures to perform multiple binary-matrix multiplication [1]. These architectures include microcomputers and programmable spatial light modulators. We have used both the inner-product and systolic-inner-product methods for multiple binary number and multiple matrix multiplication. In the first architecture the inner-product method is used to carry out multiple-matrix multiplication. Figure 1 shows a hybrid optical system which is able to carry out a triple binary number multiplication operation. Three magneto-optic spatial light modulators serve as the inputs. A CCD detects the result and feeds back to a high speed memory. In this system, the multiplication is performed by binary transmittance of the SLM's, and the sum is carried out by focusing the light onto the detector. The introduction of grating masks into this architecture permits a fully parallel matrix multiplication through separation of the output vectors.

The second architecture is a combination of the inner-product and systolic array arrangement techniques. This architecture is capable of performing large matrix multiplication and has applications in linear and bilinear transformations. In this system the binary number matrix representation in the SLM's can be shifted step-by-step for the systolic array arrangement. Thus, matrix multiplication can be performed using this system with the major drawback being the speed. For example, a 2×2 matrix multiplication requires four-step operation. By decomposing the matrices and then applying the systolic-inner-product method, substantial reduction in the size of the SLM's is possible. We have carried out preliminary experimental demonstration of these techniques. In addition, since these techniques are either mixed binary or binary representation, the hybrid optical processors would offer high accuracy with moderate speed for multiple matrix computation.

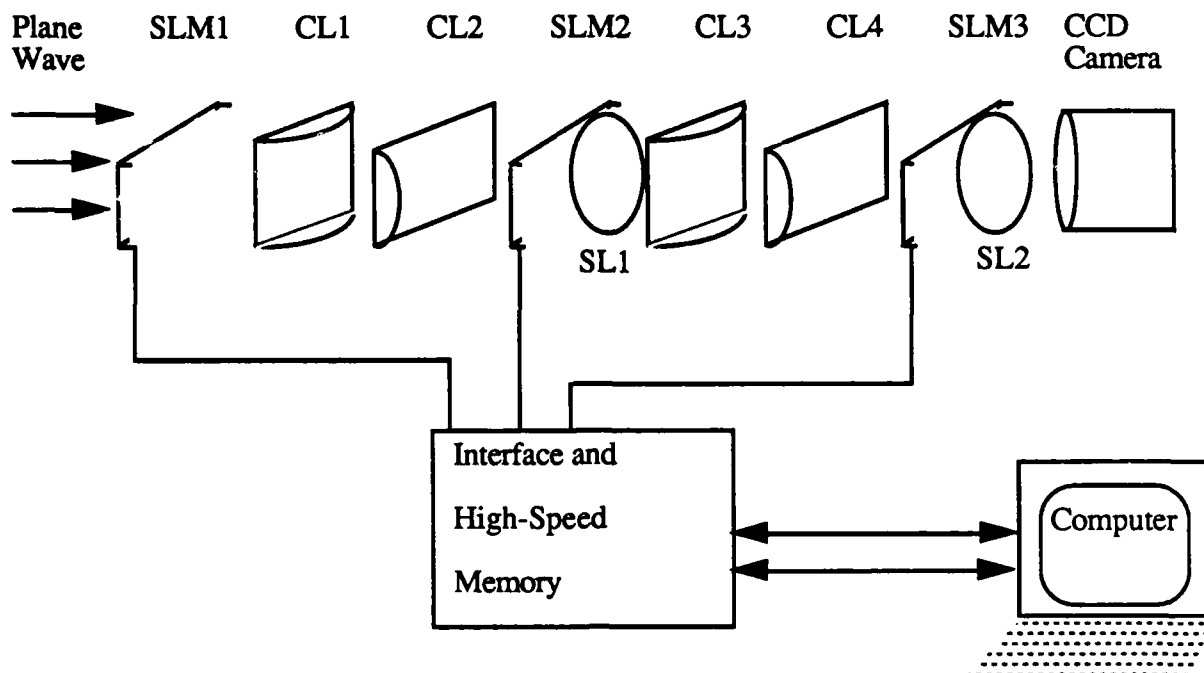


Figure 1. A hybrid optical processor for optical computing. SLM1-SLM3, spatial light modulators; CL₁-CL₄, cylindrical lenses; L₁ and L₂, lenses; SL1-SL2, spherical lenses.

2.2 Hybrid Optical Computing

We have developed several hybrid optical processors utilizing transparent SLM's for digital optical computing [2]. We have shown that digital matrix multiplication (see Figure 2), symbolic logic processing (see Figure 3), and linear transformation (see Figure 4) can be performed with these hybrid architectures. Since MOSLM can be addressed in partial parallel mode, the whole frame pattern on MOSLM can be switched in a very rapid manner; for example, 6.4 μ s for a 64 x 64 MOSLM; 51.2 μ s for a 512 x 512 MOSLM. By utilizing a high speed memory subsystem with a specially designed interfacing circuit (the technology is available) a relatively slow microcomputer can be used to manipulate the parallel operation of MOSLM's. This is known as single instruction multiple data (SIMD) operation. In addition, with the introduction of a microcomputer into the system, a man-machine communication link is also provided. To generate the systolic array formats rapidly, a table look up instruction is suggested. After the time integrating CCD detector, a high speed analog to digital converter (ADC) and a serial-parallel deformater would be used. Thus, by exploiting the programmability of the computer, various linear algebraic operations can be performed with this hybrid optical architectures.

Finally, by exploiting the efficient operation of the optics and the programmability of the electronic computer, it is our belief that hybrid optical architecture would be the logical approach toward modern optical computing. However, much remains to be done in the development of electro-optical devices before the hybrid optical computing can become a widespread practical reality.

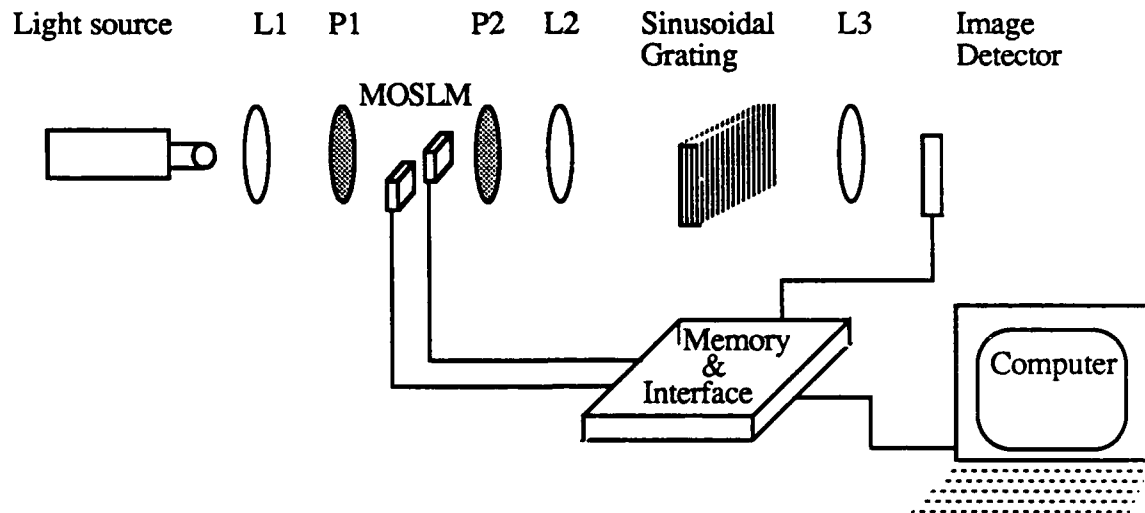


Figure 2. An electro-optical processor. L's-lenses; P's-polarizers.

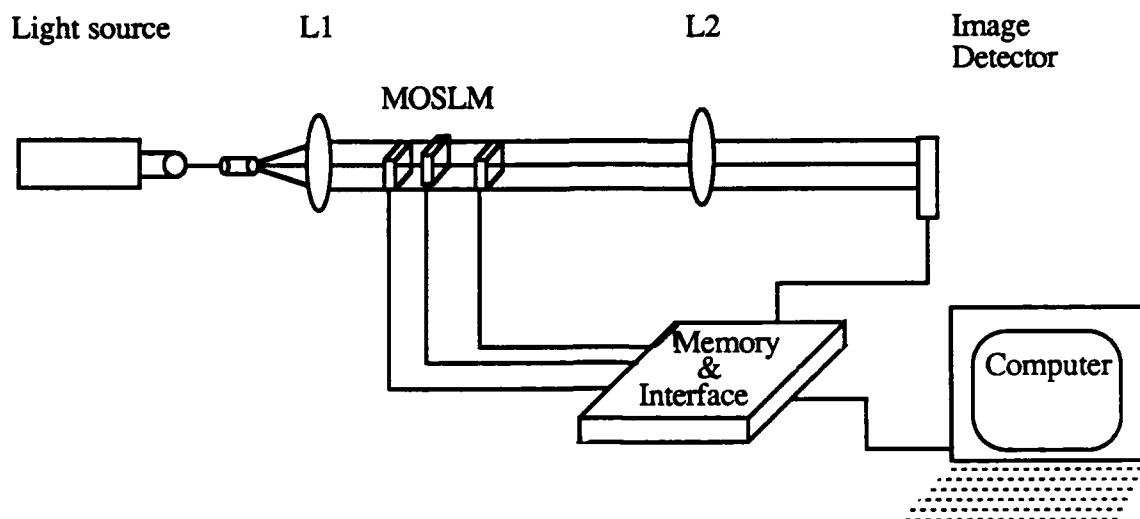


Figure 3. An electro-optical symbolic logic processor. L's-lenses.

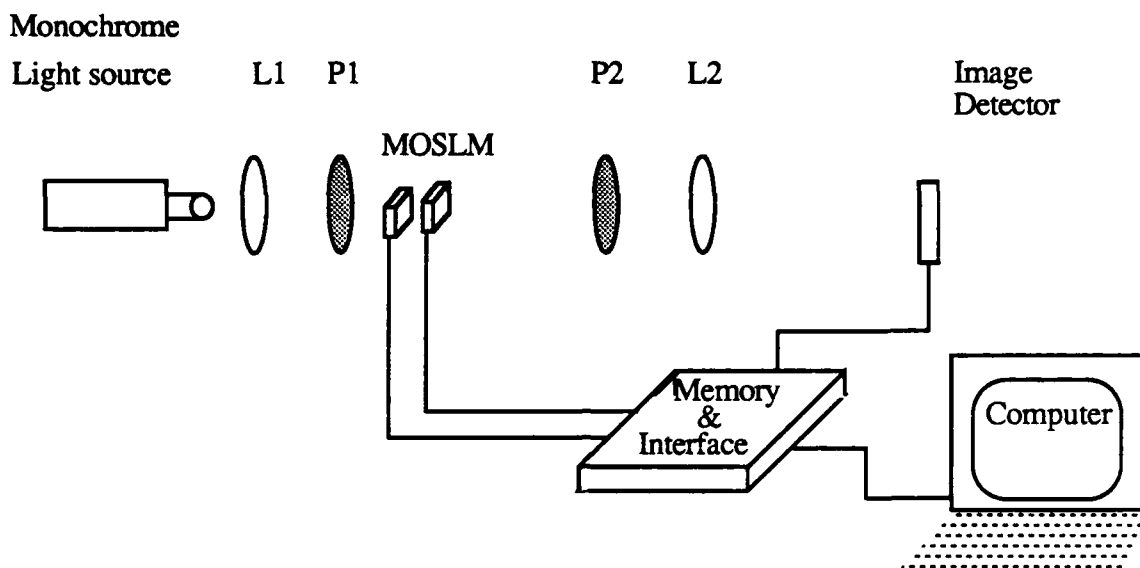


Figure 4. An electro-optical discrete linear transformation processor. L's-lenses; P's-polarizers.

2.3 Optical Perfect Shuffle

One of the inherent advantages of the optical computer is its noninteractive connecting capability. The optical perfect shuffle (PS) which forms the basis of such an interconnect network is a useful concept in optical computer architecture. We have demonstrated that two sets of data can be shuffled using an optical spatial filter [3]. Figure 5 shows the optical perfect shuffle set-up. Two sets of data are designated by S1 and S2, which are separated by 2β at the input plane. With coherent light illumination, the complex light distribution which includes the Fourier spectra of the input data appears in the Fourier plane. To implement perfect shuffle, a sinusoidal grating is placed in the Fourier plane.

In the experiment, we used two sets of English letters as input data. Figure 6(a) shows the input data and Figure 6(b) gives the shuffled data obtained with the proposed system. We have noted that perfect shuffle can also be achieved if two optical processors are arranged in tandem. In this case the perfect shuffle operation can be applied to a 2-D data array, such that one shuffles horizontally and the other vertically. The generalized perfect shuffle with its large data handling capacity might be a viable trade-off for certain applications.

2.4 Optical Binary Adder

We have demonstrated a method of building an optical half adder using a programmable LCTV [4]. This optical half adder is capable of performing the XOR, AND, NOT, and OR logical operations. Experimentally, we have shown that a 4-bit half-addition can be obtained. Figure 7 shows the set-up for 4-bit parallel half-adder. The optical half adder can be easily extended to perform larger-array-numbers addition, by simply changing the computer program of microcomputer. We note that no extra coding is required in the half-adder, since the number was automatically encoded by LCTV. To extend a half adder to perform a full-adder operation we introduce an optical read only memory for carry transmission and overflow error detection. An optical architecture of a 2-bit full adder using an OROM is also proposed.

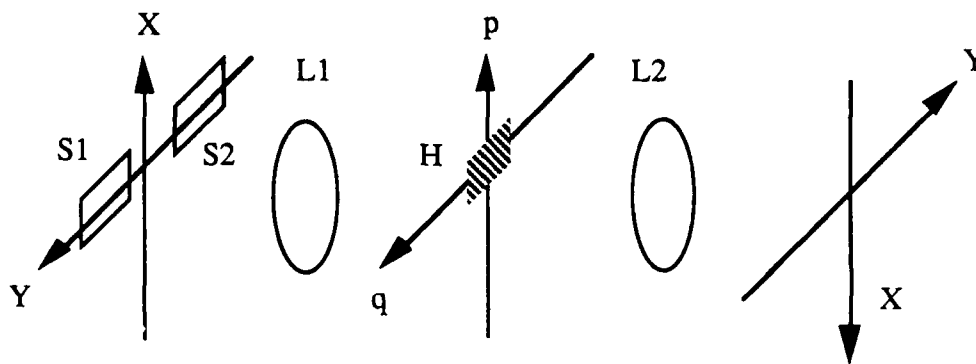


Figure 5. Optical perfect shuffle system: S1 and S2, input data; L1 and L2 lenses; H, Filtering grating.



Figure 6(a). Input data to optical perfect shuffle architecture.



Figure 6(b). The Shuffled version of the input data.

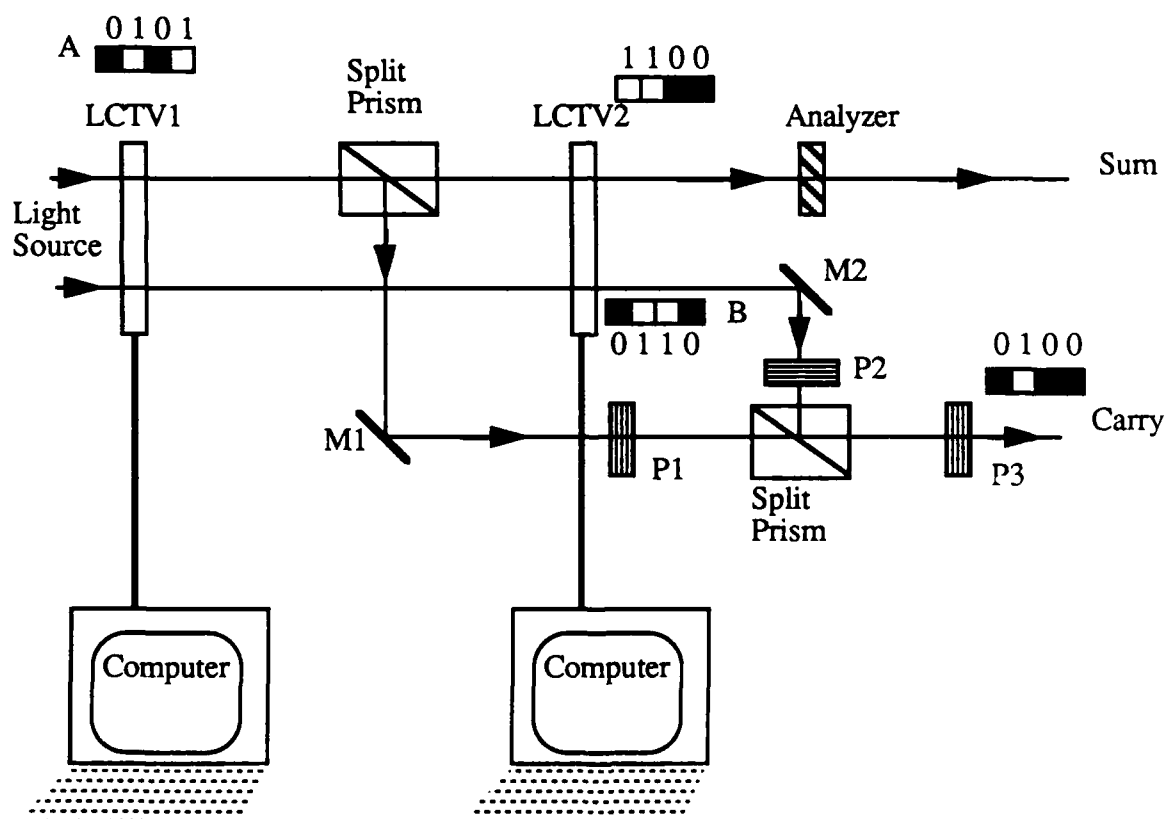


Figure 7. An optical set-up for 4-bit parallel half-adder. A, B, inputs; M1, M2, mirrors; P1, P2, P3, polarizers.

2.5 Application of Associative Memories to Symbolic Substitution

We have demonstrated a technique of spatial modulation to implement symbolic substitution logic using one-step holographic associative memories [5]. The spatial modulation technique gives more flexibility in the filter synthesis than the multiplexing technique since the hologram has a limited dynamic range. We have demonstrated a simple example of multi-instruction multi-data (MIMD) operation, i.e., parallel half addition. By utilizing real-time spatial light modulators such as LCLV, LCTV, MOSLM, a full addition may be realized by multistep substitution. If the final cross correlation can be totally eliminated, the proposed method may be superior sampling technique, since this method is fully space invariant.

2.6 Acousto-Optic Space Integrator

We have developed an architecture for a real-time space integrating correlator based on the optical joint transform correlator [6]. Two parallel on-plane AO cells are employed to convert electrical signals into acoustic strain fields. A transform lens produces the joint transform of the optical pattern induced by the acoustic strain fields. A square law converter, e. g. , a liquid crystal light valve (LCLV), can extract the joint transform power spectrum. The inverse Fourier transform of the coherent readout of the square law converter provides the cross correlation of the input signals.

Since two AO cells are on the same plane, the proposed architecture can be implemented in a compact system (see Figure 8). A simple experiment utilizing an LCTV as square-law converter and applying a 65 MHZ pure sinusoidal signal (for simplicity) to the input cells was conducted. Figure 9 shows the output correlation peaks obtained with the set-up of Figure 8, with the separation between the two AO cells being 12 mm. By addition of an adequate number of AO cells on the input plane, this architecture can easily be extended to a system that yields more than two cross-correlations. At the output plane, we obtain spatially separated cross-correlation functions that correspond to the AO cells. The correct positioning of the AO cells in the input plane will prevent the correlation distribution from overlapping each other. The three cell system may be sufficient for a digital communication system in which two different waveforms are selected for transmission to the receiver. This feature is important for digital communication in which different waveforms are used to represent different messages.

2.7 MFSK Signal Detection

We have developed a multi-channel acousto-optic space integrator for modulated frequency shift keying (MFSK) signal detection [7] as shown in Figure 10. This system consists of an array of AO cells at the input plane and a liquid crystal light valve as the square-law detector for the composite Fourier to power spectrum conversion. In principle this hybrid optical processor is capable of processing very wide bandwidth temporal signals, as high as 10^6 resolution elements. The proposed AO correlator can be synthesized in compact form. One of the requirements of the proposed system is the availability of a square law converter with both high speed and large dynamic range. Thus the realization of this architecture depends upon development of the necessary components.

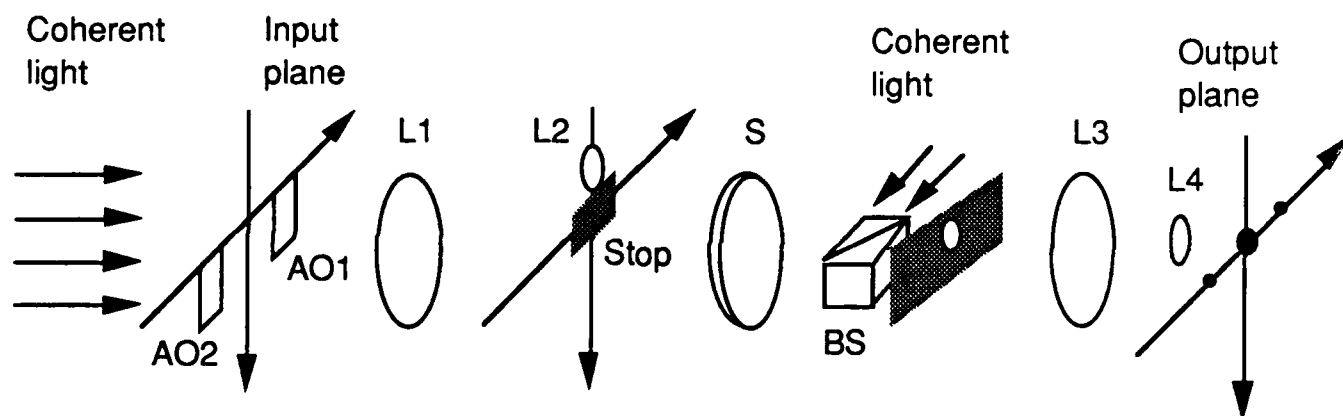


Figure 8. Optical setup for an acousto-optic signal correlator. AO1 and AO2-cells; L1 and L2-transform lenses; L2 and L4-magnifying lenses; S-square-law converter; BS-beam splitter.



Figure 9. The output correlation peaks obtained with the set-up of Figure 1.

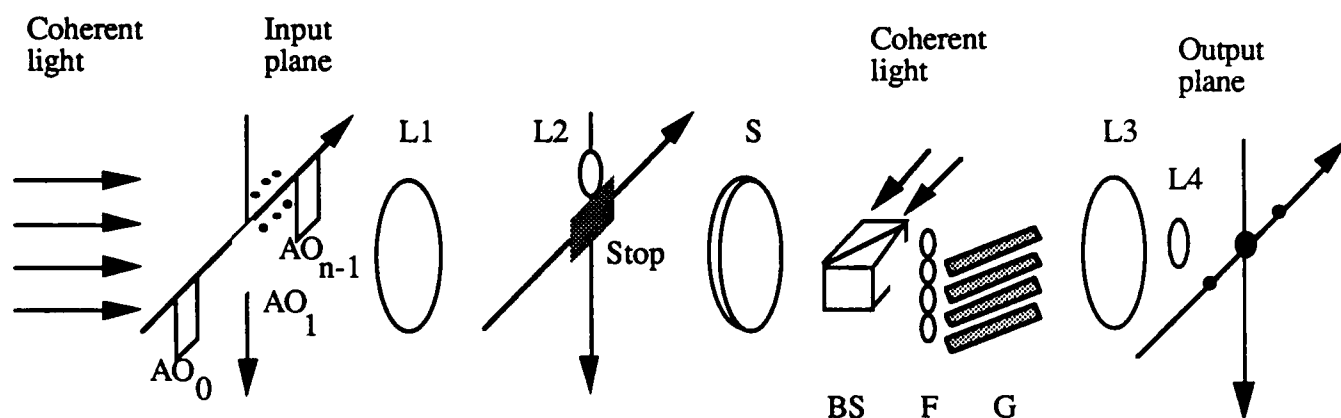


Figure 10. Multicell, multifrequency acousto-optic joint transform correlator: AO_{0-n-1} , acousto-optic cells: L1 and L3 transform lenses: L2 and L4 magnification lenses: S, square-law converter: BS, beam splitter: F, spatial filter: G, grating.

2.8 Hard-Clipping Joint Transform Correlator

Because of its high speed and structural simplicity, the optical joint transform correlator is proposed for application to pattern recognition. We have developed a real-time programmable hybrid joint transform correlator utilizing the threshold hard-clipping properties of a microchannel spatial light modulator (MSLM) [8]. In the system, an MSLM is utilized as the threshold hard-clipping device and a liquid crystal television (LCTV) is used as the input and reference images. By using the feed-back loop, as depicted in Figure 11, the system offers the adoptive processing capability.

The LCTV is used to display a real-time target and a reference image at the input plane of an optical processor. The main advantage of LCTV is its programmability for the generation of different reference images. The lens system L1-L3 is employed to demagnify the input object images from the LCTV to an appropriate size and then transform onto the MSLM. The output is detected by a CCD camera and it can be fed back to the microcomputer for further operation making the system an adaptive hybrid electro-optic correlator.

To compare the performance of the real-time programmable JTC over the existing JTC techniques, with regard to the intensity of the correlation peaks, a theoretical analysis of the two system has been carried out. Equations 1 and 2 show the autocorrelation function distribution at the output plane for the conventional system and the real-time programmable JTC respectively.

$$g(x, y) = -A \frac{1}{4\omega^2} \left[\Lambda\left(\frac{X-L}{\omega}\right) + \Lambda\left(\frac{X+L}{\omega}\right) \right] \Lambda\left(\frac{Y}{\omega}\right) \quad (1)$$

$$E = \frac{A}{\pi} \left\{ \frac{\sin[\pi(X-L)/\omega]}{\pi(X-L)} + \frac{\sin[\pi(X+L)/\omega]}{\pi(X+L)} \right\} \frac{\sin(\pi Y/\omega)}{\pi Y} \quad (2)$$

Where A is the illumination amplitude, and Λ represents a triangular function, we see that the correlation peak intensity of the proposed system is about $A^2/\pi^2\hat{U}^4$, whereas for the conventional JTC it would be $A^2/16\hat{U}^4$. In other words, the correlation peak intensity of the proposed system would be about 1.62 times higher than that of the conventional system. In addition, if the bias voltages can be controlled such that the threshold hard-clipping takes place at a lower intensity level to include the whole main lobe, it can be shown that the peak intensity function is $16A^2/\pi^2\hat{U}^4$, which is 26 times higher than the classical JTC. The autocorrelation function distribution at the output plane for this system is shown in Equation 3.

$$E = \frac{A}{\pi} \left\{ \frac{\sin[2\pi(X-L)/\omega]}{\pi(X-L)} + \frac{\sin[2\pi(X+L)/\omega]}{\pi(X+L)} \right\} \frac{\sin(2\pi Y/\omega)}{\pi Y} \quad (3)$$

It should be mentioned that, if the threshold hard-clipping values are further controlled to include the first side lobes, the output correlation intensity could be further increased.

By combining the advantages of the state-of-the-art electro-optic devices and the flexibility of a microcomputer, this technique overcomes the common drawback of the existing methods, namely, low correlation peak intensity compared to the illumination intensity hence producing sharper autocorrelation peaks. We stress that this JTC can produce sharper and higher correlation intensity than conventional JTC.

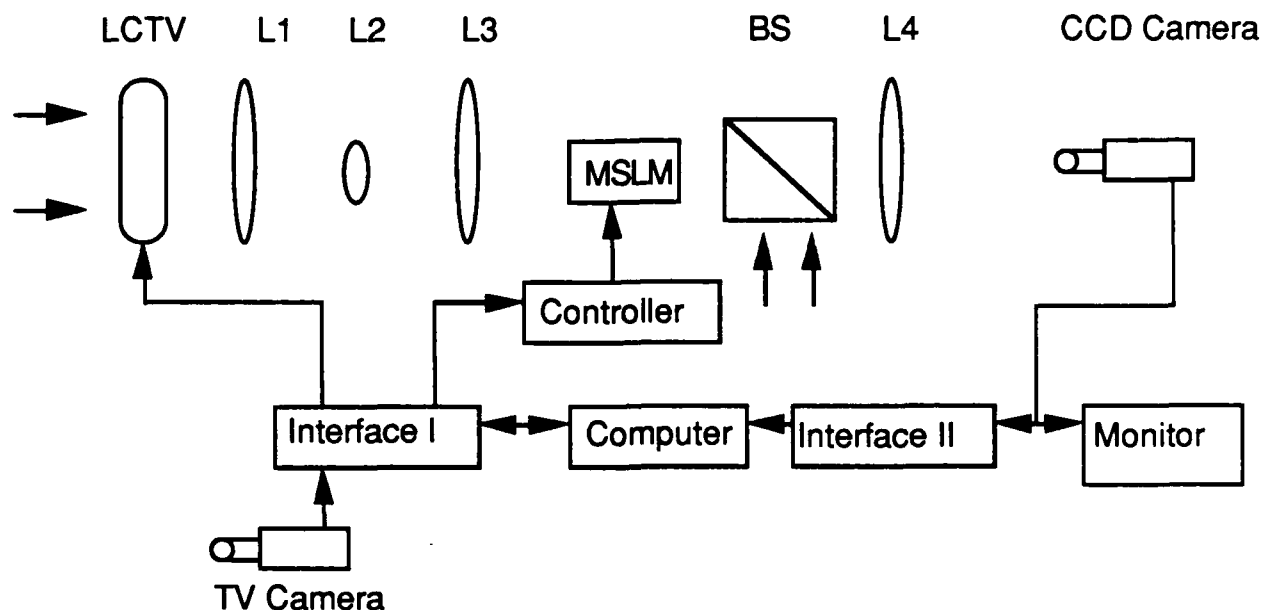


Figure 11. The Schematic of a programmable hard-clipping joint transform correlator: L's- Lenses; BS-polarizing beam splitter.

2.9 Programmable Multi-Channel Optical Correlator

We have developed a programmable scanning optical correlator using a low cost liquid crystal television (LCTV) [9]. The imposition of a scanning grating on an LCTV screen with a micro-computer will alleviate the positioning problem associated with the mechanical scanning method for large capacity correlator systems, as shown in Figure 12. The positioning difficulty can be caused by either movement or the frequency shift in the mechanical scanning techniques. The low resolution of LCTV which limits spatial carrier frequency is overcome by using a new set-up which is different from a conventional optical correlator. The lenses L2 and L3 are used to project a reduced image of the LCTV grating onto the input plane of the optical correlator, so that the Fourier transform of the object can be in a proper scale while the spatial frequency of the spectrum of the grating is magnified. The different diffraction orders on the frequency plane can therefore be sufficiently separated.

We set adjustable delays between the subroutines, longer delays for filter construction and shorter delays for target detection. In order to multiplex matched filters onto a recording plate, we would rotate the grating one at a time. While an input image is being recognized, the orientation of the grating is automatically changed according to the instruction received from the microcomputer. As soon as the auto-correlation peaks appears at the output plane, the scanning is terminated, otherwise continued. Using a multi-channel spatial filter of eight input objects which were recorded on a holographic plate and observation of the corresponding output correlation peaks we have concluded that a multi-channel correlating operation can be achieved using a programmable LCTV grating.

The scanning speed of the proposed correlator is primarily limited by the microcomputer and the response time of the LCTV. Furthermore, if a higher resolution LCTV is available, both the input object and the modulating grating can be superimposed onto the LCTV screen. Thus a programmable, real-time, electrically addressed correlator may be realized.

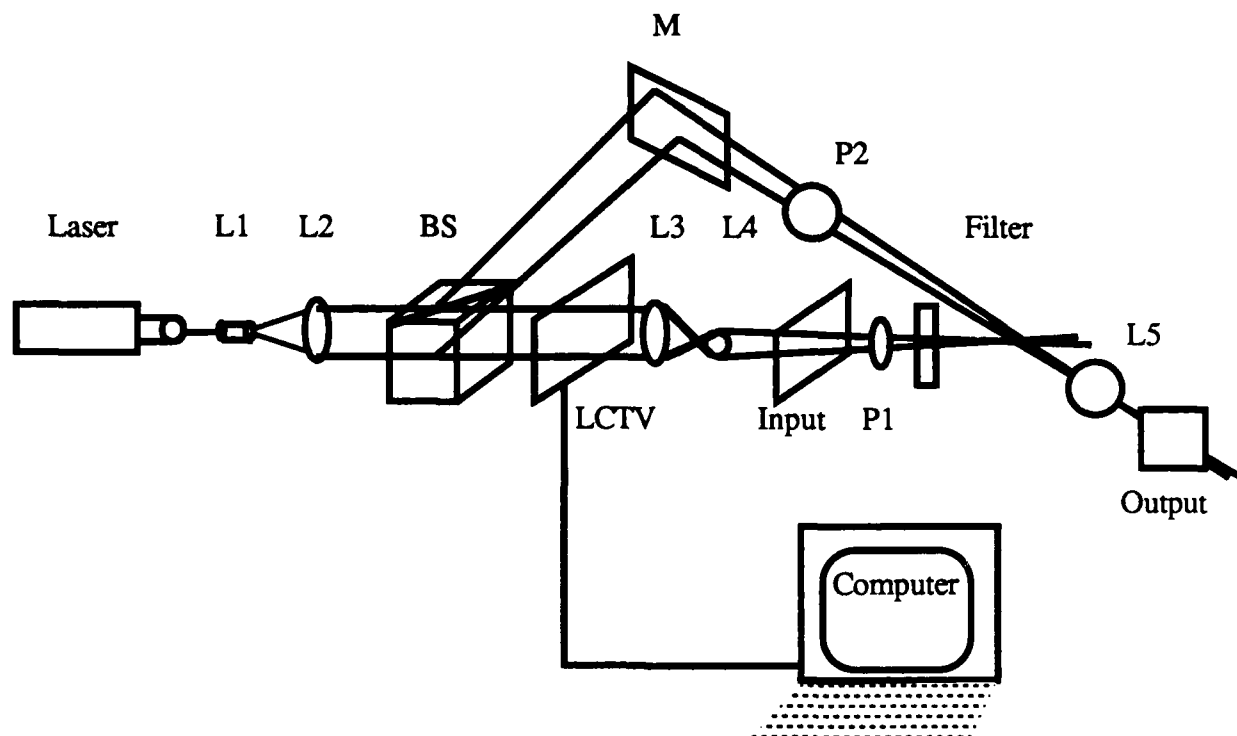


Figure 12. A multi-channel optical correlator using an addressed LCTV. L_1 and L_2 , collimating system; L_3 and L_5 , transform lenses; L_3 , magnifying lens; P_1 and P_2 , polarizers; BS, beam splitter, M, mirror

2.10 White-Light Pseudocolor Encoding

Pseudocolor encoding is a commonly used enhancement for grey level images. We have in this period of research developed a two-step, three-color, white-light pseudocolor encoding process. A variation of this three color encoding method uses moire fringe patterns from two encodings to carry the information previously obtained from the third encoding. By using this new procedure, the pseudocolor encoding was accomplished using a single sampling grating, and two rather than three exposures. This allows greater use of the dynamic range of the film by eliminating one exposure. This method also illustrates an interesting application of moire patterns.

2.11 Phase Conjugation Joint Transform Correlator

In this period of research, several applications of phase conjugation technique in a JTC have been investigated. It is shown that phase distortion in the input objects (due to SLM) in a coherent image processing system can be efficiently compensated by using the phase conjugation technique. The additional amplitude or phase modulations produced by the nonlinearity of phase conjugation can be utilized to pre-encode the object functions, for which correlation characteristics can be improved. Computer simulations indicate that phase pre-encoded objects improve the accuracy of correlation detection, which results from smaller autocorrelation spots and lower cross correlation intensity. This encoding technique would find application in the research of dynamic pattern recognition and robotic vision.

2.12 Phase Measurement by Fringe-Scanning

We have developed a novel method for obtaining the phase distribution of an object spectrum by using a fringe-scanning phase-conjugate interferometer. A detailed analysis of the proposed technique is provided, and experimental demonstrations for validating this technique are also given. The major advantages of this method are its potentially high accuracy and its low space-bandwidth-product requirement for the detection system. Moreover, using the fringe-scanning method, the factors to be multiplied are fixed to only a few values. Instead of performing real-time multiplications, one can use a data look-up table to speed up the computational process. Moreover, the spectral content of the object in the Fourier plane is concentrated mostly in some specific regions. It is generally not necessary to compute the phase distribution over the entire $n \times n$ points. In other words, the computation can be selected based on the spectral intensity distribution; thus the amount of computational time can be substantially reduced.

2.13 Symbolic Logic Processor Using Cascaded Liquid Crystal Televisions (LCTVs)

We have shown in the period of research that optical symbolic logic operation can be easily achieved with cascaded low-cost LCTVs. Aside from the basic 16 logic operations, we have shown that the same processor can perform any two-level logic function. Major limitations on using LCTV must be the low resolution, low contrast, low speed and low transmittance, which prevent widespread practical applications. Nevertheless, the low cost and programmability of the LCTV would stimulate some interest in the application of symbolic logic processing. Since the digital computation can be divided into a series of specific logic functions, perhaps some specialized digital uniprocessors may be implemented based on this proposed optical processor.

2.14 Joint Fourier Transform Processor

In this phase of research, we have shown that a joint Fourier transform processor can be used as a conventional coherent optical processor. In principle, the joint transform processor can perform all the optical data processing that a conventional coherent optical processor can offer. Sample illustrations for signal extraction and image subtraction are given. The major advantages of the joint transform processor must be (1) the avoidance of synthesizing a matched spatial filter, (2) higher space bandwidth product, (3) lower spatial carrier frequency requirement, (4) higher output diffraction efficiency, etc.

2.15 Holographic Associative Memory Using a Microchannel Spatial Light Modulator

We have, in this research program, investigated a holographic associative memory system with a controllable MSLM. Since the MSLM is used as an active device in the system, the quality of the output addressed data can be improved as compared with a passive holographic method. Another advantage of the system is its controllability, by which the memory addressing mode can be adjusted to either "winner-take-all" or "weighted sum" operations. The joint transform method has the merit of easy system alignment and real-time filter synthesis. It is apparent that if programmable spatial light modulators were used at the input plane P_1 and the holograph plane P_2 and a feedback loop was constructed between them, the memory capacity of the system could be further enhanced.

2.16 A Hybrid-Optical Neural Network

In this research program, we have developed a 2-D hybrid optical neural network using a high resolution video monitor as a programmable associative memory. Experiments and computer simulations of the system have been conducted. The high resolution and large dynamic range of the video monitor enable us to implement a hybrid neural network with more neurons and more accurate operation. The system operates in a high speed asynchronous mode due to the parallel feedback loop. The programmability of the system permits the use of orthogonal protection and multilevel recognition algorithms to increase the robustness and storage capacity of the network.

2.17 Optical Disk Based Neural Network

We have, in this period of research, proposed a technique for using an optical disk as a large capacity associative memory in an optical neural network which will be described.

There are, however, several problems that should be addressed before constructing the optical disk based neural network.

The readout head has to be redesigned for reading the whole block of an IWM rather than sequential readout techniques.

The existing SLM still cannot meet the processing speed of the proposed system (i.e., $\sim 10^9$ Hz). However, the optical disk based neural network is suitable for applications to a huge database associative search, which does not require a frequent change of input patterns.

The electronic bottleneck in the feedback loop may be alleviated to some extent by using parallel buffers. However, a decision-making circuit for postprocessing the output data in 2-45 μ s has to be developed.

Nevertheless, the proposed optical disk based neural network offers a large capacity associative database for which high speed operation can be achieved.

3.0 Conclusion

Dove Electronics, Inc. and the Pennsylvania State University have designed and demonstrated various hybrid optical processor architectures for signal/data processing applications. These applications include multiple matrix computation, hybrid optical computing, optical binary adding, optical perfect shuffle, joint transform correlation, Fourier transformation, holographic associative memory, and hybrid optical neural network. These various architectures were implemented using a combination of spatial light modulators and computers. Some of these architectures have immediate operational potential, while others require component development to increase speed of operation and reliability. Follow-on efforts to develop components and improve reliability are indicated.

List of Publications Resulting from this Support :

1. F. T. S. Yu and T. W. Lu, "Digital Optical Multiple Matrix Multiplication Based on Inner Product and Systolic-Inner-Product Architecture," *Proceedings of SPIE on Hybrid Image and Signal Processing*, Vol. 933, pp. 12-18, April 1988.
2. F. T. S. Yu, "Hybrid Optical Computing," *IEEE potential*, Vol. 6, pp. 34-37, December 1987.
3. Y. Jin and F. T. S. Yu, "Optical Binary Adder Utilizing Liquid Crystal Television," *Optical Communication*, Vol. 65, pp. 11-16, January 1988.
4. Q. W. Song and F. T. S. Yu, "Optical Perfect Shuffle Using Spatial Filtering," *Applied Optics*, Vol. 22, pp. 1222-1223, April 1988.
5. F. T. S. Yu, C. H. Zhang and S. Jutamulia, "Application of One-Step Holographic Associative Memories to Symbolic Substitution," *Optical Engineering*, Vol. 27, pp. 399-402, May 1988.
6. F. T. S. Yu and T. Nagata, "An Optical Architecture for Acousto-Optic Space Integrating Correlator," *Optical Engineering*, Vol. 27, pp. 507-511, July 1988.
7. F. T. S. Yu and T. Nagata, "MFSK Signal Detection Using Acousto-Optic Joint Transform Correlator," *Microwave and Optical Technology Letters*, Vol. 1, pp. 190-193, August 1988.
8. F. T. S. Yu, Q. W. Song, Y. Suzuki and M. Mu, "Real-Time Programmable Joint Transform Correlator with a Threshold Hard Clipping Microchannel Spatial Light Modulator," *Proceedings of OSA on Spatial Light Modulators and Applications*, Technical Digest Series, Vol. 8, pp. FB1-FB229, June 1988.
9. F. T. S. Yu, Q. Zhon and C. H. Zhang, "Multiple Channel Optical Correlator Via Rotating Grating on LCTV," *Applied Optics* (in press).
10. F. T. S. Yu, Q. W. Song, Y. Suzuki and M. Mu, "Hard Clipping Joint Transform Correlator Using A Microchannel Spatial Light Modulator," Submitted to *Microwave and Optical Technology Letters* (in press).
11. F. T. S. Yu, C. Zhang, Y. Jin and S. Jutamulia, "Application of Holographic Associative Memory to a Hybrid Binary Adder," *SPIE Proceedings on Holographic Optics: Design and Application*, Vol. 883, pp. 254-259, January 1988.
12. F. T. S. Yu and T. Nagata, "Acousto-Optic Joint Transform Correlator as Applied to Spread Spectrum Communication," *Proceedings of SPIE on Advances in Optical Information Processing III*, Vol. 936, pp. 191-197, April 1988.
13. F. T. S. Yu, S. Jutamulia and E. Tam, "Gray Level Pseudocolor Encoding Using LCTV" *Journal of Optics* (in press).

14. F. T. S. Yu and J. E. Ludman, "Joint Fourier Transform Processor," Submitted to Microwave and Optical Technology Letters.
15. F. T. S. Yu and T. Nagata, "Binary Phase Only Joint Transform Correlator," Submitted to Applied Optics.
16. X. X. Chen, A. W. Mayers and F. T. S. Yu, "A Two-Step, Three Color, White-Light Pseudocolor Encoding Process," J. Optics, Vol 19, pp. 177-180, 1988.
17. Q. W. Song and F. T. S. Yu, "Holographic Associative Memory System Using A Thresholding Microchannel Spatial Light Modulator," Optical Engineering, Vol. 28, pp. 533-536, May 1989.
18. F. T. S. Yu and T. Lu, "Digital Optical Architectures for Multiple Matrix Multiplication," Optics Communications, Vol. 71, pp. 39-45, May 1989.
19. F. T. S. Yu, S. Wu and A. W. Mayers, "Applications of Phase Conjugation to a Joint Transform Correlator," Optics Communications, Vol. 71, pp. 156-160, May 1989.
20. F. T. S. Yu, S. Wu and A. W. Mayers, "Phase Measurement of a Fourier Spectrum by a Fringe-Scanning Phase-Conjugate Interferometer," Optics Letters, Vol. 14, pp. 1171-1173, November 1989.
21. S. Wu, T. Lu, X. Xin and F. T. S. Yu, "An Adaptive Optical Neural Network Using a High Resolution Video Monitor," Microwave and Optical Technology Letters, Vol. 2, pp. 252-257, July 1989.
22. T. Lu, S. Wu, X. Xu and F. T. S. Yu, "Two-Dimensional Programmable Optical Neural Network," Applied Optics, Vol. 28, pp. 4908-4913, November 1989.
23. T. Lu, K. Choi, S. Wu, X. Xu, and F. T. S. Yu, "Optical Disk Based Neural Network," Applied Optics, Vol. 28, pp. 4722-4724, November 1989.
24. F. T. S. Yu, Y. Jin and C. Zhang, "Symbolic Logic Processor Using Cascaded Liquid Crystal Televisions (LCTVs)," Microwave and Optical Technology Letters, Vol. 2, pp. 309-313, September 1989.
25. Q. W. Song and F. T. S. Yu, "Generalized Perfect Shuffle Using Optical Spatial Filtering," Applied Optics, Vol. 27, pp. 1222-1223, April 1988.
26. F. T. S. Yu, S. Wy, and A. W. Mayers, "Applications of Phase Conjugation to a Joint Transform Correlator," Optics Communications, Vol. 71, pp. 156-160, May 1989.

Hybrid optical computing

Francis T. S. Yu

**High accuracy,
high data rate,
electro-optical architecture**

Lightweight and pocket sized, the optical signal processor can perform a myriad of complicated processing operations. Its success is primarily due to the profound diffraction phenomena of coherent light. The essential merit of an optical signal processor is its capability to process a signal in complex amplitude, parallelism, large capacity, high speed and diversified wavelength. Several processing operations have proven to be more efficient with optical techniques than with their electronic counterparts. These operations are: Fourier transforms, convolutions, correlation operations and spectrum analysis. The major advantages of an electronic computer is its flexibility, programmability and easy accessibility. (Optical signal processors are very inflexible compared with electronic computers.) The question is, "Can we exploit the efficient operation of optics and the flexibility of electronics to come up with a realistic electro-optical (EO) architecture that meets our computational needs?" The answer to this question is, "yes."

First, let me point out that the earlier development of the electronic computer was based on state-of-the-art technology available at that time. It was a very realistic approach that we should adopt for the development of our electro-optical computer.

Second, the current optical signal processor can be regarded as a highly efficient processing system like a high performance vehicle, which requires human intervention to perform properly. Likewise, in order for an optical signal processor to function efficiently, we need an electronic computer to lend a hand. The intervention of an electronic computer is not for data processing. Rather, its purpose is to control the electro-optical devices

so data can be primarily processed by the optical processor. Thus, high accuracy and high data rate processing can be achieved by the electro-optical computer.

Digital-optical computing

Credit for the first optical architecture proposed to carry out matrix-vector multiplication must be given to J. W. Goodman and his colleagues. They used a light emitting diode (LED) to generate a time sequence vector, with a binary mask to control the variable openings representing a matrix format to perform matrix-vector multiplication. A similar LED, with higher accuracy optical architecture for matrix-vector operation, was developed later by others. They utilized a linear array of LEDs to generate an input vector and array of acousto-optic cells to represent a matrix formulation of vector-matrix multiplication. To avoid the interfacing difficulties, still others introduced a systolic array processing concept for optical matrix-matrix multiplication.

However, the analog nature of the optical processing techniques limits

the accuracy of these operations. To alleviate this problem, digital representation was introduced. Multiplying two numbers on a digit-by-digit basis, a numerical multiplication technique was demonstrated that could perform using optical convolution operations. Next, the concept of implementing a real-time convolution-based multiplication was introduced. The idea suggested was an outer product technique with correlation matrices. Also, a number of architectures have been proposed to exploit the parallelism of optics. This is described in a survey paper by R. A. Athale. (See "Read more about it.")

Matrix-matrix multiplication

To exploit the parallelism of optical processing, an electro-optical (EO) processor is used as shown in Fig. 1. This EO architecture utilizes an outer product technique for matrix-matrix multiplication.

Figure 2 shows the outer product computation. When the row and column electrodes of a two-dimensional (programmable) electro-optic spatial light modulator (SLM) is addressed by

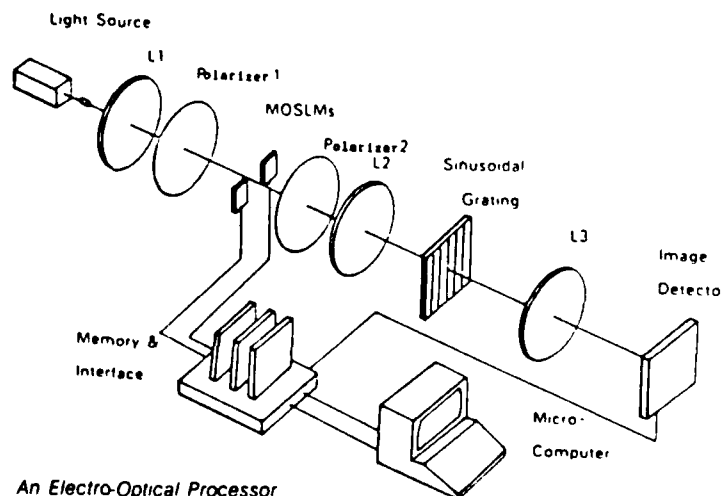


Fig 1 An Electro-Optical Processor

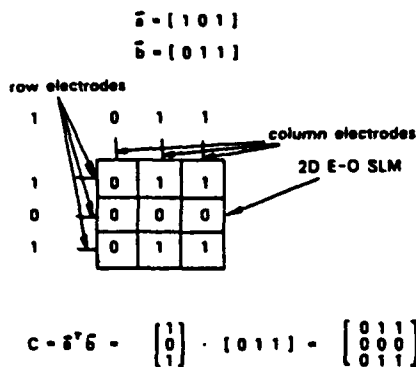


Fig. 2. An Outer Product Computation. two binary vectors a and b , such as $\bar{a} = [1 \ 0 \ 1]$, and $\bar{b} = [0 \ 1 \ 1]$,

the corresponding outer product would be

$$a = \bar{a}' \bar{b} = \begin{bmatrix} 1 \\ 0 \\ 1 \end{bmatrix} [0 \ 1 \ 1] = \begin{bmatrix} 0 & 1 & 1 \\ 0 & 0 & 0 \\ 0 & 1 & 1 \end{bmatrix}$$

It is clear now that a matrix-matrix multiplication can be computed by successive outer product operations, as shown in the following illustration.

$$\begin{bmatrix} a_{11} & a_{12} & a_{13} \\ a_{21} & a_{22} & a_{23} \\ a_{31} & a_{32} & a_{33} \end{bmatrix} \begin{bmatrix} b_{11} & b_{12} & b_{13} \\ b_{21} & b_{22} & b_{23} \\ b_{31} & b_{32} & b_{33} \end{bmatrix} = \begin{bmatrix} a_{11} \\ a_{21} \\ a_{31} \end{bmatrix} \begin{bmatrix} b_{11} & b_{12} & b_{13} \end{bmatrix} + \begin{bmatrix} a_{12} \\ a_{22} \\ a_{32} \end{bmatrix} \begin{bmatrix} b_{21} & b_{22} & b_{23} \end{bmatrix} + \begin{bmatrix} a_{13} \\ a_{23} \\ a_{33} \end{bmatrix} \begin{bmatrix} b_{31} & b_{32} & b_{33} \end{bmatrix}$$

Such computations can also be used to carry out the multiplication of two arbitrary matrices by appropriate decomposition and summing.

Since a multiplication between two single bits is equivalent to the logic operation AND, an outer product operation can be carried out with a Magneto-Optic (MO) SLM. In other words, the row and column electrodes of the MOSLM can be addressed with two binary vectors a and b , and the outer product C can be directly evaluated.

With reference to the EO architecture of Fig. 1, the grating in the Fourier plane diffracts the outer products of AB , from the MOSLM, to form an elementary 2×2 matrix at the origin of the output plane. As an example, a 2×2 elementary matrix $C = AB$ representation of a 16×16 extended binary matrix is seen in the experimental result shown in Fig. 3. Thus, a higher order matrix multiplication can be obtained by decomposing the matrices into a number of elementary 2×2 matrices and then performing the basic matrix multiplication optically.

Symbolic logic processing

Basic optical logic array processing has been reported recently. Thus, a programmable optical symbolic logic processor can be constructed as shown in Fig. 4. A collimated light is used to illuminate three cascaded SLMs. The product of their generated patterns is then imaged onto a charge coupled device (CCD) area detector. The output CCD data are then fed to electronic "OR" circuits, before being stored in a high speed memory subsystem.

As an example, a binary input pattern A is subdivided into $N \times N$ small regions called "logic cells." To perform the logic operation, the value a_{ij} (0 or 1) of each ij th cell are encoded with binary patterns, as shown in the top row of Fig. 5 (a). We then utilize a 2×2 pixel of the SLM for each logic cell. The other binary input pattern B is encoded in a similar manner, as shown in the bottom row of Fig. 5(a). These encoded binary patterns can be generated with a microcomputer memory subsystem. The encoded patterns of A and B are then written into the SLM1 and SLM2,

$$A = \begin{pmatrix} 16.75 & 22.50 \\ 22.50 & 56.50 \end{pmatrix} \quad B = \begin{pmatrix} 50.25 & 53.25 \\ 51.50 & 10.25 \end{pmatrix}$$

$$C = A \cdot B = \begin{pmatrix} 2000 & 4375 & 1122 & 5625 \\ 4040 & 375 & 1777 & 25 \end{pmatrix}$$

$$\begin{pmatrix} 1 & 1 & 0 & 0 & 1 & 0 & 0 & 1 & 1 & 1 & 0 & 1 & 0 & 1 & 1 \\ 1 & 1 & 0 & 0 & 1 & 1 & 1 & 0 & 0 & 0 & 1 & 0 & 1 & 0 & 0 & 1 \end{pmatrix}$$

0 0	0 0 0 0 0 0 0 0	0 0 0 0 0 0 0 0
1 1	2 2 0 0 2 1 1 1	1 1 1 1 1 1 0 2
0 0	0 0 0 0 0 0 0 0	0 0 0 0 0 0 0 0
0 1	1 1 0 0 1 1 1 0	0 0 1 0 1 0 0 1
0 1	1 1 0 0 1 1 1 0	0 0 1 0 1 0 0 1
0 0	0 0 0 0 0 0 0 0	0 0 0 0 0 0 0 0
1 1	2 2 0 0 2 1 1 1	1 1 1 1 1 1 0 2
1 0	1 1 0 0 1 0 0 1	1 1 0 1 0 1 0 1
0 1	1 1 0 0 1 1 1 0	0 0 1 0 1 0 0 1
1 1	2 2 0 0 2 1 1 1	1 1 1 1 1 1 0 2
0 1	1 1 0 0 1 1 1 0	0 0 1 0 1 0 0 1
1 1	2 2 0 0 2 1 1 1	1 1 1 1 1 1 0 2
0 0	0 0 0 0 0 0 0 0	0 0 0 0 0 0 0 0
1 1	2 2 0 0 2 1 1 1	1 1 1 1 1 1 0 2
0 0	0 0 0 0 0 0 0 0	0 0 0 0 0 0 0 0

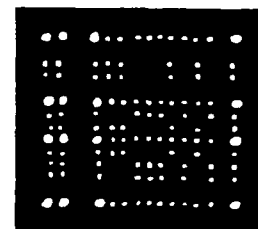


Fig. 3. Matrix Multiplication.

transform the optical signal from every pixel (after the light passes through the cascaded SLM) into arrays of electrical signals. The four pixel signals of a logic cell can be combined with a Transistor Transistor Logic (TTL) "OR" gate. Thus, a logic operation resulting from a logic cell can be expressed as

$$c_{ij} = \alpha(a_{ij}b_{ij}) + \beta(a_{ij}b_{ij}) + \gamma(a_{ij}b_{ij}) + \delta(a_{ij}b_{ij}),$$

where $+$ stands logic "OR" operations.

The spatial representations of the sixteen logic gates and the resulting patterns are shown in Fig. 6. Since the

respectively. Since SLM1 and SLM2 are closely cascaded, the combination states of a_{ij} and b_{ij} are represented by the patterns shown in Fig. 5(b). A logic operation in one channel is also represented by a 2×2 pixel pattern of the SLM3. $(\alpha, \beta, \gamma, \delta)$ represents the switching states (0 or 1) of the pixels of a logic mask as shown in Fig. 5(c). Thus, the combinations of these 2×2 pixel logic cells would provide a total of 16 logic gates.

A CCD area detector is used to

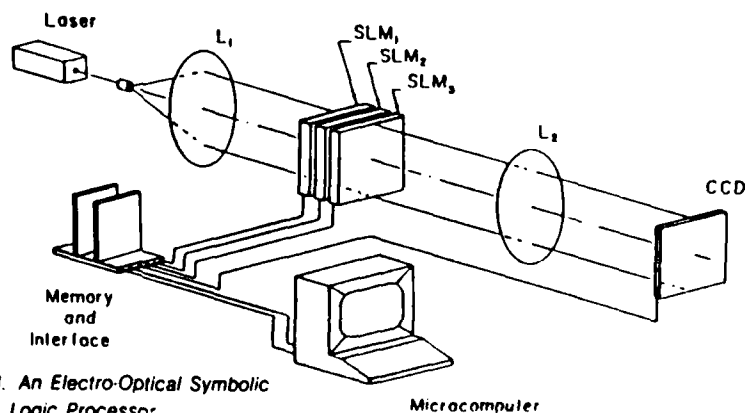


Fig. 4. An Electro-Optical Symbolic Logic Processor.

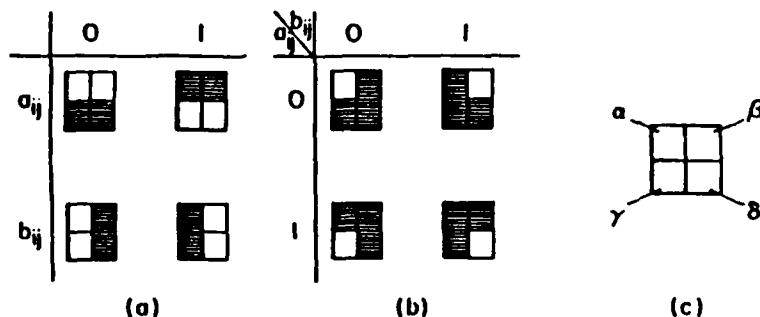
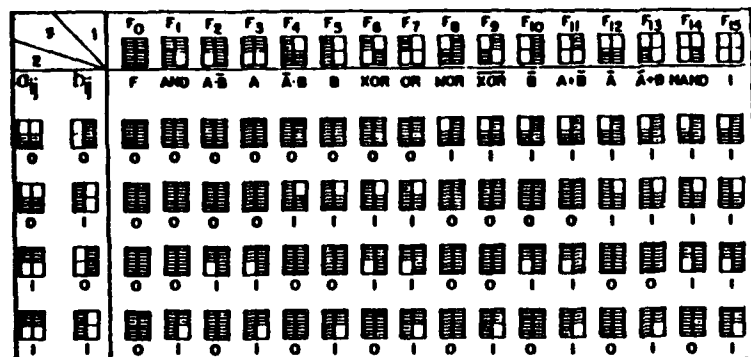


Fig. 5. (a) Encoded Input Patterns.
(b) Product of the Input Patterns.
(c) A Logic Mask.



NOTE: 1- CONTROL PATTERNS
2- INPUT PATTERNS
3- OUTPUT PATTERNS



Fig. 6. Representation of the Sixteen Logic Functions.

final result of c_{ij} is represented by an electrical signal, it can be directly stored in the memory subsystem, which can be used in the next cycle of operation.

It should be noted that the combinations of the 16 logic functions are the fundamentals of the arithmetic operations of a digital computer. It is obvious that the proposed technique has the ability to perform the arithmetic operation of two input patterns.

Discrete linear transformations

A discrete linear transformation (DLT) system represented in Fig. 7 can be characterized by an impulse response h_{mn} . The input-output relationship of such a system can be summarized by the following equation:

$$g_m = \sum_{n=1}^n f_n h_{m,n}, \quad m = 1, 2, \dots, m.$$

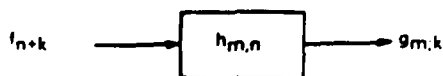


Fig. 7. Discrete Linear Transform.

Since the output g_m and input f_n can be considered as vectors, the above equation can be represented in matrix form, that is

$$\begin{bmatrix} g_0 \\ g_1 \\ g_2 \\ \vdots \\ g_{m-1} \end{bmatrix} = \begin{bmatrix} h_{0,0} & h_{0,1} & h_{0,2} & \dots & h_{0,n-1} \\ h_{1,0} & h_{1,1} & h_{1,2} & \dots & \dots \\ h_{2,0} & h_{2,1} & h_{2,2} & \dots & \dots \\ \vdots & \vdots & \vdots & \ddots & \vdots \\ h_{m-1,0} & \dots & \dots & \dots & h_{m-1,n-1} \end{bmatrix} \begin{bmatrix} f_0 \\ f_1 \\ f_2 \\ \vdots \\ f_{n-1} \end{bmatrix}$$

or abbreviated as,

$$[g_m] = [h_{m,n}][f_n],$$

where $[h_{m,n}]$ is known as a transform matrix. Thus, the different DLTs would have different transform matrices. We shall now illustrate a few frequently used DLTs.

Discrete Fourier transform (DFT)

The DFT is defined by

$$F_m = \frac{1}{N} \sum_{n=0}^{n-1} f_n \exp\left[\frac{-i2\pi mn}{N}\right],$$

$$0 \leq m \leq n-1,$$

where $h_{m,n} = \exp\left[\frac{-i2\pi mn}{N}\right]$ is also known as the transform kernel. To implement the DFT transformation in an electro-optical processor, we shall present the complex transform matrix in real elements. The corresponding real transform matrices can be written as

$$R_c[h_{m,n}] = \cos\left[\frac{2\pi mn}{N}\right],$$

and

$$Im[h_{m,n}] = \sin\left[\frac{2\pi mn}{N}\right],$$

which are the well-known discrete cosine transform (DCT) and discrete sine transformation (DST).

Discrete Hilbert transform (DHT)

It is well-known that the relationship between the real and imaginary parts of an analytic signal can be described by the Hilbert transformation. The elements of a discrete Hilbert transform (DHT) matrix can be written as

$$h_{m,n} = \begin{cases} \frac{2}{\pi} \times \frac{\sin^2[\pi(m-n)/2]}{(m-n)}, & m-n \neq 0, \\ 0, & m-n = 0. \end{cases}$$

$$m-n = 0.$$

Discrete Chirp-Z Transform (DCZT)

Another frequently used linear

transformation is the Chirp-Z transform, which can be used to compute the DFT coefficients. The elements of the DCZT transform matrix can be written as

$$h_{m,n} = \exp[i\pi(m-n)^2/N]$$

We note that this type of shift-invariant transformation, as well as other types of DLTs, can be implemented by an electro-optical processor with a systolic array processing technique.

Since the discrete linear transformation can be viewed as the result of a matrix-vector multiplication, the systolic array processing architecture

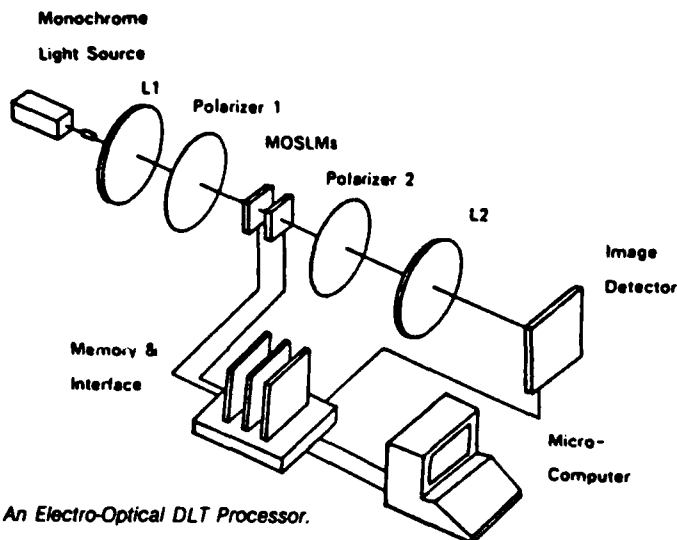


Fig. 8. An Electro-Optical DLT Processor.

can be used for the implementation of a DLT. Thus, by combining the systolic array processing technique and the two's complement representation, a DLT can be performed with an electro-optical processor as shown in Fig. 8. This technique has a high accuracy and low error rate processing capability. And it is compatible with other digital processors.

An example of a DLT using the systolic array processing technique is illustrated in Fig. 9. In Fig. 9(a), a three-sample points discrete cosine transform (DCT) matrix is encoded in the two's complement form, and multiplied with an input vector using the systolic array method. A discrete sine transformation (DST), carried out by the systolic array method, is shown in Fig. 9(b). Thus, by combining DCT and DST of Figs. 9(a) and 9(b), a discrete Fourier transform can be obtained.

Concluding remarks

Since MOSLM can be addressed in spatial parallel mode, the whole frame pattern on MOSLM can be switched in a very rapid manner: for example, 6.4 μ s for a 64 \times 64 MOSLM; 51.2 μ s for a 512 \times 512 MOSLM. By utilizing a high speed memory subsystem with a specially designed interfacing circuit, (the technology is available) a relatively slow microcomputer can be used to manipulate the parallel operation of the MOSLMs. This is known as a single instruction multiple data (SIMD) operation. In addition, with the introduction of a microcomputer into the system, a man-machine communication link is also provided. To generate the systolic array formats rapidly, a table look up structure is suggested. After the time

integrating CCD detector, a high speed analog to digital converter (ADC) and a serial-parallel deformatter would be used. Thus, by exploiting the programmability of the computer, various linear algebraic operations can be performed with this hybrid optical architecture.

Finally, by exploiting the efficient operation of optics and the programmability of electronic computer, it is the author's belief that hybrid optical architecture would be the logical approach toward modern optical computing. However, much remains to be done in the development of electro-optical devices before the hybrid optical computing can become a widespread practical reality. We hope this article will stimulate interested readers to produce more imaginative hybrid optical computing applications in the future.

Read more about it

- J. W. Goodman, A. R. Dias, and L. M. Woody, "Fully parallel,

high speed incoherent optical method for performing discrete Fourier transforms," *Opt. Lett.*, vol. 2, no. 1, 1978.

- D. Casasent and M. Carlotto, "Multidimensional adaptive radar array processing using an iterative optical matrix-vector processor," *Opt. Eng.*, vol. 21, 1982.

About the author

Francis T. S. Yu is an Evan Pugh Professor of Electrical Engineering at the Pennsylvania State University. He is an active researcher in modern optical signal processing and optical computing. He is a Fellow of IEEE, OSA, and SPIE. □

Acronym Conversion Table

ADC	— analog to digital converter
CCD	— charge coupled device
DCT	— discrete cosine transformation
DCZT	— discrete chirp - z transformation
DFT	— discrete Fourier transformation
DHT	— discrete Hilbert transformation
DLT	— discrete linear transformation
DST	— discrete sine transformation
EO	— electro-optical
LED	— light emitting diode
MO	— magneto-optic
MOSLM	— magneto-optic spatial light modulator
SIMD	— single instruction multiple data
SLM	— spatial light modulator
TTL	— transistor-transistor logic

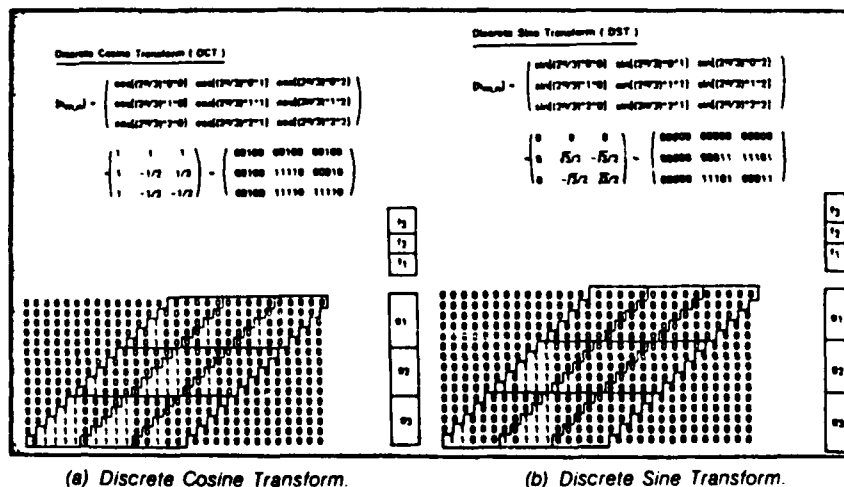


Fig. 9. Systolic Array DLT Matrix Representation.

OPTICAL BINARY ADDER USING LIQUID CRYSTAL TELEVISION

Yong JIN and Francis T.S. YU

Electro-Optics Laboratory, Electrical Engineering Department, The Pennsylvania State University, University Park, PA 16802, USA

Received 29 July 1987

This paper describes the methods of implementing an optical half-adder and a full adder utilizing programmable liquid crystal televisions (LCTV). The concept of constructing an optical full adder is based upon the realization of an optical read-only-memory (OROM). An experimental demonstration of binary number addition performed by an optical half-adder is given.

1. Introduction

Prior to our discussion, we note that the optical binary adder, when used in digital optical computing, is a basic part of the central processing unit (CPU). Methods of making an optical half-adder and full adder have been proposed by several investigators in the past few years [1,2]. Having already built a 4-bit half adder, Lohmann and Weigelt have proposed a 1-bit full adder that is based on the spatial filtering technique [1]. In order to implement a 1-bit half-adder, Khan and Nejib [2] have proposed an optical structure that employs crystal switches. In addition to these, we have recently proposed a method that performs XOR logical operations utilizing liquid crystal televisions (LCTV) [3]. The XOR logical operation is in fact a key operation in a binary adder.

The basic difference between a half-adder and a full adder is the carry-transmission. A 1-bit half-adder, however, does not require carry input. If two bits, A_i and B_i , are added together, the half-adder would produce a sum S_i , and a carry C_{i+1} , i.e., $S_i = A_i \oplus B_i$, $C_{i+1} = A_i \cdot B_i$. In a 1-bit full adder, three inputs, C_i , A_i , and B_i , would also produce a sum and a carry, i.e., $S_i = A_i \oplus B_i \oplus C_i$, and $C_{i+1} = (A_i \oplus B_i) \cdot C_i + A_i \cdot B_i$. In a n -bit full adder ($n > 1$), the carry is transferred bit by bit from the least significant bit (LSB) to the most significant bit (MSB). We stress that the main difficulty in building an n -bit optical full adder lies within the realization of carry-transmission. To

overcome this problem, the optical read-only-memory (OROM) is introduced.

In this paper, we propose a multi-channel optical half-adder using LCTVs. This optical half-adder is capable of performing the XOR, AND, NOT, and OR logical operations. An experimental demonstration of the proposed half-adder is provided. Finally, by introducing an OROM to the system, we can realize a 2-bit optical full adder.

2. An optical half-adder

The logical operations of a half-adder produce a sum S_i and a carry C_{i+1} such as

$$S_i = A_i \oplus B_i, \quad (1)$$

$$C_{i+1} = A_i \cdot B_i, \quad (2)$$

where A_i and B_i are the input bits. Since XOR and AND operations are required in a half-adder, they can easily be implemented with LCTVs as shown in fig. 1. In the optical system, two microcomputers are used in order to produce the image patterns for A and B onto two LCTVs. Two LCTVs perform the XOR operations with the polarization logic in which the logical "0's" are encoded in horizontal polarization while the logical "1's" are encoded in vertical polarization. To perform the XOR and AND operations in parallel, it is required that pattern B is written twice (e.g., B_2 is the extra copy of B in fig. 1).

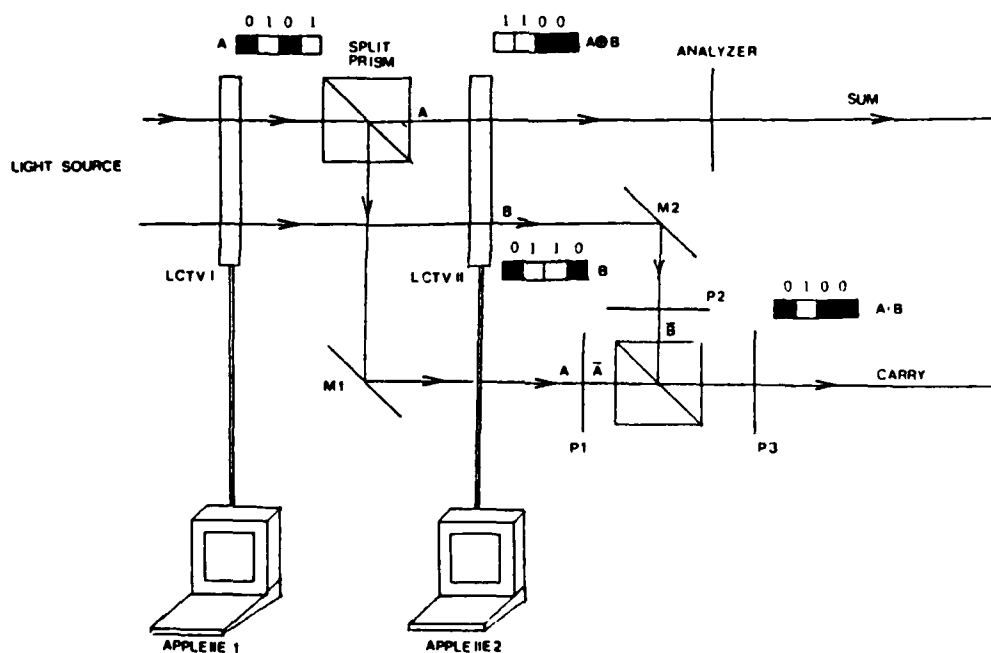


Fig. 1. An optical setup for 4-bit parallel half-adder: A, B, inputs; M1, M2, mirrors; P1, P2, P3, polarizers.

The sum, S, produced by the LCTVs is directly detected by an analyzer. The intensities of patterns A and B can be combined together to perform the logical operation OR, which is basically performed in the intensity logic. We note that a polarizer set in the contrast reverse mode can be used as a NOT gate. Therefore, an AND gate can be implemented with the optical structure shown in fig. 2. In this structure, the DeMorgan's Theorem is applied, such as,

$$X \cdot Y = \overline{\overline{X} \oplus \overline{Y}}. \quad (3)$$

In the experimental demonstrations, we used four-channel half addition in parallel. We have chosen the following values to reflect the general case.

$$A_1 = 0, \quad A_2 = 1, \quad A_3 = 1, \quad A_4 = 0; \quad (4)$$

$$B_1 = 0, \quad B_2 = 1, \quad B_3 = 0, \quad B_4 = 1. \quad (5)$$

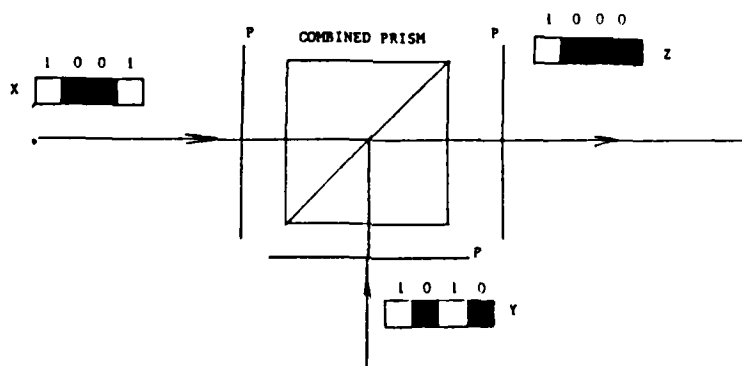


Fig. 2. An "AND" logical gate using three polarizers: X, Y, inputs; Z, output; P1, P2, P3, polarizers.

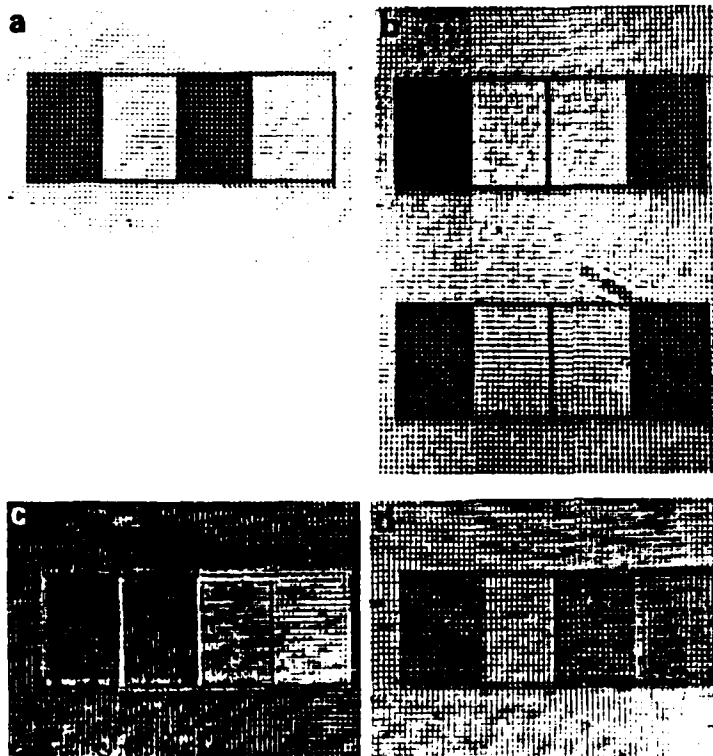


Fig. 3. An experimental demonstration of an optical half-adder: A, B, inputs; S, sum; C, carry

Consequently the output data would be,

$$S_1=0, S_2=0, S_3=1, S_4=1; \quad (6)$$

$$C_1=0, C_2=1, C_3=0, C_4=0. \quad (7)$$

The results obtained, which include two input patterns and two output patterns, are shown in fig. 3. Note that the distance between two LCTVs should satisfy the following inequality condition [3]:

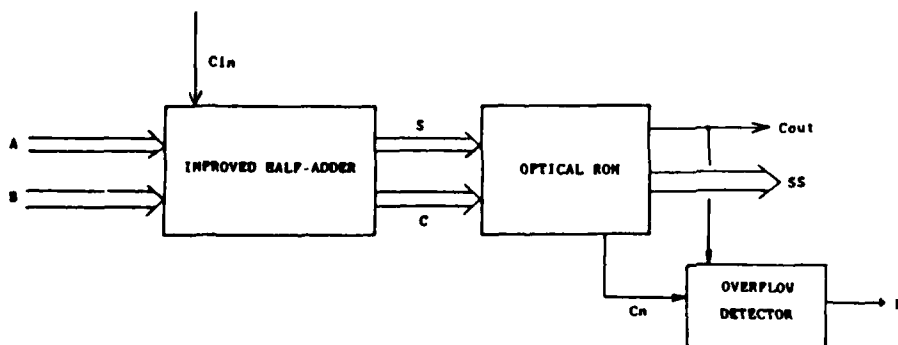


Fig. 4. A block diagram of an n -bit full adder.

$$z < d^2/\lambda, \quad (8)$$

where z is the distance between two LCTVs, d is the width of a square resolution cell, and λ is the wavelength of the light source. In our experiment, a He-Ne laser oscillating at $\lambda = 632.8$ nm is used. Since the resolution of LCTV $d = 370$ μ m, we set the distance between the LCTVs to about 20 cm (see fig. 1).

Although 15×20 pixels were used to represent 1-bit data in our experiment, fewer pixels, as small as one pixel in 1-bit, can be used in this experiment. To reduce the coherent artifact, a white light source can be used in the system [4].

3. An optical full adder

To add the new carry-in to the inputs of A and B at the LSB, the n -bit full-adder should have the capabilities of performing the carry-transmission (between the successive bits from LSB to MSB) and of detecting the overflow errors. For an n -bit full adder, S_i and C_i can be obtained by the recurrent equations,

$$SS_i = A_i \oplus B_i \oplus CC_i, \quad (9)$$

$$CC_{i+1} = (A_i \oplus B_i) \cdot CC_i + A_i \cdot B_i, \quad (10)$$

where SS_i represents the i th sum bit and CC_i denotes the i th carry output bit of a full adder.

The simplest means of implementing a full adder is to feed the carries bit by bit. This, however, is not an easy task to perform when using an optical processor. Nevertheless, with the addition of an OROM, an optical processor can perform the carry transmission, as proposed in fig. 4 and fig. 5. In other words, the OROM can allow a full adder to perform addition in parallel without feeding carries. We further note that an OROM is a digital logic device that can be implemented with any binary logical function.

In a 2-bit full adder, the sum SS and the C_{out} can be produced by S_i and C_i that have been obtained from the output of the improved half-adder. Let us now state the following relations:

$$SS_1 = A_1 \oplus B_1 \oplus C_{in} = S_1, \quad (11)$$

$$CC_2 = S_1 \cdot C_{in} + A_1 \cdot B_1 = S_1 \cdot C_{in} + C_2, \quad (12)$$

$$SS_2 = S_2 \oplus CC_2 = S_2 \cdot \overline{CC_2} + S_2 \cdot CC_2, \quad (13)$$

$$C_{out} = S_1 \cdot S_2 \cdot C_{in} + C_2 \cdot S_2 + C_1, \quad (14)$$

where A_i and B_i are the input patterns, C_{in} is the carry input, S_i and C_i are the i th output sum and carry obtained from the improved half-adder, and C_{out} is the carry output of the full adder. We stress again that the relations (11)–(14) can be implemented with an optical processor using an OROM, as shown in fig. 6. The logic diagram for this setup is illustrated in fig. 7.

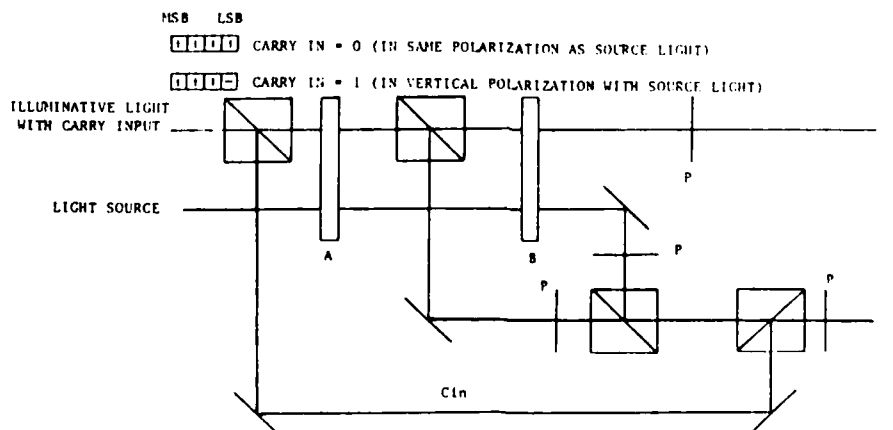


Fig. 5. An improved half-adder.

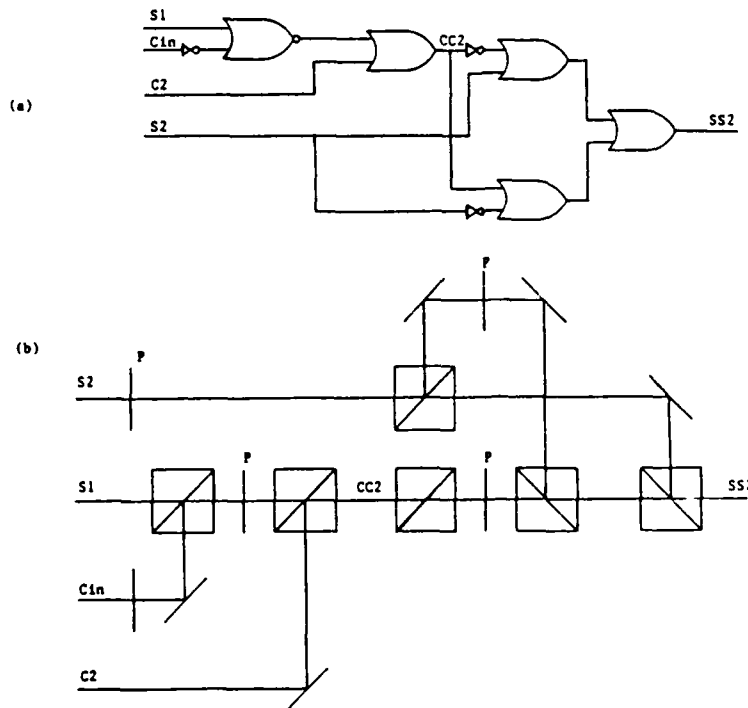
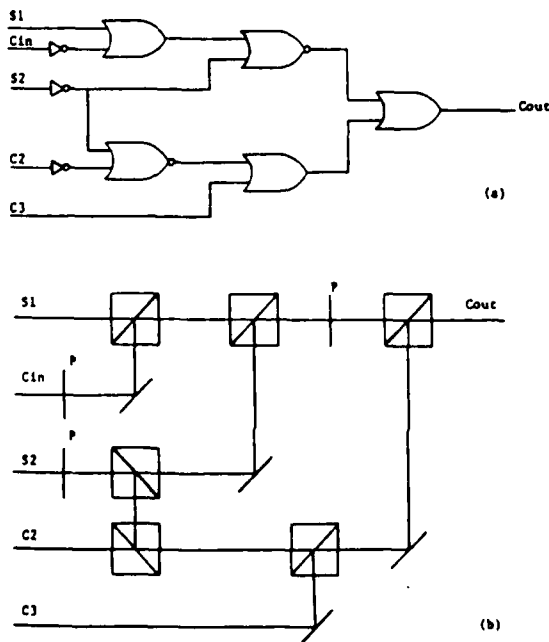


Fig. 6. Optical Implementation of an OROM for sum bit and carry out. (a) Sum bit SS_2 . (b) Carry out C_{out} .



Overflow errors occur whenever the addition of two numbers results in a sum which is too large or too small to be represented by n bits. Consequently, the detection of overflow errors is required for a full adder. This is done by utilizing the well-known rules, for an unsigned number,

$$E = C_{out} \quad (15)$$

and for a signed number,

$$E = C_n \oplus C_{n+1} \quad (16)$$

where $E=0$ and $E=1$ indicate overflow error and no overflow error respectively.

Thus, in a 2-bit full adder, we would have,

$$E = CC_2 \oplus C_{out} = CC_2 \cdot \overline{C_{out}} + \overline{CC_2} \cdot C_{out} \quad (17)$$

Fig. 7. A logic diagram of an OROM for sum bit and carry out. (a) Sum bit SS_2 . (b) Carry out C_{out} .

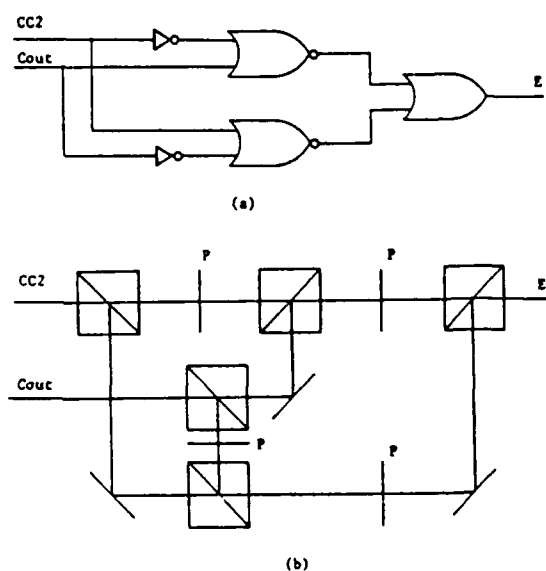


Fig. 8. An overflow detector system. (a) Logical diagram. (b) Optical implementation.

This logical operation may be performed by an optical processor using an OROM, as proposed in fig. 8.

4. Conclusion

We have demonstrated a method of building an optical half-adder using a programmable LCTV. An

experimental demonstration shows that a 4 addition can be obtained. This result shows a general case for an optical half-adder. The optical adder can be easily extended to perform n rays-number addition, by simply changing the computer program of the microcomputer. We need no extra coding procedure is required in the order, since the number was automatically entered in the LCTV. To extend a half-adder to perform an adder operation, we introduce an OROM transmission and overflow error detection optical architecture of a 2-bit full adder using an OROM is also proposed in this paper.

Acknowledgement

We acknowledge the support of the U.S. Rome Air Development Center, Hanscom Base, under contract No. F19628-87-C-001

References

- [1] A.W. Lohmann and J. Weigelt, Appl. Optics 18 (1979) 1781.
- [2] A.H. Khan and U.R. Nejid, Appl. Optics 18 (1979) 1782.
- [3] F.T.S. Yu, S. Jutamulia and D.A. Gregory, Appl. Optics 26 (1987) 2738.
- [4] F.T.S. Yu, S. Jutamulia, T.W. Lin and X.L. Huang, Opt. Eng. 25 (1986) 45.

Application of one-step holographic associative memories to symbolic substitution

Francis T. S. Yu, FELLOW SPIE
Chenhua Zhang
Suganda Jutamulia, MEMBER SPIE
The Pennsylvania State University
Electrical Engineering Department
University Park, Pennsylvania 16802

Abstract. An experimental procedure using one-step holographic associative memories to implement symbolic substitution is described. The proposed system as a whole is nonlinear. Experimental results of parallel half-addition are presented.

Subject terms: optical signal processing; optical computing; symbolic substitution; associative memories.

Optical Engineering 27(5), 399-402 (May 1988).

CONTENTS

1. Introduction
2. Background
3. Nonlinearity requirement
4. Experiment
5. Discussion
6. Conclusion
7. Acknowledgment
8. References

1. INTRODUCTION

Symbolic substitution was originally proposed by Huang¹ as a means of utilizing the parallelism of optical systems to perform digital computing. Some possible implementations of symbolic substitution have been demonstrated by Brace et al.,^{2,3} Tsao et al.,⁴ and Casasent and Botha.⁵ Recently, we proposed two methods for the optical implementation of symbolic substitution⁶ based on (1) a two-step Vander Lugt filter, which was also pointed out by Casasent and Botha⁵ and was applied by Pack and Psaltis,⁷ and (2) one-step holographic associative memories.^{7,8} In this paper, we demonstrate the experimental verification of symbolic substitution using one-step holographic associative memories.

2. BACKGROUND

Unlike Boolean logic, symbolic substitution recognizes not only a combination of bits but also their relative locations.¹ The output is not just a single bit but rather a combination of bits positioned in a particular manner. Figure 1(a) is a schematic diagram of symbolic substitution logic. Symbolic substitution is essentially a combination of recognition and substitution phases. Therefore, optical associative memories may be applied to construct a symbolic substitution logic system. In this system logical 1 and logical 0 are encoded in certain spatial patterns. For example, the logic patterns

shown in Fig. 1(a) may be encoded into the patterns shown in Fig. 1(b). This has the advantage of distinguishing logical 0 and a void space having no information.

The basic experimental setup is depicted in Fig. 2. A joint Fourier transform hologram of an input and an output pattern is first recorded as shown in Fig. 2(a). The output pattern is then generated optically by illuminating the hologram with the input pattern in the optical setup shown in Fig. 2(b). To perform a Boolean operation, the AND function, for instance, four associative memories are required, corresponding to four possible combinations of two inputs. This technique differs from the truth-table look-up optical processor,^{9,10} which basically applies the interferometric subtraction technique.

3. NONLINEARITY REQUIREMENT

Botha, Casasent, and Barnard¹¹ pointed out that a contradiction would be present if a linear holographic filter were used to perform nonlinear logic operations. To show this, we consider the symbolic substitution for the AND function. With the four possible inputs denoted as $I_{00}(x, y)$, $I_{01}(x, y)$, $I_{10}(x, y)$, and $I_{11}(x, y)$, the four AND outputs are

$$\begin{aligned} O_{00}(x, y) &= O_{01}(x, y) = O_{10}(x, y) = \text{zero}(x, y), \\ O_{11}(x, y) &= \text{one}(x, y), \end{aligned} \quad (1)$$

where $\text{zero}(x, y)$ and $\text{one}(x, y)$ are the patterns representing binary numbers 0 and 1, respectively. The input spatial functions are composed of the following:

$$\begin{aligned} I_{00}(x, y) &= \text{zero}(x - a_1, y - b_1) + \text{zero}(x - a_2, y - b_2), \\ I_{01}(x, y) &= \text{zero}(x - a_1, y - b_1) + \text{one}(x - a_2, y - b_2), \\ I_{10}(x, y) &= \text{one}(x - a_1, y - b_1) + \text{zero}(x - a_2, y - b_2), \\ I_{11}(x, y) &= \text{one}(x - a_1, y - b_1) + \text{one}(x - a_2, y - b_2), \end{aligned} \quad (2)$$

where (a_1, b_1) and (a_2, b_2) are the positions of the first and second input bits. Considering the holographic filtering as a linear system, it is seen that

$$I_{11}(x, y) = I_{01}(x, y) + I_{10}(x, y) - I_{00}(x, y), \quad (3)$$

Invited Paper SP-101 received Nov. 14, 1987; revised manuscript received Dec. 20, 1987; accepted for publication Dec. 20, 1987; received by Managing Editor Jan. 21, 1988. Portions of this paper were presented as paper 883-15 at the SPIE conference Holographic Optics: Design and Applications, Jan. 13-14, 1988, Los Angeles, Calif. The paper presented there appears (unreferenced) in SPIE Proceedings Vol. 883.

© 1988 Society of Photo-Optical Instrumentation Engineers.

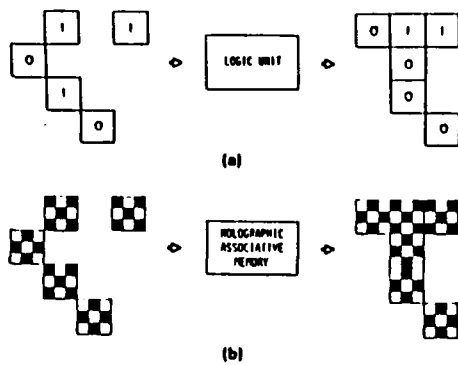


Fig. 1. (a) Schematic diagram of symbolic substitution logic. (b) Logical 1 and logical 0 encoded into certain spatial patterns.

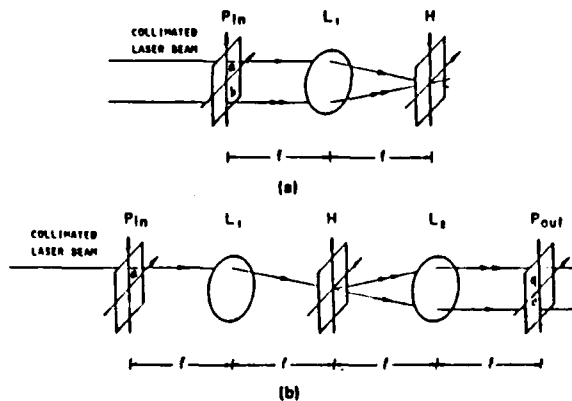


Fig. 2. (a) Recording of joint Fourier transform hologram of an input and an output pattern. (b) Reconstruction of output from an associated input pattern. Input pattern is also observed in the output plane due to the dc term of the hologram.

and the corresponding output must be

$$O_{01}(x, y) + O_{10}(x, y) - O_{00}(x, y) = \text{zero}(x, y), \quad (4)$$

which is contradictory to the logic output

$$O_{11}(x, y) = \text{one}(x, y). \quad (5)$$

To overcome this problem, the system as a whole must be nonlinear. We conducted the experiment in the same spirit as those of Refs. 5, 7, and 11 and the first method described in our previous letter,⁸ that is, as a process of independent multi-channel correlations.

4. EXPERIMENT

We used photographic film as the input transparency. Nine pixels were required to encode one bit, as depicted in Fig. 1(b). The patterns representing 1 and 0 cannot be orthogonal since the orthogonality will eliminate the association of two patterns. In other words, the two patterns must have overlapping spectra in the Fourier plane in order to yield a good holographic image.

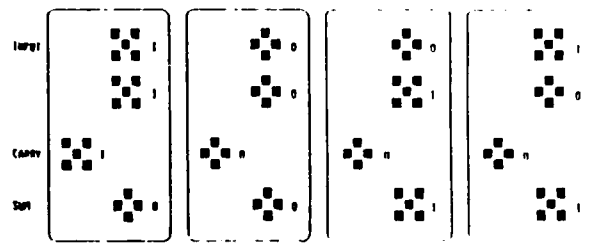


Fig. 3. Combinations of inputs and the resulting sum and carry.



Fig. 4. (a) Input pattern superimposed with a cross Ronchi grating in the spatial modulation technique. (b) Hologram indicating that multiple spectra occupy the four quadrants of the Fourier plane.

We implemented a half-adder, in which sum (XOR function) and carry (AND function) are performed simultaneously from the same data. This is an example of the realization of multiple-instruction multiple-data (MIMD) architecture utilizing the parallelism of optics. Four combinations of input and the corresponding output combinations of sum and carry are illustrated in Fig. 3. To implement four associative memories in a single hologram, we applied the spatial modulation technique,¹² in which an additional cross Ronchi grating was superimposed with the input pattern to give multiple carrier frequencies, as shown schematically in Fig. 4(a).

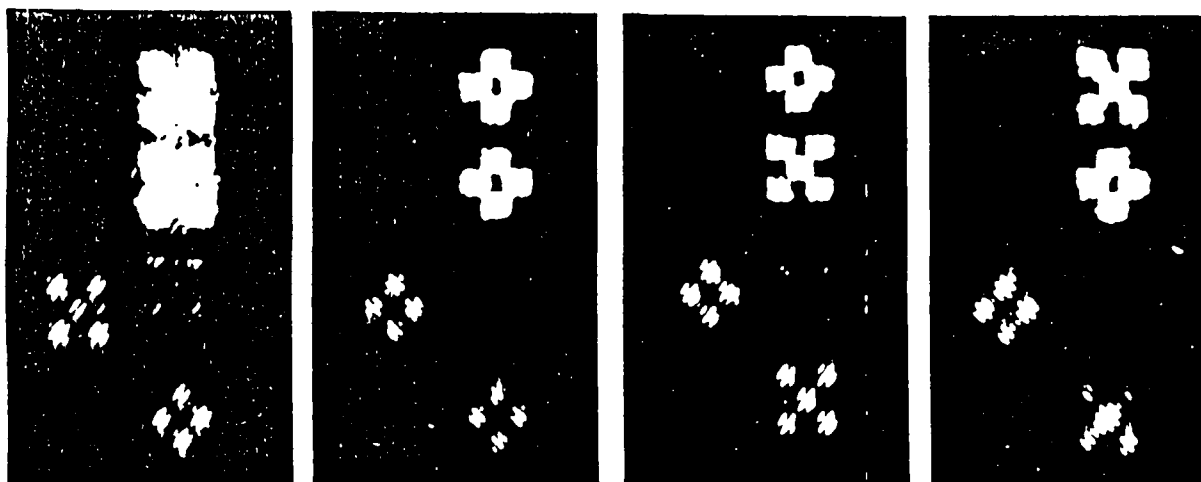


Fig. 5. Experimental results showing direct associations, obtained using only one uncovered quadrant of the hologram for each association.

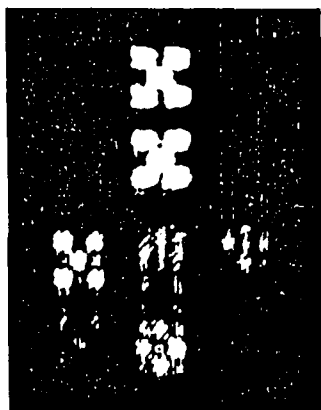


Fig. 6. Experimental result of 1+1 half-addition.

In the synthesis of the holographic filters, a mask was employed in the Fourier plane such that each input combination occupied only one quadrant of the Fourier plane, as depicted in Fig. 4(b). This multiple-spectrum configuration enhances the dynamic range of the holographic filter.¹¹ It is important to note that this multiple-spectrum configuration may also approach nonlinearity since it is very common to obtain slightly different bandwidths for different associative memories. In the final stage, a video monitor system was applied in the system to detect and threshold the hologram-generated output.

A set of experimental results is shown in Fig. 5. These direct associations were obtained using only one uncovered quadrant of the hologram for each association. To perform parallel half-addition, the entire hologram was uncovered. An example of parallel half-addition, i.e., sum and carry obtained in parallel, is shown in Fig. 6. Both Figs. 5 and 6 were taken from the video monitor after thresholding. Although cross-correlation still exists, the dominant output is the correct logic

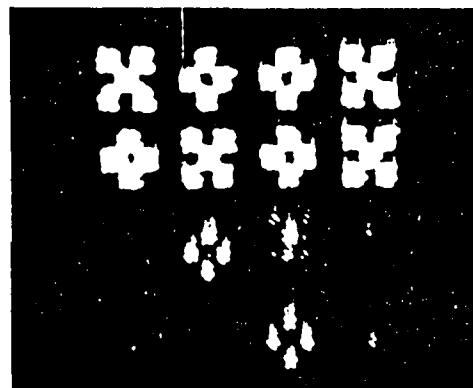


Fig. 7. Experimental result showing the association between four inputs with a filter of 0.10. Only one dominant output pattern was observed, as was expected (carry = 0, sum = 0).

pattern. Thus, it is seen from the experiments that the whole system is nonlinear. For comparison, Fig. 7 shows the output when four input combinations are associated with only one memory (only one quadrant of the hologram). The input associated with the filter produced the dominant output pattern.

5. DISCUSSION

The absence of the contradiction of linearity can be explained in the following discussion. For the case in which the input is $I_{11}(x, y)$, a quarter of the input energy (assume $\frac{1}{4}E$) will be incident on the quadrant associated with $I_{11}(x, y)$. The output $O_{11}(x, y)$ will have a total intensity of $\frac{1}{4}\alpha E$, that is

$$\iint |O_{11}(x, y)|^2 dx dy = \frac{1}{4} \alpha E, \quad (6)$$

where α is the energy diffraction efficiency of the hologram

A quarter of the input energy ($\frac{1}{4}E$) also will be incident on the quadrant associated with $I_{01}(x, y)$. Since $I_{11}(x, y) = I_{01}(x, y) + I_{10}(x, y) - I_{00}(x, y)$ [Eq. (3)], the output from this quadrant is $O_{01}(x, y)$ plus the noise $N(x, y)$ coming from the crosstalk between $I_{10}(x, y)$ and $I_{01}(x, y)$ and between $I_{00}(x, y)$ and $I_{01}(x, y)$. Therefore, the output pattern $O_{01}(x, y)$ will have a total intensity lower than $\frac{1}{4}\alpha E$. It is seen that

$$\iint |O_{01}(x, y) + N(x, y)|^2 dx dy = \frac{1}{4}\alpha E. \quad (7)$$

Thus

$$\iint |O_{01}(x, y)|^2 dx dy < \frac{1}{4}\alpha E. \quad (8)$$

The other two quadrants follow the same analysis. We may conclude that the output pattern $O_{01}(x, y) + O_{10}(x, y) - O_{00}(x, y) = \text{zero}(x, y)$ [Eq. (4)] generated from three quadrants always has lower intensity than that of the output pattern $O_{11}(x, y) = \text{one}(x, y)$ [Eq. (5)] directly generated from the quadrant associated with $I_{11}(x, y)$. Thus, a thresholding process can be applied to hardclip the total output pattern and result in a clean pattern $O_{11}(x, y)$.

6. CONCLUSION

We have demonstrated an experimental procedure to implement symbolic substitution logic using one-step holographic associative memories. In the experiment, a spatial modulation technique was applied. The spatial modulation technique gives more flexibility in the filter synthesis than the multiplexing technique since the hologram has a limited dynamic range. It is seen that the constructed system is nonlinear. A very simple example of MIMD operation, i.e., parallel half-addition, has been shown. Utilizing real-time spatial light modulators such as LCLV, LCTV, MOSLM, etc., a full addition may be realized by multistep substitution.¹ If the final cross-correlation can be totally eliminated, the proposed one-step holographic technique may be superior to the pinhole sampling technique,⁷ since the one-step technique is fully space invariant.

7. ACKNOWLEDGMENT

We acknowledge the support of the U.S. Air Force, Rome Air Development Center, Hanscom AFB, under contract F19628-87-C-0086.

8. REFERENCES

1. A. Huang, "Parallel algorithms for optical digital computers," In *Tech. Digest, 10th Int. Optical Computing Conf.*, pp. 13-17, IEEE (1981).
2. K.-H. Brenner, A. Huang, and N. Streibl, "Digital optical computing with symbolic substitution," *Appl. Opt.* 25(18), 3054 (1986).
3. K.-H. Brenner, "New implementation of symbolic substitution logic," *Appl. Opt.* 25(18), 3061 (1986).
4. M. T. Tsao, L. Wang, R. Jin, R. W. Sprague, G. Giglioli, H.-M. Kulcke, Y. D. Li, H. M. Chou, H. M. Gibbs, and N. Peyghambarian, "Symbolic substitution using ZnS interference filters," *Opt. Eng.* 26(1), 41-44 (1987).
5. D. Casasent and E. Botha, "Correlator-based optical architecture for symbolic substitution," *Opt. Commun.* To be published.
6. F. T. S. Yu and S. Jutamulia, "Implementation of symbolic substitution logic using optical associative memories," *Appl. Opt.* 26(12), 2293 (1987).
7. E. G. Pack and D. Psaltis, "Optical associative memory using Fourier transform holograms," *Opt. Eng.* 26(5), 438-443 (1987).
8. D. Gabor, "Associative holographic memories," *IBM J. Res. Dev.* 13, 156 (1969).
9. C. C. Guest and T. K. Gaylord, "Truth table look-up optical processing utilizing binary and residue arithmetic," *Appl. Opt.* 19(7), 1291 (1980).
10. C. C. Guest, M. M. Mirsatchi, and T. K. Gaylord, "EXCLUSIVE OR processing (binary image subtraction) using thick Fourier holograms," *Appl. Opt.* 23(19), 3434 (1984).
11. E. Botha, D. Casasent, and E. Barnard, "Optical symbolic substitution using multi-channel correlators," *Appl. Opt.* To be published.
12. C. Zhang, "Some applications of spatial modulation to optical information processing," *Acta Optica Sinica* 2(5), 406 (1982).
13. F. T. S. Yu, S. Jutamulia, and L. W. Lin, "Real time polychromatic signal detection using a color liquid crystal television," *Opt. Eng.* 26(5), 453-460 (1987).

Optical architecture for acousto-optic space integrating correlator

Francis T. S. Yu, FELLOW SPIE
Toshio Nagata, MEMBER SPIE
The Pennsylvania State University
Electrical Engineering Department
University Park, Pennsylvania 16802

Abstract. An architecture for a real-time signal correlation based on optical joint transform correlation is proposed. Two parallel on-plane acousto-optic (AO) cells and square-law converter are employed to produce cross correlation of two electrical signals. Arrangement of the two AO cells on the same plane permits this architecture to be implemented in a compact form. The proposed architecture has a capability of performing parallel multiple cross correlations by addition of AO cells on the input plane. The theoretical analysis and preliminary experimental results are presented.

Subject terms: signal processing; acousto-optic signal processing; joint transform correlation; digital communication.

Optical Engineering 27(7), 507-511 (July 1988).

CONTENTS

1. Introduction
2. Theory
3. Three-cell system
4. Experimental demonstrations
5. Conclusion
6. Acknowledgments
7. References

1. INTRODUCTION

Acousto-optic (AO) signal correlators have been of particular interest in such applications as matched filters, ambiguity function processors, and spectrum analyzers,¹⁻⁴ in which real-time processing is indispensable. A variety of architectures for signal correlators have been developed. These architectures can be categorized into two basic types: multiplicative and additive.⁵ In the multiplicative type, the laser beam is sequentially modulated by two successive AO cells and detected by a photodetector array. In the additive type, the laser beam is split into two paths, each of which is singly modulated by an AO cell and combined on a photodetector array where square-law mixing takes place.

This paper proposes an architecture for a real-time space integrating correlator based on the optical joint transform

correlator. Two parallel on-plane AO cells are employed to convert electrical signals into acoustic strain fields. A transform lens produces the joint transform of the optical pattern induced by the acoustic strain fields. A square-law converter, e.g., a liquid crystal light valve (LCLV), can extract the joint transform power spectrum. The inverse Fourier transform of the coherent readout of the square-law converter provides the cross correlation of input signals.⁶⁻⁸

Since two AO cells are on the same plane, the proposed architecture can be implemented in a compact system. By the addition of an adequate number of AO cells on the input plane, this architecture can be easily extended to a system that yields more than two cross correlations. This feature is important for digital communication in which different waveforms are used to represent different messages.

2. THEORY

Optical setup of the proposed correlator is shown in Fig. 1. Figure 2 depicts the geometry of the input plane. Two AO cells (AO_1 and AO_2) with dimensions a and b are inserted in the input plane with centers at $(a/2, h/2)$ and $(a/2, -h/2)$. Both AO cells are operating in Bragg regime. Narrowband input signals $s_1(t)$ and $s_2(t)$ induce acoustic strain fields in AO cells. We assume that the complex wave amplitude transmittance functions of AO_1 and AO_2 are $g_1(x, y - h/2, t)$ and $g_2(x, y + h/2, t)$, respectively, where x and y are the spatial coordinates along and perpendicular to the axis of acoustic wave propagation, h is a separation between two AO cells, and t denotes time.

Paper 2379 received Feb. 5, 1987; revised manuscript received Feb. 3, 1988; accepted for publication Feb. 3, 1988; received by Managing Editor April 19, 1988.

© 1988 Society of Photo-Optical Instrumentation Engineers.

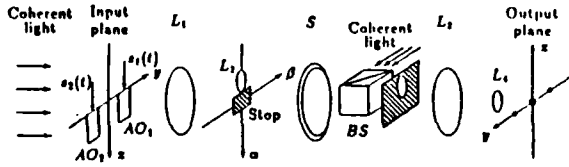


Fig. 1. Optical setup for an acousto-optic signal correlator. AO₁ and AO₂—cells; L₁ and L₃—transform lenses; L₂ and L₄—magnifying lenses; S—square-law converter; BS—beam splitter.

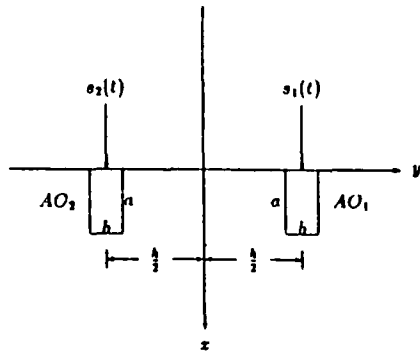


Fig. 2. Geometry of a two-cell system.

Two input signals $s_1(t)$ and $s_2(t)$ can be represented by⁹

$$\begin{aligned} s_1(t) &= a_1(t) \cos[\omega t + \phi_1(t)] \\ &= \tilde{s}_1(t) + \tilde{s}_1^*(t), \end{aligned} \quad (1)$$

$$\begin{aligned} s_2(t) &= a_2(t) \cos[\omega t + \phi_2(t)] \\ &= \tilde{s}_2(t) + \tilde{s}_2^*(t), \end{aligned} \quad (2)$$

where

$$\tilde{s}_1(t) = \frac{1}{2} \hat{a}_1(t) \exp(j\omega t), \quad (3)$$

$$\tilde{s}_2(t) = \frac{1}{2} \hat{a}_2(t) \exp(j\omega t), \quad (4)$$

$$\hat{a}_1(t) = a_1(t) \exp[j\phi_1(t)], \quad (5)$$

$$\hat{a}_2(t) = a_2(t) \exp[j\phi_2(t)]. \quad (6)$$

Here $\hat{a}_1(t)$ and $\hat{a}_2(t)$ represent complex envelopes of $s_1(t)$ and $s_2(t)$, respectively, $\phi_1(t)$ and $\phi_2(t)$ represent phases, and ω is a carrier frequency. The superscript asterisk represents the complex conjugate. The terms $\tilde{s}_1(t)$ and $\tilde{s}_2(t)$, having no negative frequency component, are the analytic signals associated with $s_1(t)$ and $s_2(t)$. The two terms of Eqs. (1) and (2) correspond to the downshifted (-1) diffraction order and upshifted ($+1$) diffraction order. Either downshifted or upshifted diffraction order can be observed in Bragg regime.⁹ In the following discussion, the downshifted components $\tilde{s}_1(t)$ and $\tilde{s}_2(t)$ are assumed.

Taking the input end of AO cells as the origin of the x -axis, $g_1(x, y, t)$ and $g_2(x, y, t)$ can be written as

$$g_1(x, y, t) = \exp \left[j\gamma \tilde{s}_1 \left(t - \frac{x}{v} \right) \right] w(x, y), \quad (7)$$

$$g_2(x, y, t) = \exp \left[j\gamma \tilde{s}_2 \left(t - \frac{x}{v} \right) \right] w(x, y), \quad (8)$$

where

$$w(x, y) = \begin{cases} 1 & 0 \leq x \leq a, -\frac{b}{2} \leq y \leq \frac{b}{2} \\ 0 & \text{otherwise} \end{cases}, \quad (9)$$

γ is the modulation depth, and v is sound velocity in AO cells. For small γ , Eqs. (7) and (8) can be approximated by the following equations¹⁰:

$$g_1(x, y, t) \approx \left[1 + j\gamma \tilde{s}_1 \left(t - \frac{x}{v} \right) \right] w(x, y), \quad (10)$$

$$g_2(x, y, t) \approx \left[1 + j\gamma \tilde{s}_2 \left(t - \frac{x}{v} \right) \right] w(x, y). \quad (11)$$

The first terms in the brackets of Eqs. (10) and (11) correspond to the undiffracted (dc or zero) orders. Since dc components are eliminated by spatial filtering, Eqs. (10) and (11) can be reduced to

$$g_1(x, y, t) \approx j\gamma \tilde{s}_1 \left(t - \frac{x}{v} \right) w(x, y), \quad (12)$$

$$g_2(x, y, t) \approx j\gamma \tilde{s}_2 \left(t - \frac{x}{v} \right) w(x, y). \quad (13)$$

Two-dimensional Fourier spectra of $g_1(x, y, t)$ and $g_2(x, y, t)$ are produced on the focal plane of lens L_1 . The light distribution $G(\alpha, \beta, t)$ at the focal plane can be shown as

$$\begin{aligned} G(\alpha, \beta, t) &= \mathcal{F} \left\{ g_1 \left(x, y - \frac{h}{2}, t \right) + g_2 \left(x, y + \frac{h}{2}, t \right) \right\} \\ &= \exp \left(-\frac{j h \beta}{2} \right) G_1(\alpha, \beta, t) + \exp \left(\frac{j h \beta}{2} \right) G_2(\alpha, \beta, t), \end{aligned} \quad (14)$$

where \mathcal{F} denotes the 2-D spatial Fourier transform operator and $G_1(\alpha, \beta, t)$ and $G_2(\alpha, \beta, t)$ are the Fourier spectra of $g_1(x, y, t)$ and $g_2(x, y, t)$, respectively.

Interference fringes will be generated by superposition of $G_1(\alpha, \beta, t)$ and $G_2(\alpha, \beta, t)$. Lens L_3 will magnify these fringes onto the square-law converter S. The intensity distribution at the output end of the square-law converter can be written as

$$\begin{aligned} |G(\alpha, \beta, t)|^2 &= |G_1(\alpha, \beta, t)|^2 + |G_2(\alpha, \beta, t)|^2 \\ &\quad + \exp(-j h \beta) G_1(\alpha, \beta, t) G_2^*(\alpha, \beta, t) \\ &\quad + \exp(j h \beta) G_1^*(\alpha, \beta, t) G_2(\alpha, \beta, t), \end{aligned} \quad (15)$$

where the magnification constant is omitted for simplicity.

The coherent readout of the square-law converter induces a light field proportional to $|G(\alpha, \beta, t)|^2$. Since side lobes of $|G(\alpha, \beta, t)|^2$ are negligible, a circular spatial filter in front of lens L_3 , which extracts interference fringes around the main lobe of $|G(\alpha, \beta, t)|^2$, can be employed to reduce the dc level of the output. The transfer function of this spatial filter $W'(\alpha, \beta)$ and its impulse response $w'(x, y)$ are given by

$$W'(\alpha, \beta) = \begin{cases} 1 & \alpha^2 + \beta^2 \leq \frac{d^2}{4} \\ 0 & \text{otherwise} \end{cases} \quad (16)$$

$$w'(x, y) = \frac{\pi d}{\rho} J_1\left(\frac{\rho d}{2}\right) \quad (17)$$

where

$$\rho^2 = p^2 + q^2 \quad (18)$$

J_1 is the first-order Bessel function of the first kind, and d is the diameter of the circular aperture.

The complex light distribution at the output plane can be shown as

$$g(x, y, t) = [R_{11}(x, y, t) + R_{22}(x, y, t) + R_{12}(x, y - h, t) + R_{21}(x, y + h, t)] \cdot w'(x, y) \quad (19)$$

where

$$R_{ij}(x, y, t) = \mathcal{F}^{-1} \{ G_i(\alpha, \beta, t) G_j^*(\alpha, \beta, t) \} \\ = \int_{-\infty}^{+\infty} \int_{-\infty}^{+\infty} g_i(\alpha + x, \beta + y, t) g_j^*(\alpha, \beta, t) d\alpha d\beta \quad (20)$$

and the asterisk and the superscript asterisk represent the convolution operation and the complex conjugate, respectively. R_{11} and R_{22} are the autocorrelation functions that appear at the origin of the output plane. R_{12} and R_{21} are the cross-correlation terms that are centered around $y = h$ and $y = -h$, respectively. We note that these cross-correlation patterns are magnified by lens L_4 for convenience of the observation.

By substituting Eqs. (3) and (4) into Eqs. (12) and (13) and ignoring the window effect (both w and w'), the intensity distribution at $y = h$ can be written as

$$|R_{12}(x, 0, t)|^2 = \left| \int_{-\infty}^{+\infty} \int_{-\infty}^{+\infty} g_1(\alpha + x, \beta, t) g_2^*(\alpha, \beta, t) d\alpha d\beta \right|^2 \\ = \gamma^2 h^2 \left| \int_{-\infty}^{+\infty} \tilde{s}_1\left(t - \frac{\alpha + x}{v}\right) \tilde{s}_2^*\left(t - \frac{\alpha}{v}\right) d\alpha \right|^2 \\ = \frac{\gamma^2 h^2}{16} \left| \int_{-\infty}^{+\infty} \tilde{a}_1\left(t - \frac{\alpha + x}{v}\right) \tilde{a}_2^*\left(t - \frac{\alpha}{v}\right) d\alpha \right|^2 \\ = \frac{\gamma^2 h^2 v^2}{16} \left| r_{12}\left(-\frac{x}{v}, t\right) \right|^2 \quad (21)$$

where

$$r_{12}(x, t) = \int_{-\infty}^{+\infty} \tilde{a}_1(t + \alpha + x) \tilde{a}_2^*(t + \alpha) d\alpha \quad (22)$$

Therefore, except for the window function, the correlation peak intensity is proportional to the square value of the cross correlation of \tilde{a}_1 and \tilde{a}_2 .

If signal duration is longer than the cell length or the effect of $w(x, y)$ is not ignorable, only partial correlation can be obtained. We note that the cross correlation can be obtained only if the frame rate of the square-law converter is sufficiently high. For example, if the signal takes 10 μ s to fulfill the aperture of the AO cell, the necessary frame rate is about 100 kHz. Unfortunately, with the current stage of technology, such a high frame rate is not achievable in existing square-law converters.

Let us consider the special case where $s_1(t) = s_2(t) = 2A \cos \omega t$. This simple case is important for an application to the particular digital communication system such as the frequency shift keying, in which the frequency carries the signal information. The analytic signal of $2A \cos \omega t$ is given by

$$\tilde{s}(t) = A \exp(j\omega t) \quad (23)$$

We get the joint transform power spectrum as

$$|G(\alpha, \beta)|^2 = 2\gamma^2 \Lambda^2 \left| W\left(\alpha + \frac{\omega}{v}, \beta\right) \right|^2 \\ + \exp(-j\beta h) \gamma^2 \Lambda^2 \left| W\left(\alpha + \frac{\omega}{v}, \beta\right) \right|^2 \\ + \exp(j\beta h) \gamma^2 \Lambda^2 \left| W\left(\alpha + \frac{\omega}{v}, \beta\right) \right|^2 \\ = 2\gamma^2 \Lambda^2 \left| W\left(\alpha + \frac{\omega}{v}, \beta\right) \right|^2 (1 + \cosh \beta h) \quad (24)$$

$$W(\alpha, \beta) = ab \exp\left(-j \frac{a\alpha}{2}\right) \text{sinc}\left(\frac{a\alpha}{2\pi}\right) \text{sinc}\left(\frac{b\beta}{2\pi}\right) \quad (25)$$

where $W(\alpha, \beta)$ is the Fourier transform of the rectangular window function $w(x, y)$. Time variable t is omitted since $|G(\alpha, \beta, t)|^2$ is assumed to be quasi time independent. The inverse Fourier transform of Eq. (24) can be shown as

$$g(x, y) = \gamma^2 \Lambda^2 \exp\left(-j \frac{\omega}{v} p\right) \\ \times [2R(x, y) + R(x, y - h) + R(x, y + h)] \quad (26)$$

where

$$R(x, y) = w(x, y) \otimes w(x, y) \\ = \begin{cases} (a - |x|)(b - |y|) & |x| \leq a, |y| \leq b \\ 0 & \text{otherwise} \end{cases} \quad (27)$$

and \otimes denotes the correlation operation.

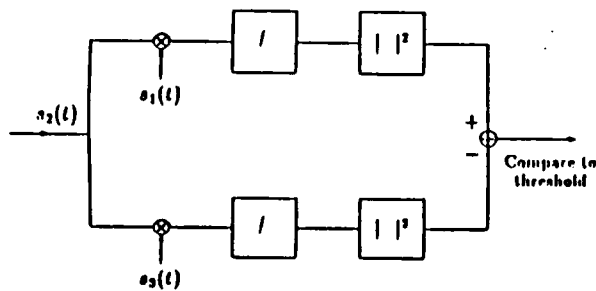


Fig. 3. Correlation receiver.

3. THREE-CELL SYSTEM

The system discussed above is easily extended to a three-cell system where three parallel AO cells (AO_{1-3}) are placed at the input plane. We assume that the separation between AO_1 and AO_2 is h_1 and between AO_2 and AO_3 is h_2 . For simplicity, we neglect the window effect in the following discussion.

Three electrical signals s_1 , s_2 , and s_3 fed into three cells induce complex wave transmittance functions g_1 , g_2 , and g_3 , respectively. On the focal plane of the Fourier transform lens, the light distribution is obtained, similarly to Eq. (14), as

$$G(\alpha, \beta, t) = \exp(-jh_1\beta)G_1(\alpha, \beta, t) + G_2(\alpha, \beta, t) + \exp(jh_2\beta)G_3(\alpha, \beta, t). \quad (28)$$

At the output plane, we obtain spatially separated cross-correlation functions that correspond to each pair of s_1 , s_2 , and s_3 at points $(0, \pm h_1)$, $(0, \pm h_2)$, and $(0, \pm(h_1 + h_2))$. We note that to prevent the correlation distributions from overlapping each other, h_1 and h_2 must be sufficiently far apart. The expansion of the above discussion to a multicell correlator is apparent.

The three-cell system may be significant for a digital communication system in which two different waveforms are selected for transmission to the receiver. Suppose that s_1 and s_3 are possible waveforms to be transmitted and that s_2 is a signal received by the observer. Since the intensity of each correlation peak is proportional to the intensity of the correlation function, the received signal can be interpreted by a simple decision rule,¹⁰ such as

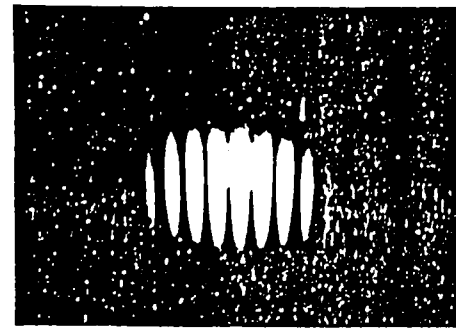
choose s_1 if intensity at $(0, h_1) > \text{intensity at } (0, h_2)$,

choose s_3 otherwise.

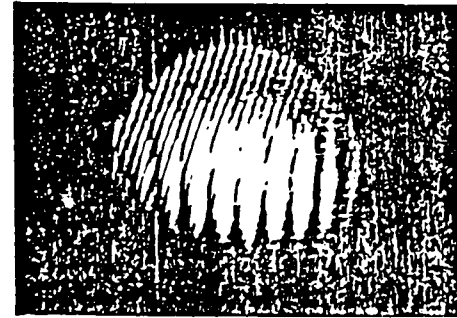
A block diagram representation of the correlator is shown in Fig. 3.

4. EXPERIMENTAL DEMONSTRATIONS

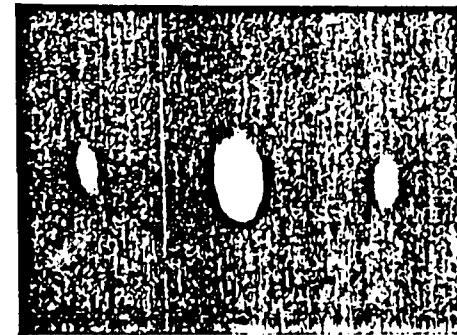
The experiment was conducted with the setup shown in Fig. 1. We used an LCLV as a square-law converter. Since the response time of the LCLV is slow, the system can be made to operate only for periodic signals. A pure sinusoidal signal at frequency 65 MHz was applied to both AO cells as input signals because the sinusoidal signal makes the experiment relatively simple. The separation h between two AO cells was about 15 mm. The aperture dimensions $a = 5$ mm and $b = 3$ mm were selected to be sufficiently small so that a larger main lobe can be obtained [see Eq. (25)].



(a)



(b)



(c)

Fig. 4. Experimental results: (a) Written in interference fringes, (b) read-out interference fringes, and (c) output correlation peaks; the center spot is the zero-order diffraction

Figure 4(a) shows the interference fringes produced by the phase difference of modulated light coming from both cells. The cosine term of Eq. (24) shows that the fringe size is equal to $\lambda f/h$, where f is the focal length of lens L_1 and λ is the wavelength of illumination. Figure 4(b) shows interference fringes written onto the LCLV. The small oblique fringes in the background represent interference due to internal reflections within the LCLV. Since the spatial frequencies of these fringes are different, the internal interference can be eliminated by spatial filtering. Figure 4(c) shows the output correlation peaks obtained with the setup of Fig. 1.

5. CONCLUSION

We have demonstrated an optical architecture that can be applied to acousto-optic space integrating correlation. The correlation peaks corresponding to each pair of input signals

can be read out simultaneously at the output plane with a CCD array camera for signal interpretation. The on-plane structure of the proposed time-signal optical correlator would enable us to implement the system in a small package by using relatively few optical components. This system may be applicable to spread spectrum communication as a frequency hopping signal receiver.

6. ACKNOWLEDGMENTS

We acknowledge the support of the U.S. Air Force, Rome Air Development Center, Hanscom Air Force Base, under contract F19628-87C-0086 and the Westinghouse Electric Corporation for providing the AO cells.

7. REFERENCES

1. W. I. Maloney, "Acoustooptical approaches to radar signal processing," *IEEE Spectrum* 6, 40-48 (1969).
2. J. N. Lee, "Optical and acousto-optical techniques in radar and sonar," in *Optical Computing*, J. A. Nell, ed., Proc. SPIE 456, 96-104 (1984).
3. I. M. Turpin, "Spectrum analysis using optical processing," *Proc. IEEE* 69, 79-92 (1981).
4. R. A. Sprague, "A review of acousto-optic signal correlators," *Opt. Eng.* 16(5), 467-474 (1977).
5. N. J. Berg and J. N. Lee, *Acousto-Optic Signal Processing*, Marcel Dekker, New York (1983).
6. C. S. Weaver and J. W. Goodman, "A technique for optically convolving two functions," *Appl. Opt.* 5, 1248-1249 (1966).
7. F. T. S. Yu and X. J. Lu, "A real-time programmable joint transform correlator," *Opt. Commun.* 52, 10-15 (1984).
8. F. T. S. Yu and J. E. Ludman, "Microcomputer-based programmable optical correlator for automatic pattern recognition and identification," *Opt. Lett.* 11, 395-397 (1986).
9. W. I. Rhodes, "Acousto-optic signal processing: convolution and correlation," *Proc. IEEE* 69, 65-78 (1981).
10. A. D. Whalen, *Detection of Signals in Noise*, Academic Press, Orlando, Fla. (1971).

OPTICAL ENGINEERING EDITORIAL SCHEDULE

August 1988

Photomechanics II

Fu-Pen Chiang
SUNY/Stony Brook
Lab. for Experimental Mechanics Research
Stony Brook, NY 11794
516/632-8311

September 1988

Multiple-Aperture Optical Systems

Janet S. Fender
U.S. Air Force Weapons Lab.
Optical Phased Array Branch
Kirtland AFB, NM 87117-6008
505/844-9831

October 1988

Contributed papers on optical engineering

November 1988

Optical Design

Carmina Londoño and
Jon Vantassel
Polaroid Corporation
38 Henry Street
Cambridge, MA 02139
617/577-4115

December 1988

Contributed papers on optical engineering

January 1989

Optical Computing

Sing H. Lee
Electrical & Computer
Engineering
Univ. of California,
San Diego
La Jolla, CA 92093
619/534-2413

Ravindra A. Athale
BDM Corporation
7915 Jones Branch Dr.
McLean, VA 22102-3396
703/848-7556

February 1989

Polarization Considerations for Optical Systems

Russell A. Chipman
Center for Applied Optics
University of Alabama in Huntsville
Huntsville, AL 35899
205/895-6307

MFSK SIGNAL DETECTION USING ACOUSTO-OPTIC JOINT TRANSFORM CORRELATOR

Francis T. S. Yu and Toshio Nagata
Department of Electrical Engineering
The Pennsylvania State University
University Park, Pennsylvania 16802

KEY TERMS

Acousto-optic cell, joint transform correlator, frequency shift keying, signal detection

ABSTRACT

A multichannel acousto-optic joint transform correlator is presented. On-plane acousto-optic (AO) cells and a square law converter are employed. The AO cells are driven by frequency multiplexed temporal signals to produce spatially modulated signals. The joint transform power spectrum is generated with a square law converter. By inverse Fourier transformation with a coherent readout, the cross correlation of input signals can be obtained. Since the architecture can process wideband signals, it may be applied to detect multiple frequency shift keying (MFSK) signals.

1. INTRODUCTION

Recently, we have introduced an optical architecture for an acousto-optic (AO) correlator based on optical joint transform correlation [1]. Two parallel on-plane AO cells were used to produce cross correlation between two temporal signals. We have noted that the proposed system is capable of processing signals that are modulated by frequency shift keying (FSK).

In this article we will expand the concept for a multiple AO cell system that deals with multiple frequency signals, so that higher communication throughput can be obtained. The proposed multicell, multifrequency system is suitable for the application of detecting multiple frequency shift keying (MFSK) communication signals.

2. ARCHITECTURE

Figure 1(a) shows a schematic diagram of an acousto-optic joint transform correlator (AJTC). This system consists of an array of AO cells at the input plane and a liquid crystal light valve (LCLV) which acts as a square-law detector for the composite Fourier to power spectrum conversion. The geometrical locations of the AO cells at the input plane are depicted in Figure 1(b). One of the AO cells, which is referred to as a reference cell, is driven by a local reference signal $s_0(t)$. We assume $N - 1$ number of signals $s_n(t)$, received from a communication path, are fed into the other $N - 1$ AO cells, which are called signal cells. If all the signal cells are equally spaced on the right-hand side of the input plane, the reference cell would be placed on the left-hand side at a distance Nh apart from the optical axis, where h is the spacing of the signal cells. Thus, the cross correlations among received signals would be diffracted within a distance $(N - 2)h$ from the optical axis, while the cross correlation between reference and received signals would be diffracted away from those undesired correlation spots.

Now assume that the input signals $s_n(t)$ are narrowband signals, which can be decomposed into the sum of two analytic signals

$$s_n(t) = \tilde{s}_n(t) + \tilde{s}_n^*(t) \quad n = 0, 1, 2, \dots, N - 1 \quad (1)$$

The corresponding transmittance functions of the AO cells can be approximated by [2]

$$g_n(x, y, t) = j\gamma \tilde{s}_n(t - x/v) w_n(x, y) \quad n = 0, 1, 2, \dots, N - 1 \quad (2)$$

where γ and $w_n(x, y)$ are the modulation depth and the

window function of the AO cells, respectively. Note that the window function represents not only the aperture size, but also includes the uniformity of illumination, misalignment factor, and roughness of the crystal. Thus, the light distribution emerging from the AO cells can be written as

$$e(x, y, t) = g_0(x, y + (N - 1)h, t) + \sum_{n=1}^{N-1} g_n(x, y - h(n - 1), t) \quad (3)$$

The Fourier transform of the above equation, through a transform lens L_1 , can be projected onto the input end of a square-law converter (i.e., LCLV). The lens L_2 was used to magnify the joint Fourier spectra, such that the interference fringes would be within the resolution limit of the LCLV. Since the readout light field of the square-law converter is proportional to the square modulus of this Fourier transform, we have

$$\begin{aligned} |E(\alpha, \beta, t)|^2 = & \sum_{n=0}^{N-1} |G_n(\alpha, \beta, t)|^2 \\ & + \sum_{n=1}^{N-1} G_0(\alpha, \beta, t) G_n^*(\alpha, \beta, t) \\ & \times \exp[jh(N + n - 2)] \\ & + \sum_{n=1}^{N-1} G_0^*(\alpha, \beta, t) G_n(\alpha, \beta, t) \\ & \times \exp[-jh(N + n - 2)] \\ & + \sum_{n=1}^{N-1} \sum_{m=1}^{N-1} G_n(\alpha, \beta, t) G_m^*(\alpha, \beta, t) \\ & \times \exp[-jh(n - m)] \end{aligned} \quad (4)$$

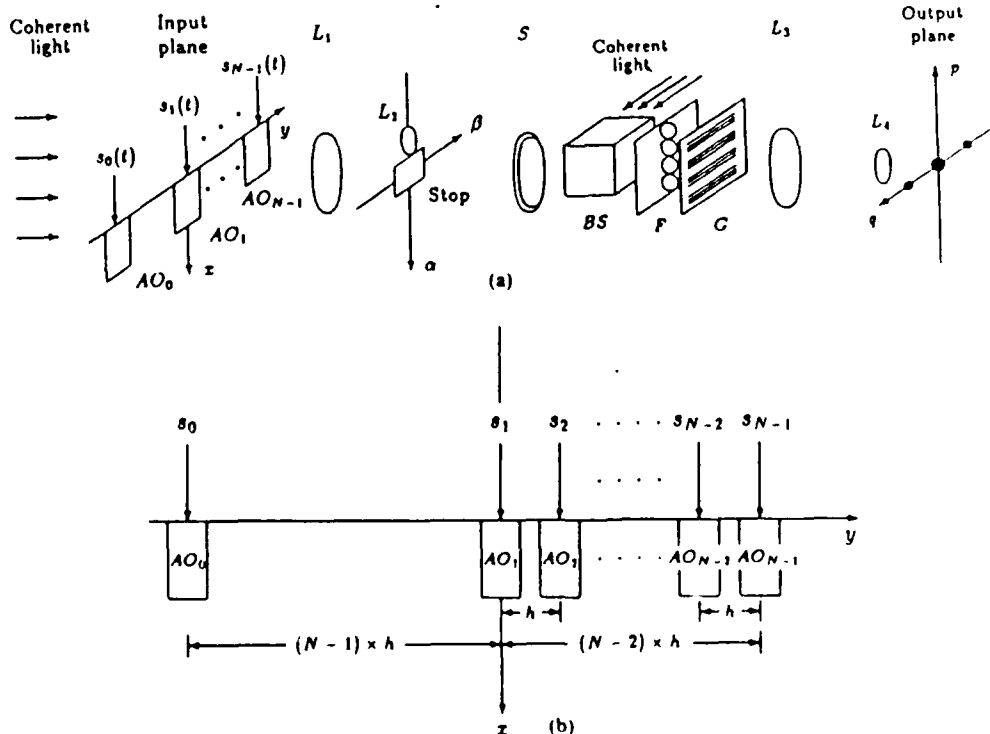


Figure 1 (a) Multicell, multifrequency acousto-optic joint transform correlator: AO_0, \dots, A_{N-1} , acousto-optic cells; L_1 and L_2 , transform lenses; L_3 and L_4 , magnification lenses; S , square-law converter; BS , beam splitter; F , spatial filter; G , grating (b) The input plane geometry of the multicell system

where $G_n(\alpha, \beta, t)$ are Fourier transform of $g_n(x, y, t)$.

The complex light distribution at the output plane would be

$$\begin{aligned}
 e(p, q, t) = & \sum_{n=0}^{N-1} R_{nn}(p, q, t) \\
 & + \sum_{n=1}^{N-1} R_{0n}(p, q + h(N + n - 2), t) \\
 & + \sum_{n=1}^{N-1} R_{n0}(p, q - h(N + n - 2), t) \\
 & + \sum_{n=1}^{N-1} \sum_{m=1}^{N-1} R_{nm}(p, q - h(n - m), t) \quad (5)
 \end{aligned}$$

where

$$\begin{aligned}
 R_{nm}(p, q, t) = & \int_{-\infty}^{+\infty} \int_{-\infty}^{+\infty} g_n(\alpha + p, \beta + q, t) \\
 & \times g_m^*(\alpha, \beta, t) d\alpha d\beta \quad (6)
 \end{aligned}$$

The first summation of Eq. (5) represents the autocorrelation terms of the input signals, which are diffracted at the origin of the output plane. The second and third summations correspond to the cross correlations between the reference and the input signal terms, which are diffracted in the vicinity of $(0, \pm h(N + n - 2))$. These correlation spots can be separated if the spacing h is sufficiently large. The last summation represents the undesired cross correlations of the input signals, which would be diffracted within the distance $(N - 2)h$ from the optical axis. Notice that these terms are separated from the desired reference to input signal correlation spots.

Also note that the correlation spots from the second and third summations represent the frequency content of the input signals, if they match the reference frequencies. The position of each correlation spot indicates that the signal cell has the same frequency components as the reference cell. Because the frequency components are diffracted to the same correlation spots, the actual temporal frequencies cannot be determined.

To overcome this problem, gratings of different spatial frequencies are added behind the square-law converter as shown in Figure 1(a). A linear array of bandpass spatial filters were also introduced to reduce the zero-order diffraction component. Since the AO cells diffract incident light at different angles, a series of Fourier spectra along the vertical axis can be obtained. If a signal contains one of the frequency components of the reference cell, linear interference fringes would be produced in the corresponding Fourier spot, which determines the horizontal location of the output correlation spots. The gratings behind the square-law converter will separate the superimposed correlation spots in the vertical direction. One of the possible arrangements of the output correlation spots is shown in Figure 2. The correlation spots within the dashed box represent the frequency content of the input signal cells.

Two experimental demonstrations using the three AO cells were conducted in our laboratory, where the center cell was used as the reference signal. In the first demonstration, a signal with frequencies of 50 MHz and 49.75 MHz was applied to all the AO cells. Circular spatial filters 4 mm in

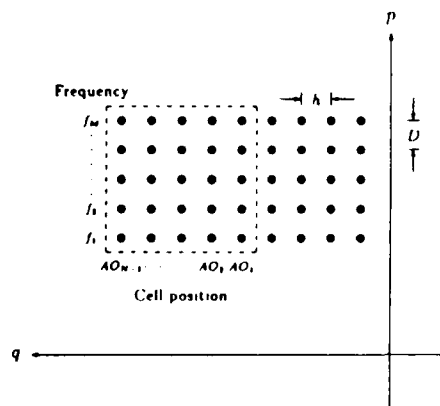
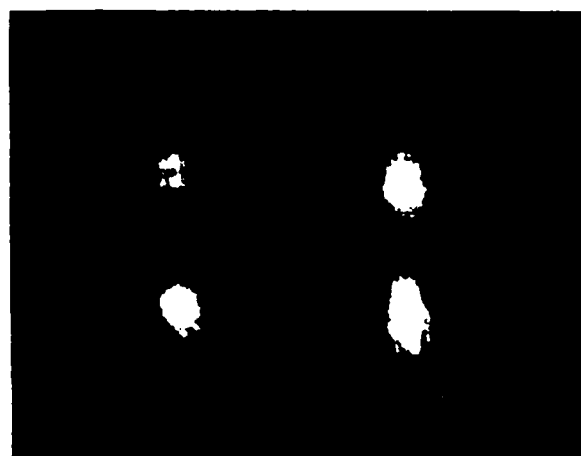
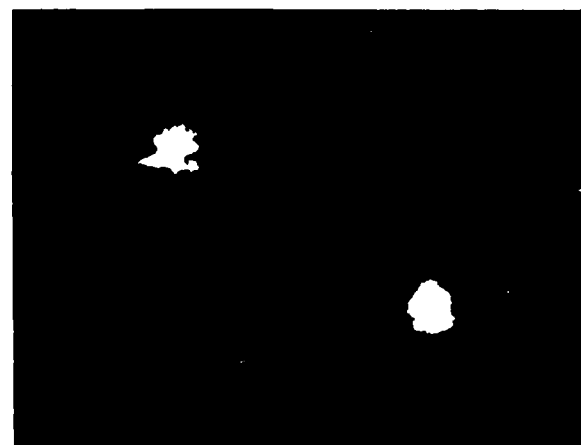


Figure 2 Output correlation spots



(a)



(b)

Figure 3 Experimental results for a three-cell system (a) Output correlation spots obtained with matching two frequencies (b) Output correlation spots obtained with matching one of the frequencies

diameter and grating frequencies of 4 and 8 lines/mm were used in the experiment. For convenient illustration, photographic film was used as the square-law converter. Figure 3(a) shows the four output correlation spots obtained with this experiment. In the second experimental demonstration, signals of 50 MHz and 49.75 MHz were respectively applied to each of two signal cells. Output correlation spots corresponding to each of the applied frequencies are shown in Figure 3(b). The frequency content of the signal cells can be identified.

3. RECEIVER CONFIGURATION

Since efficient diffraction by the AO cell occurs at the Bragg angle, the signal should be implemented around the Bragg frequency. The incoming wideband signal is divided into small subbands that fit into the bandwidth of AO cells. The center frequency of each subband is then translated to the Bragg frequency before being input to the AO cells. We assume that there are $N \pm 1$ signal cells and that each subband has M frequency-division channels. Then the system can deal with $M(N - 1)$ channels simultaneously.

A block diagram of the proposed receiving system is illustrated in Figure 4. The first frequency converter selects the appropriate communication band, and demodulates the signal to the intermediate frequency which is the Bragg frequency of the system. The secondary frequency converters are used to translate the center frequency of the subbands to the appropriate Bragg frequency of the AO cells. After bandpass filtering, these signals are fed into an array of AO cells. Output correlation spots can be read out by photodiode array detectors. By passing these detected correlation spots through a thresholding logic network, the highest probable received signal can be displayed at the system output. The basic bottleneck of the proposed system is the square-law converter

(e.g., LCLV), in which the response time is in the order of milliseconds.

4. CONCLUSION

In conclusion we would like to point out that the proposed architecture is capable of processing very wide bandwidth temporal signals, as high as 10^6 resolution elements. The proposed AO correlator can be synthesized in compact form. The operation of the system is rather simple, for it eliminates the complicated electronics circuitry usually required for data processing. However, the proposed system requires the availability of a square-law converter with higher speed and larger dynamic range. Thus, the realization of a practical joint transform AO correlator for MFSK communication applications would be dependent upon the rapid development of a qualified device in the future.

5. ACKNOWLEDGMENTS

We acknowledge the support of the U.S. Air Force Rome Air Development Center, Hanscom Air Force Base, under contract F19628-87-0086.

REFERENCES

1. F. T. S. Yu and T. Nagata, "An Optical Architecture for Acousto-Optic Space Integrating Correlator," *Opt. Eng.*, Vol. 27, 1988, to be published.
2. W. T. Rhodes, "Acousto-Optic Signal Processing: Convolution and Correlation," *Proc. IEEE*, Vol. 69, 1981, pp. 65-78.

Received 5-19-88

Microwave and Optical Technology Letters, 1/6, 190-193
© 1988 John Wiley & Sons, Inc.
CCC 0895-2477/88/\$4.00

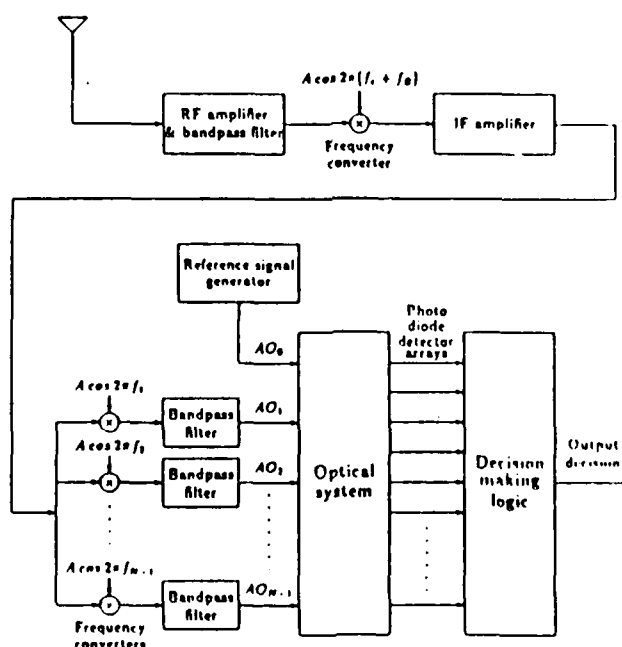


Figure 4 A black box representation of an acousto-optic frequency hopping signal receiver

Letters to the Editors should be addressed to the Editor, APPLIED OPTICS, Georgia Institute of Technology, Atlanta, GA 30332-0252. If authors will state in their covering communications whether they expect their institutions to pay the publication charge, publication time should be shortened (for those who do).

Multiple channel optical correlator via rotating grating on LCTV

Francis T. S. Yu, Qihou Zhou, and Chenhua Zhang

Pennsylvania State University, Department of Electrical Engineering, University Park, Pennsylvania 16802.

Received 20 November 1987.

0003-6935/88/183770-03\$02.03/0.

© 1988 Optical Society of America.

Optical signal detection by complex spatial filtering can be traced back to 1964, when it was developed by VanderLugt.¹ Since then the concept has been widely used for various types of large-capacity optical correlator.²⁻⁶ One of them is a scanning correlator system using a rotating grating.⁴⁻⁶ Gregory and Huckabee reported a correlator addressed by an acoustooptic cell.⁷ Recently liquid crystal television (LCTV) has found some interesting applications to optical signal processing, e.g., optical pattern recognition and adaptive joint transform correlation.⁸⁻¹⁰ In this Letter we propose a technique in which a scanning grating⁴ can be easily imposed on an LCTV screen with a microcomputer. The setup is depicted in Fig. 1. The proposed system overcomes the positioning difficulty caused by either the mechanical movement or the frequency shift in the techniques mentioned above.²⁻⁶

Because the low resolution of LCTV limits the spatial carrier frequency, we use a new setup which is little different from a conventional optical correlator. The lens system L_2 -

L_3 is used to project a reduced image of the LCTV grating onto the input plane of the optical correlator, so that the Fourier transform of the object can be of the proper scale while the spatial frequency spectrum of the grating is magnified. The different diffraction orders on the frequency plane can, therefore, be sufficiently separated. We further note that the pixel size of the LCTV is $\sim 390 \mu\text{m}$, so the highest spatial modulating frequency for the input object in a conventional 4- f system is ~ 1.25 lines/mm. In our system, a carrier frequency of 12 lines/mm is obtained. A higher carrier frequency can be achieved by adjusting the lens system, and the spatial-bandwidth-product of the system remains the same. The transmittance of the LCTV grating image, including the polarizers, can be approximately written as

$$u(x,y) = K_1 + K_2 \left[\text{rect} \left(\frac{x}{a}, \frac{y}{b} \right) \cdot \text{comb} \left(\frac{x}{c}, \frac{y}{d} \right) \right] \times \left[\text{rect} \frac{X}{g} \cdot \text{comb} \frac{X}{h} \right], \quad (1)$$

where K_1 and K_2 are proportionality constants, a, b are the pixel image size in the x and y directions, respectively, c, d are the distances between the centers of adjacent pixel images, g and h are the width and spacing of the image grating grooves, and X represents the orientation of the grating vector, which is given by

$$X = x \cos \theta + y \sin \theta. \quad (2)$$

The Fourier transform of the input object with the modulating function of Eq. (1) can be written as

$$U(f_x, f_y) = V(f_x, f_y) \cdot [\delta(f_x, f_y) + \text{sinc}(af_x, bf_y) \text{comb}(cf_x, df_y)] \times [\text{sinc}(gf_x) \text{comb}(hf_x)], \quad (3)$$

where $V(f_x, f_y) = \mathcal{F}[v(x, y)]$, and $v(x, y)$ is the input object function.

For a detailed analysis of the recording of the matched filters and the correlation operation refer to Refs. 4-6 and 11.

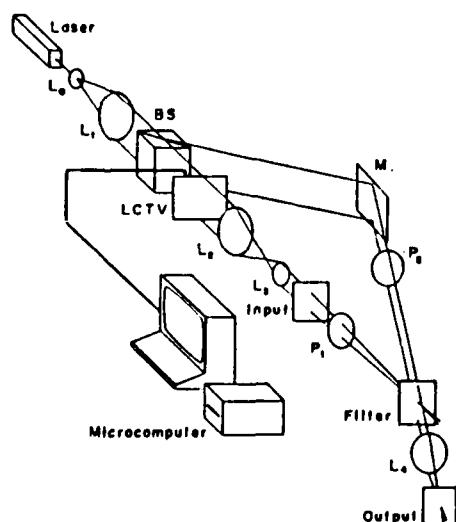


Fig. 1. Multichannel optical correlator using an addressable LCTV. L_0 and L_1 , collimating system; L_2 and L_4 , transform lenses; L_3 , magnifying lens; P_1 and P_2 , polarizers; BS, beam splitter; M, mirror.



Fig. 2. Experimental results: the recorded multiple matched filter (on one plate).

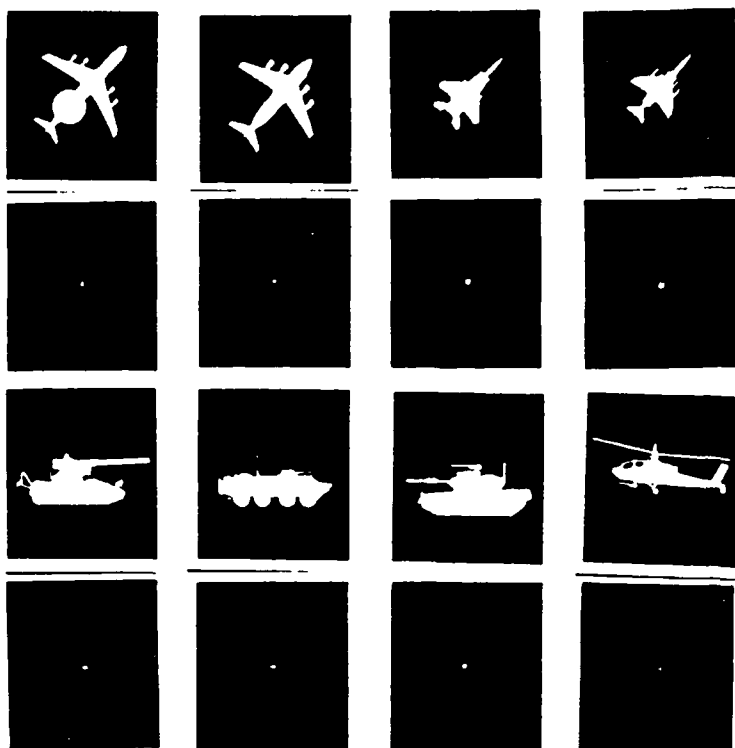


Fig. 3. Experimental results: autocorrelation peaks of eight input objects.

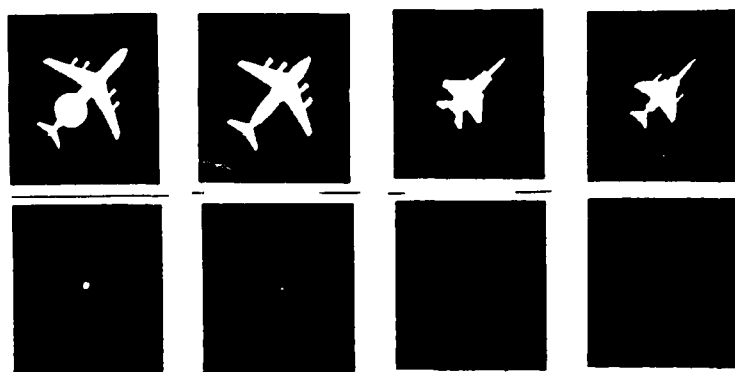


Fig. 4. Experimental results: autocorrelation and cross-correlation peaks obtained with the filter for warning plane.

We set adjustable delays between the subroutines, longer delays (minutes) for filter construction, and shorter delays (seconds) for target detection. To multiplex the matched filters onto a recording plate, we change the orientation and period of the grating via the microcomputer. During the detection, the orientation and period of the grating are automatically changed once again. As soon as the autocorrelation peak appears at the output plane, which means the input image has been recognized, the scanning is terminated; otherwise it is continued.

As an experimental demonstration, multichannel spatial filters of eight input objects were recorded on a holographic plate, as shown in Fig. 2. The output peaks related to the input objects are shown in Figs. 3 and 4. From these results, we see that a multichannel correlating operation can be achieved by using a programmable LCTV grating.

A programmable scanning correlator using a low-cost LCTV has been implemented. This technique alleviates the positioning problem of the mechanically scanning method.

The scanning speed of the proposed correlator is primarily limited by the microcomputer and the response time of the LCTV. Furthermore, if a higher-resolution LCTV is available, both the input object and modulating grating can be superimposed onto the LCTV screen. Thus a programmable real-time electrically addressed correlator may be realized.

We acknowledge the support by U.S. Air Force, Rome Air Development Center, Hanscom Air Force Base, MA, under contract F19628-87-C-0086.

References

1. A. VanderLugt, "Signal Detection by Complex Spatial Filtering," *IEEE Trans. Inf. Theory* IT-10, 139 (1964).
2. K. G. Leib, R. A. Bondurant, and M. R. Wohlert, "Optical Matched Filter Correlator Memory Techniques and Storage Capacity," *Opt. Eng.* 19, 414 (1980).

3. H. K. Liu and J. G. Duthie, "Real-Time Screen-Aided Multiple-Image Optical Holographic Matched-Filter Correlator," *Appl. Opt.* **21**, 3278 (1982).
4. F. T. S. Yu and X. J. Lu, "Real-Time Scanning Correlator," *Appl. Opt.* **23**, 3109 (1984).
5. F. T. S. Yu and Q. H. Zhou, "A Multichannel Optical Correlator," *Opt. Commun.* **64**, 111 (1987).
6. Q. H. Zhou and X. J. Lu, "Diffraction by a 3-D Oriented Grating and its Use in Scanning Correlation Detection," *Appl. Opt.* **26**, 4803 (1987).
7. D. A. Gregory and L. L. Huckabee, "Acoustooptically Addressed Fourier Transform Matched Filtering," *Appl. Opt.* **24**, 859 (1985).
8. H. K. Liu, J. A. Davis, and R. A. Lilly, "Optical-Data-Processing Properties of a Liquid-Crystal Television Spatial Light Modulator," *Opt. Lett.* **10**, 635 (1985).
9. D. A. Gregory, "Real-Time Pattern Recognition Using a Modified Liquid Crystal Television in a Coherent Optical Correlator," *Appl. Opt.* **25**, 467 (1986).
10. F. T. S. Yu, S. Jutamulia, T. W. Lin, and D. A. Gregory, "Adaptive Real-Time Pattern Recognition Using a Liquid Crystal TV Based Joint Transform Correlator," *Appl. Opt.* **26**, 1370 (1987).
11. Chenhua Zhang, "Some Applications of Spatial Modulation to Optical Information Processing," *Acta Opt. Sinica* **2**, 406 (1982).

Integrated-optic Mach-Zehnder rf phase comparator

L. M. Walpita, S. C. Wang, and W. S. C. Chang

S. C. Wang is with Lockheed Palo Alto Research Laboratories, 3251 Hanover Street, Palo Alto, California 94505-1185; the other authors are with University of California at San Diego, Department of Electrical & Computer Engineering, La Jolla, California 92093.
Received 18 March 1988.

0003-6935/88/183772-02\$02.00/0.

© 1988 Optical Society of America.

In rf signal processing applications, the determination of the rf signal phase is sometimes required. For example, in radar direction finding, the signal direction can be obtained from the phase difference between detected rf signals from two spatially separated antennas. In such situations electronic signal processing of the received signals is employed to determine this phase difference; acoustic and acoustooptic techniques of rf signal phase evaluation have been discussed.^{1,2} However, systems employing these techniques are fairly limited in frequency response. These techniques have been employed to determine the phase angle to better than 0.3° at 25% bandwidth at operating frequencies below 1 GHz.³

We describe a novel high-frequency phase comparator based on a large signal modulation of light in an integrated optic Mach-Zehnder interferometer. In this device two high-frequency electrical signals are fed into the electrodes on the two channels of the Mach-Zehnder modulator. The phase difference of the two signals is measured by determining the optical intensity of the output of the modulator.

The schematic diagram of the phase comparator is shown in Fig. 1. The input light to the device is divided equally into two channels. The light wave in the reference arm of the output junction of the interferometer, modulated by the reference signal, is given by

$$R = A \cos(\omega_0 t + m_1 \sin(\omega_e t) + \beta_1 l_1),$$

where ω_0 is the optical frequency in radians per unit time, m_1 is the amplitude of the sinusoidal change of the phase of the

optical mode that is caused by the high-frequency reference, l_1 is the length of the reference arm, β_1 is the propagation constant, ω_e is the electrical reference frequency in radians per unit time, and t is the time. It is assumed that the amplitude A of the optical signals in both the channels are equal. The light wave in the signal arm at the output junction of the interferometer is given by

$$S = A \cos(\omega_0 t + m_2 \sin(\omega_e t + \Delta\phi) + \beta_2 l_2),$$

where l_2 is the signal arm length, β_2 is the propagation constant in the signal arm, m_2 is the amplitude of the sinusoidal change of the phase of the optical mode that is caused by the signal, and $\Delta\phi$ is the phase difference between the signal and reference voltage. The two optical waves from the two channels will interfere at the output junction of the Mach-Zehnder modulator, and the resulting amplitude corresponds to the sum of S and R given by $T = S + R$.

The dc component of the optical intensity as seen by a detector at the output is

$$\begin{aligned} T^2 = & 0.5 + \frac{J_0(m_1)J_0(m_2)}{2} \cos(\beta_2 l_2 - \beta_1 l_1) \\ & + J_1(m_1)J_1(m_2) \cos(\beta_2 l_2 - \beta_1 l_1 + \Delta\phi) \\ & + J_2(m_1)J_2(m_2) \cos(\beta_2 l_2 - \beta_1 l_1 + 2\Delta\phi) \\ & + J_3(m_1)J_3(m_2) \cos(\beta_2 l_2 - \beta_1 l_1 + 3\Delta\phi) \dots \end{aligned}$$

where J_n is the Bessel function of the order n (n is an integer). Large amplitudes of modulation cause large nonlinearities in the modulator output, and the effective number of Bessel terms in the expression are increased.

The Mach-Zehnder modulator channels were $\sim 3.5 \mu\text{m}$ wide and designed for single-mode operation at 0.6328 μm . The waveguides were fabricated on x-cut lithium niobate for y-propagation. To fabricate the waveguides, 235-Å thick titanium strips were diffused into the substrate for 3.5 h at 1000°C. Aluminum electrodes of 3.8-mm length, 4- μm gap, and 6- μm width were deposited onto the substrate with the gap centered on the channels.

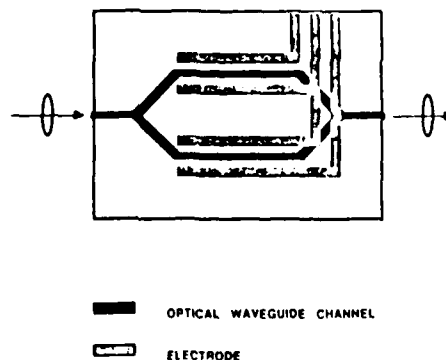


Fig. 1. Schematic of the Mach-Zehnder modulator. It consists of titanium-diffused waveguides in x-cut lithium niobate for y-propagation with aluminum electrodes deposited on both waveguide arms.

HARD-CLIPPING JOINT TRANSFORM CORRELATOR USING A MICROCHANNEL SPATIAL LIGHT MODULATOR

F. T. S. Yu and Q. W. Song
Electrical Engineering Department
The Pennsylvania State University
University Park, Pennsylvania 16802

Y. Suzuki
Hamamatsu Photonics KK
Hamamatsu City
Japan

M. Wu
Hamamatsu Corporation
Bridgewater, New Jersey 08807

KEY TERMS

Optical processing, optical correlation, optical computing, spatial light modulator

ABSTRACT

A programmable real time optical joint transform correlator that generates sharper autocorrelation peaks is presented. A microchannel spatial light modulator is utilized as the threshold hard clipping square law device. A liquid crystal television is used to display the input target and reference image. The basic principle of the system and a preliminary experimental result are given.

I. INTRODUCTION

Because of its high processing speed and structural simplicity, an optical joint transform correlator has been proposed for the application to pattern recognition. With advancing technology, various schemes to perform real-time joint transform correlation have been reported [1, 2]. Nevertheless, all the existing techniques have a common drawback, namely, that the correlation peak intensity is only a very small fraction of the illumination intensity. This low intensity presents no major problem if input signal-to-noise ratio (SNR) is high. Whenever the SNR is low, however, the detection of the signal becomes increasingly more difficult. Using a phase-only matched filter [3] can improve the diffraction efficiency of the correlation peak many fold. Nevertheless, a phase only filter is difficult to realize in practice with the current state-of-the-art electrooptic devices.

In this article, we will introduce a real-time programmable joint transform correlator utilizing the threshold hard-clipping property of a microchannel spatial light modulator (MSLM) [4]. We will show that this technique is capable of producing sharper autocorrelation peaks than the conventional optical correlator. By combining the advantages of the state-of-the-art electrooptic devices and flexibility of a microcomputer, the system can be built as an adaptive, self-learning correlator. The operating principle of the technique and a preliminary experimental demonstration are given.

II. BACKGROUND

A. Microchannel Spatial Light Modulator The MSLM is a reflective type electrooptic spatial light modulator. It consists of a photocathode, imaging electrodes, a microchannel plate (MCP), a mesh electrode, and an electrooptical (EO) crystal plate positioned in a sealed vacuum tube. In operation, the write-in image projected on the photocathode creates a spatial

photoelectron distribution. The electrostatic lens images the distribution onto the MCP. After a 10^3 to 10^4 electron multiplication by the MCP, the electrical charge image is deposited on the inner side of the EO crystal plate. This charge distribution induces a spatially varying electric field within the crystal plate. The field in turn modulates the phase retardation between the X and Y components of the read-out light that makes a double pass through the plate. Passing the light through an analyzer, a coherent optical image corresponding to the input image is obtained. One unique feature of the MSLM is that when the bias voltages are properly controlled, the device can perform quite a number of optical operations in its internal mode processing.

B. Joint Transform Correlator. The principle of the classical joint transform correlator (JTC) is well documented by Weaver and Goodman [5]. To compare it with the proposed MSLM based system, we shall briefly discuss its operation in a specific example. For simplicity, we suppose both the target and the reference image at the input plane are binary type with square apertures of width w . The main separation between them is l . The amplitude transmittance function of these input objects can be expressed as

$$f(x, y) = \left[\text{rect}\left(\frac{x - l/2}{w}\right) + \text{rect}\left(\frac{x + l/2}{w}\right) \right] \text{rect}\left(\frac{y}{w}\right) \quad (1)$$

where the rectangular function is defined as

$$\text{rect}\left(\frac{x}{w}\right) = \begin{cases} 1, & \text{if } |x| \leq \frac{w}{2} \\ 0, & \text{otherwise} \end{cases}$$

If the input objects are illuminated by a collimated coherent light, the complex light field at the back focal plane of a transform lens would be

$$F(\nu, \mu) = c \frac{\sin(\pi w \nu)}{\pi \nu} \frac{\sin(\pi w \mu)}{\pi \mu} \cos(\pi l \nu) \quad (2)$$

where c is a proportionality constant and μ and ν are spatial frequency coordinates, corresponding to the X and Y directions, respectively. If this complex light field is imaged onto a square-law convertor (e.g., a photographic plate), then the recorded amplitude transmittance can be written as

$$t = t_0 - \beta |\Delta F|^2 \quad (3)$$

where t_0 and β are the bias transmittance and the slope of the T-E (transmittance vs. exposure) curve, respectively.

In linear approximation, we would use a linear piecewise model to represent the T-E curve. Thus, Eq. (3) can be approximated by

$$t = 1 - \alpha \left[\frac{\sin(\pi w \nu)}{\pi \nu} \frac{\sin(\pi w \mu)}{\pi \mu} \cos(\pi l \nu) \right]^2 \quad (4)$$

where α is a proportionality constant. Since $t \geq 0$, the maximum value of α is $\alpha_{\max} = 1/w^4$.

Taking the inverse Fourier transform of the preceding equation, the autocorrelation functions distributed at the out-

put plane would be

$$g(x, y) = -A \frac{1}{4w^2} \left[\Lambda\left(\frac{x-l}{w}\right) + \Lambda\left(\frac{x+l}{w}\right) \right] \Lambda\left(\frac{y}{w}\right) \quad (5)$$

where A is the illumination amplitude, and Λ represents a triangular function defined as

$$\Lambda\left(\frac{x}{w}\right) = \begin{cases} 1 - \frac{|x|}{w} & \text{if } |x| \leq w \\ 0 & \text{otherwise} \end{cases}$$

In view of Eq. (5), the intensity of the correlation peaks is about $A^2/16w^4$. Moreover, the illustrated technique is not a real-time technique. In the following discussion we shall, however, describe a programmable hard-clipping JTC using a MSLM.

III. BASIC PRINCIPLE

The schematic diagram of a microcomputer-based JTC is shown in Figure 1. The liquid crystal plate of a LCTV is used to display a real-time target and a reference image at the input plane of an optical processor. The working principle of the LCTV as an optical element is well known. The major advantage of using a LCTV must be programmability, which can be addressed with a microcomputer, for the generation of various reference images. The telescopic imaging lenses are employed to demagnify the input object images from the LCTV to an appropriate size and then transformed onto the MSLM. We shall use the MSLM as a threshold hard-clipping device. The output light field is detected by a CCD camera. This detected electrical signal can be sent to a TV monitor for observation or fed back to the microcomputer for further instruction. Thus, in principle, an adaptive hybrid electrooptic correlator could be constructed.

Let us assume that the target and reference image are the same as expressed by Eq. (1). The light intensity distribution at the input end of the MSLM would be

$$|F(\nu, \mu)|^2 = c^2 \left[\frac{\sin(\pi w \nu)}{\pi \nu} \frac{\sin(\pi w \mu)}{\pi \mu} \cos(\pi l \nu) \right]^2 \quad (6)$$

Notice that the grid structure of the LCTV, which is beyond the resolution limit of the MSLM, is omitted. To obtain a binarized power spectral distribution for joint transform correlation, the bias voltages of the MSLM are adjusted such that only those parts of the input with intensity values above the threshold level will be responded. This hard-clipping property of the MSLM converts the input irradiance $I(\nu, \mu)$ into a series of binary phase distributions, between the X and Y components of the read-out light, as depicted in Figure 2. By binarizing the central lobe of Eq. (6) using the half-power criterion, the output phase function can be obtained with the first-order approximation, as given by

$$\Gamma = \pi \text{rect}\left(\frac{\nu}{1/w}\right) \text{rect}\left(\frac{\mu}{1/w}\right) \sum_{-\infty}^{\infty} \text{rect}\left(\frac{\nu}{4l}\right) \otimes \delta\left(\nu - \frac{n}{l}\right) \quad (7)$$

where \otimes denotes the convolution operation. This equation represents a truncated binary phase grating. After emerging from the polarizing beam splitter (PBS), the complex light

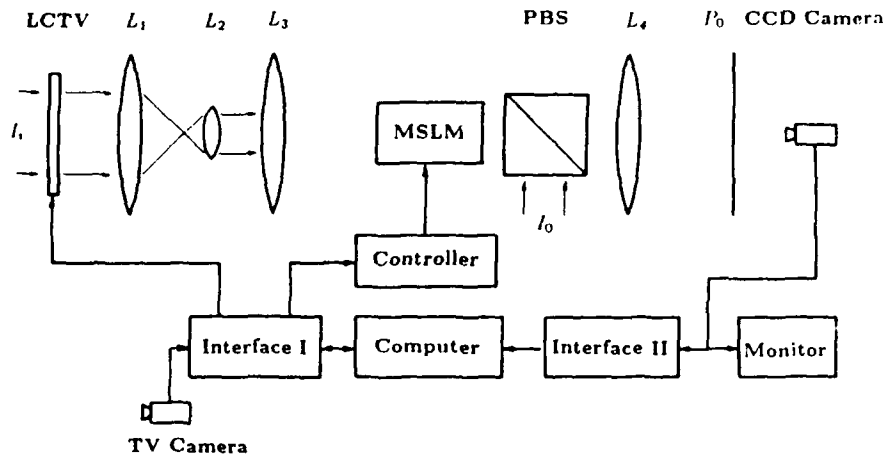


Figure 1 The schematic of a programmable optical joint transform correlator: I_i , coherent input illumination; L_1 - L_4 , lenses; PBS, polarizing beam splitter; I_0 , He-Ne laser read-out illumination; P_0 , output plane

field becomes

$$E_0 = \frac{A}{2} (e^{i\Gamma} - 1) \quad (8)$$

where A is the amplitude of the read-out light.

Using straightforward manipulation to inverse transform Eq. (8), the output autocorrelation functions can be shown as

$$E = \frac{A}{\pi} \left\{ \frac{\sin[\pi(x-l)/w]}{\pi(x-l)} + \frac{\sin[\pi(x+l)/w]}{\pi(x+l)} \right\} \times \frac{\sin(\pi y/w)}{\pi y} \quad (9)$$

To compare the performance of the binarized JTC with the conventional JTC, we see that the correlation peak intensity of the proposed system is about $A^2/\pi^2 w^4$, whereas for the conventional JTC the correlation peak intensity would be $A^2/16w^4$. In other words, the correlation peak intensity of the proposed system would be about 1.62 times higher than that of the conventional one, under the same illumination. Moreover, if the bias voltages can be controlled such that the threshold hard clipping takes place at a lower intensity level to

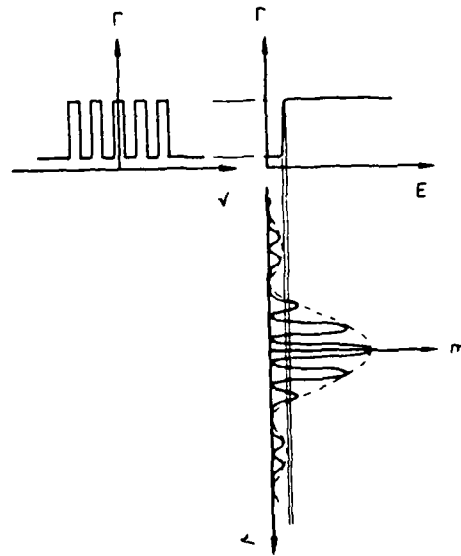


Figure 2 The conversion of the input light intensity to the output phase retardation for an MSLM in threshold hard-clipping mode

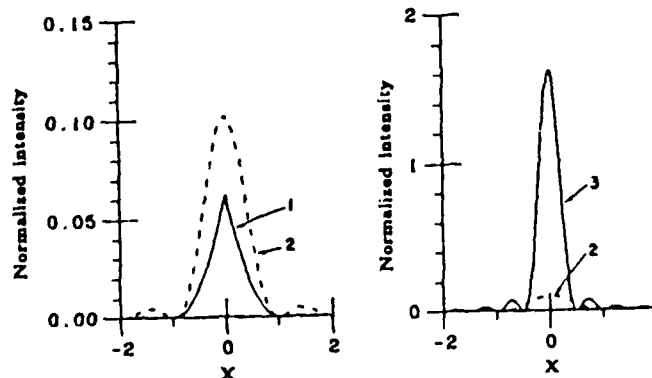


Figure 3 Simulated correlation peaks (normalized by A^2) for a 1×1 -mm binary input pattern: 1, correlation peak by the classical JTC; 2, by the proposed technique with threshold hard clipping applied to the central half of the main lobe of Eq. (6); 3, with threshold hard clipping including the whole main lobe of Eq. (6)

MICROWAVE PHOTOCONDUCTORS

V. P. McGinn
University of Tulsa
10714 E 20th Street
Tulsa, Oklahoma 74128

D. M. Grimes
Electrical Engineering Department
The Pennsylvania State University
University Park, Pennsylvania 16802

KEY TERMS

Lumped element, monolithic, microwave, photoconductor, cadmium selenide

ABSTRACT

An optically controlled microwave attenuator is described. The bulk semiconductor properties of cadmium selenide are demonstrated effectively at Ku band frequencies. The device is configured monolithically with a low capacitance resistive channel. Electrical resonance is achieved with symmetric inductance loops which bridge the channel ends.

I. INTRODUCTION

There exist numerous situations which require control of microwave signals. Electronically variable attenuators are available for frequencies up to 20.0 GHz. These attenuators may take the form of PIN diodes or field effect transistors (FETs). At higher frequencies junction capacitance limits device usefulness. A more serious concern deals with decoupling the control signal from the RF signal path. The utility of a variable resistor under the control of incident optical illumination is obvious. Cadmium sulfide photoconductive cells have been employed in a wide variety of industrial applications for more than 40 years. In fact, the characteristic distributed resistance of these devices may result in large chip areas with the power handling capability up to several watts. Commercial photoconductive cells typically employ a serpentine resistance

TABLE 1 Comparison of CPU Time between the FFT Summation Scheme and the Conventional Brute-Force Summation on the Cray X-MP / 48 for a Free-Standing Frequency Selective Surface

No. of Unknowns	CPU (sec)	
	FFT Summation	Brute-Force Summation
24	0.127	0.449
60	0.165	1.135
112	0.267	2.286

TABLE 2 Comparison of CPU Time between the FFT Summation Scheme and the Conventional Brute-Force Summation on the Cray X-MP / 48 for Signals over a Periodically Perforated Ground Plane

No. of Unknowns	CPU (sec) for 7 iterations	
	FFT Summation	Brute-Force Summation
148	3.843	20.673

CONCLUSIONS

A numerically efficient summation technique using the FFT for the method of moments solution to electromagnetic problems associated with planar periodic structures is presented. Numerical results for the scattering problem from a frequency selective surface and the transmission problem from signal lines over a periodic perforated ground plane are presented to demonstrate the superior numerical efficiency of the present technique over the conventional brute-force summation scheme. This technique is especially well suited for the eigenvalue problems associated with planar periodic structures.

REFERENCES

1. B. J. Rubin and H. L. Bertoni, "Reflection from a Periodically Perforated Plane Using a Subsectional Current Approximation," *IEEE Trans. Antennas Propagat.*, Vol. AP-31, no. 11, Nov. 1983, pp. 829-836.
2. B. J. Rubin and H. L. Bertoni, "Waves Guided by Conductive Strips Above Periodically Perforated Ground Plane," *IEEE Trans. Microwave Theory Tech.*, Vol. MTT-31, no. 7, July 1983, pp. 541-549.
3. C. H. Chan and R. Mittra, "The Propagation Characteristics of Signal Lines Embedded in a Multilayered Structure in the Presence of a Periodically Perforated Ground Plane," *IEEE Trans. Microwave Theory Tech.*, Vol. MTT-36, no. 6, June 1988, pp. 968-975.
4. C. H. Chan, "Investigation of Iterative and Spectral Galerkin Techniques for Solving Electromagnetic Boundary Value Problems," Ph.D. Dissertation, Univ. of Illinois, Urbana, 1987.

Received 9-9-88

Microwave and Optical Technology Letters, 1/10, 372-374
 © 1988 John Wiley & Sons, Inc.
 CCC 0895-2477/88/\$4.00

JOINT FOURIER TRANSFORM PROCESSOR

F. T. S. Yu
 Department of Electrical Engineering
 The Pennsylvania State University
 University Park, Pennsylvania 16802

J. E. Ludman
 Optical Signal Processing Section
 Rome Air Development Center
 Hanscom Air Force Base, Massachusetts 01731

KEY TERMS

Joint transform processor, optical signal processor, optical correlator

ABSTRACT

A joint Fourier transform processor can be used as a conventional coherent optical processor. In principle, the joint transform processor can perform all the optical data processing that a conventional coherent optical processor can offer. Sample illustrations for signal extraction and image subtraction are given. The major advantages of the joint transform processor must be (1) the avoidance of synthesizing a matched spatial filter, (2) higher space-bandwidth product, (3) lower spatial carrier frequency requirement, (4) higher output diffraction efficiency, etc.

In a conventional coherent optical signal processor [1], the processing operation is usually carried out at the spatial frequency or Fourier plane with a complex spatial filter [2]. This type of coherent optical processor offers a myriad of complicated processing operations [3]. Its success is primarily due to the profound diffraction phenomena. We shall, in this letter, point out that complex signal processing can also be achieved by the spatial impulse response using a joint transform processor [4-6]. There are several inherent advantages of using the joint Fourier transform processor as compared with the conventional coherent processor: (1) spatial filter adjustment is not imposed; (2) a higher input space-bandwidth product; (3) generally, a higher modulation index of the joint transform hologram; (4) lower spatial carrier frequency, etc. In view of these advantages, a joint transform processor, in principle, is capable of performing optical signal processing more efficiently, particularly in the application to real-time signal processing [6].

Let us now consider a joint Fourier transform optical signal processor as depicted in Figure 1. We assume an object function $f(x, y)$ is inserted at $(\alpha_0, 0)$ and a spatial impulse response $h(x, y)$ is placed invertedly at $(-\alpha_1, 0)$ in the input plane P_1 . By illuminating the input objects with coherent light, the complex light distribution at the Fourier plane P_2 is given by

$$U(p, q) = F(p, q)e^{i\alpha_0 p} + H^*(p, q)e^{-i\alpha_1 p} \quad (1)$$

where (p, q) represents the angular spatial frequency coordinate system, the superscript asterisk represents the complex conjugate, and

$$F(p, q) = \mathcal{F}[f(x, y)]$$

$$H(p, q) = \mathcal{F}[h(x, y)]$$

where \mathcal{F} denotes the Fourier transformation. Thus, at the output end of the square law detector, the intensity distribution is given by

$$\begin{aligned} I(p, q) &= |U(p, q)|^2 \\ &= |F(p, q)|^2 + |H(p, q)|^2 \\ &\quad + F(p, q)H(p, q)e^{i2\alpha_0 p} \\ &\quad + F^*(p, q)H^*(p, q)e^{-i2\alpha_1 p} \end{aligned} \quad (2)$$

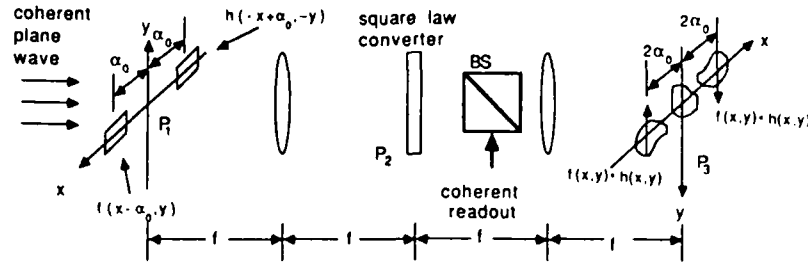


Figure 1 A joint Fourier transform processor. BS, beam splitter

By coherent readout of this intensity distribution, the complex light distribution at the output plane P_2 would be

$$g(x, y) = f(x, y) \odot f(x, y) + h(-x, -y) \odot h(-x, y) + f(x, y) * h(x + 2\alpha_0, y) + f(-x, -y) * h(-x - 2\alpha_0, -y) \quad (3)$$

where \odot denotes the correlation operation and $*$ denotes the convolution operation. Thus, we see that two sets of convolution operations, i.e., the object function $f(x, y)$ convolves with the spatial impulse response $h(x, y)$, are diffracted around $(-2\alpha_0, 0)$ and $(2\alpha_0, 0)$, respectively.

Similarly, if the spatial impulse response $h(x, y)$ is properly placed (i.e., not inverted) at the input plane, e.g., $h(x + \alpha_0, y)$, the output light distribution can be shown as

$$g(x, y) = f(x, y) \odot f(x, y) + h(x, y) \odot h(x, y) + f(x, y) \odot h(x + 2\alpha_0, y) + f(-x, -y) \odot h(-x - 2\alpha_0, -y) \quad (4)$$

where \odot denotes the correlation operation. From Equations (3) and (4) we notice that the joint Fourier transform system can be used as a coherent optical data processor. In principle, it can perform all the optical data processing that a conventional coherent optical processor can offer.

We shall illustrate an application to extraction of a signal embedded in a random noise. We assume that a target is embedded in an additive white Gaussian noise, as given by

$$f(x - \alpha_0, y) = s(x - \alpha_0, y) + n(x - \alpha_0, y) \quad (5)$$

where $s(x, y)$ represents the target function and $n(x, y)$ is the noise distribution. If the spatial impulse response is given by

$$h(x + \alpha_0, y) = s(x + \alpha_0, y) \quad (6)$$

then from Equation (4), the output complex light distribution can be shown, such as

$$g(x, y) = [s(x, y) + n(x, y)] \odot [s(x, y) + n(x, y)] + s(x, y) \odot s(x, y) + [s(x, y) + n(x, y)] \odot s(x + 2\alpha_0, y) + [s(-x, -y) + n(-x, -y)] \times \odot s(-x - 2\alpha_0, -y) \quad (7)$$

where \odot denotes the correlation operation.

Since $n(x, y)$ is an additive white Gaussian noise, we note that [7]

$$n(x, y) \odot s(x, y) = 0 \quad (8)$$

Thus Equation (8) reduces to

$$g(x, y) = 2s(x, y) \odot s(x, y) + n(x, y) \odot n(x, y) + s(x, y) \odot s(x + 2\alpha_0, y) + s(-x, -y) \odot s(-x - 2\alpha_0, -y) \quad (9)$$

From this result, we see that two autocorrelation functions of the target object will be diffracted in the output plane around $(-2\alpha_0, 0)$ and $(2\alpha_0, 0)$, respectively. For experimental demonstration, a computer simulated object of this application is shown in Figure 2. From Figure 2(b), we see that two highly visible correlation peaks are obtained in the output plane. One of the apparent advantages of the joint transform correlation must be the avoidance of the matched filter synthesis. This technique is very suitable for application to the real-time pattern recognition.

Let us now illustrate a second application to image subtraction. We assume that the objects at the input plane are given by

$$f_1(x - \alpha_0, y) + \delta(x, y) + f_2(-x + \alpha_0, -y) \exp(i\pi) \quad (10)$$

where $\delta(x, y)$ is a delta function, $\exp(i\pi)$ represents a half-wave phase plate, and $f_1(x, y)$ and $f_2(x, y)$ are real objects.

The intensity distribution at the output end of the square law detector can be shown as

$$I(p, q) = 1 + |F_1(p, q)|^2 + |F_2^*(p, q)|^2 + [F_1^*(p, q) - F_2^*(p, q)] e^{i\alpha_0 p} + [F_1(p, q) - F_2(p, q)] e^{-i\alpha_0 p} - F_1(p, q) F_2^*(p, q) e^{-i2\alpha_0 p} - F_1^*(p, q) F_2(p, q) e^{i2\alpha_0 p} \quad (11)$$

where the superscript asterisk denotes the complex conjugate.

By coherent readout of Equation (11), the output complex light field would be

$$g(x, y) = \delta(x, y) + f_1(x, y) \odot f_1(x, y) + f_2(-x, -y) \odot f_2(-x, -y) + [f_1(-x + \alpha_0, -y) - f_2(-x + \alpha_0, -y)] + [f_1(x - \alpha_0, y) - f_2(x - \alpha_0, y)] - f_1(x, y) * f_2(x - 2\alpha_0, y) - f_1(-x, -y) * f_2(-x + 2\alpha_0, -y) \quad (12)$$

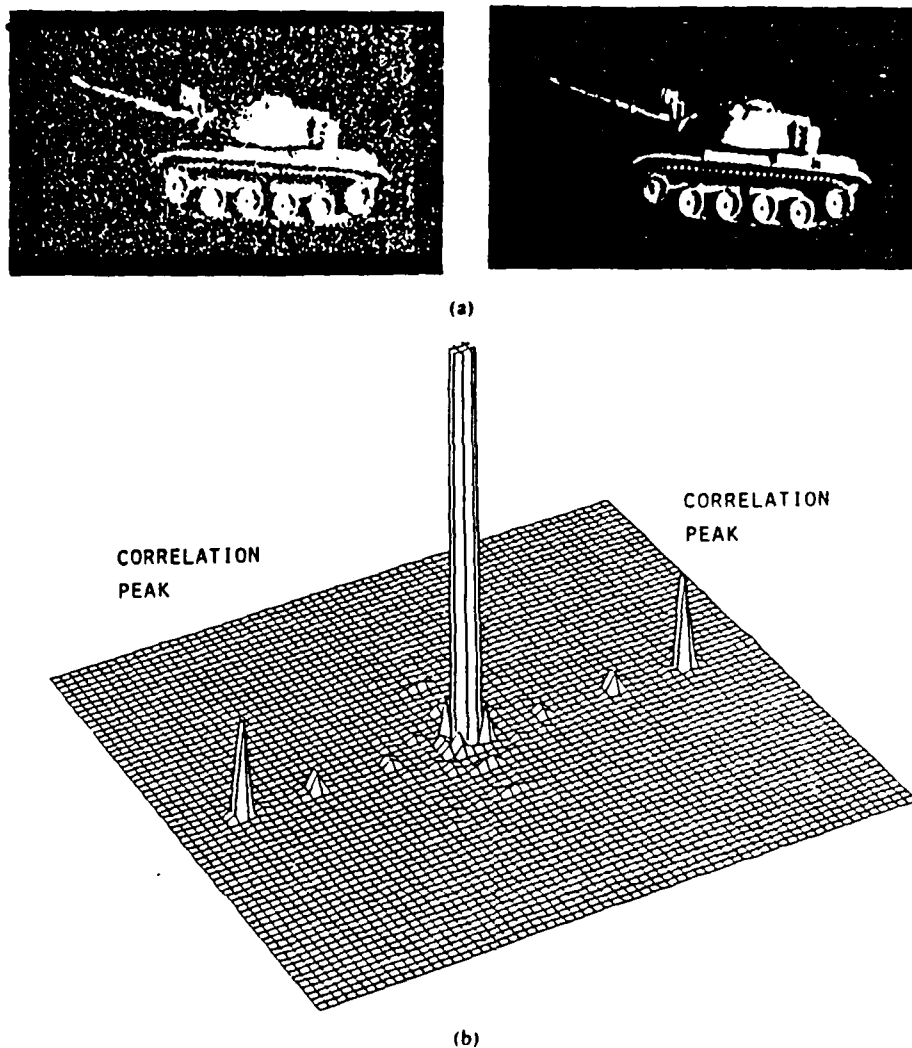


Figure 2 Extraction of a signal from random noise. (a) Left side—target imbedded in random noise. Right side—spatial impulse response of the target. (b) Output intensity distributions

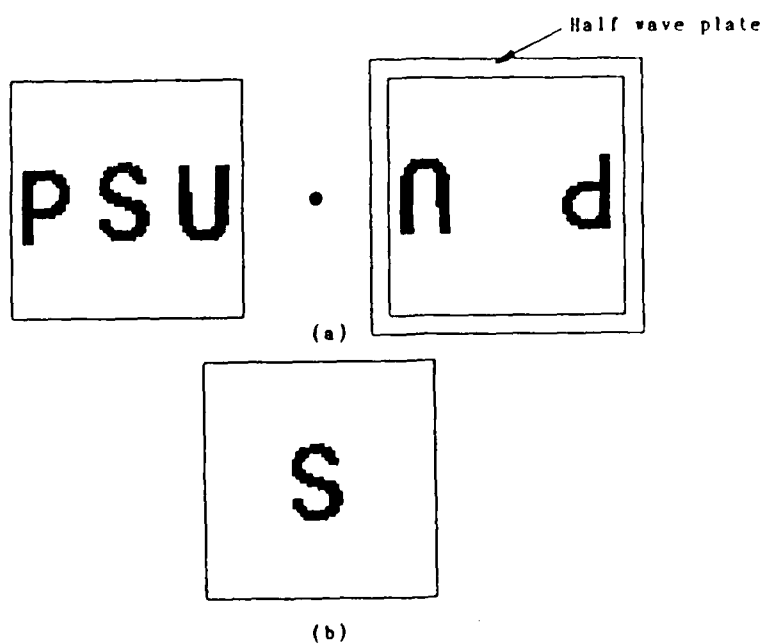


Figure 3 Image subtraction (a) Input objects (b) Subtracted image

where \odot and \cdot denote the correlation and the convolution operations, respectively. In view of Equation (12), we see that two sets of subtracted images will be diffracted around $(-a_0, 0)$ and $(a_0, 0)$, respectively. A computer simulation of this application is shown in Figure 3, where Figures 3(a) are the input objects and Figure 3(c) shows the corresponding subtracted image obtained by this technique.

In conclusion, we would stress that, in principle, the joint transform processor can perform all the processing that a conventional coherent optical processor can offer. The inherent advantages of the joint transform processor are (1) the avoidance of complex spatial filter synthesis, (2) a higher input space-bandwidth product, (3) lower spatial carrier frequency requirement, (4) generally higher output diffraction efficiency, and many others.

ACKNOWLEDGMENT

We acknowledge the support of the U.S. Air Force Rome Air Development Center, Hanscom Air Force Base, under contract No. F19628-87-C-0086.

REFERENCES

1. L. J. Cutrona, E. N. Leith, C. J. Palermo, and L. J. Porcello, "Optical Data Processing and Filtering Systems," *IRE Trans. Inform. Theory*, Vol. IT-6, 1960, p. 386.
2. A. Vander Lugt, "Signal Detection by Complex Spatial Filtering," *IEEE Trans. Inform. Theory*, Vol. IT-10, 1964, p. 139.
3. F. T. S. Yu, *Optical Information Processing*, Wiley-Interscience, New York, 1983.
4. C. S. Weaver and J. W. Goodman, "A Technique for Optically Convolving Two Functions," *Appl. Opt.*, Vol. 5, 1966, p. 1248.
5. F. T. S. Yu and X. J. Lu, "A Real-Time Programmable Joint Transform Correlator," *Opt. Commun.*, Vol. 52, 1984, p. 47.
6. F. T. S. Yu and J. E. Ludman, "Microcomputer-Based Programmable Optical Correlator for Automatic Pattern Recognition and Identification," *Opt. Lett.*, Vol. 11, 1986, p. 395.
7. M. Schwartz, *Information, Transmission, Modulation, and Noise*, 2nd ed., McGraw-Hill, New York, 1970.

Received 9-19-88

Microwave and Optical Technology Letters, 1/10, 374-377
 © 1988 John Wiley & Sons, Inc.
 CCC 0895-2477/88/\$4.00

PENNSYLVANIA STATE UNIVERSITY, DEPARTMENT OF ELECTRICAL ENGINEERING,
University Park, Pa 16802

A TWO STEP, THREE COLOR, WHITE-LIGHT PSEUDOCOLOR ENCODING PROCESS

X. X. CHEN, A. W. MAYERS, F. T. S. YU

KEY WORDS :

White light

Pseudocolor encoding

MOIS CLÉS :

Lumière blanche

Codage en fausses couleurs

Un procédé de codage en fausses couleurs en deux étapes et à trois couleurs

SUMMARY : Pseudocolor encoding is a commonly used enhancement procedure for grey level images. One of the classical techniques for three color white light pseudocolor encoding was presented by Yu *et al.* [1]. In this paper a variation of this three color encoding method will be described that uses moiré fringe patterns from two encodings to carry the information previously obtained from the third encoding. Both a theoretical description and experimental results are presented.

RÉSUMÉ : Le codage en fausses couleurs est un procédé classique pour améliorer le rendu des niveaux de gris dans une image. L'une des techniques les plus connues pour le codage en trois couleurs en lumière blanche a été présentée par Yu *et al.* [1]. On décrit dans cet article une variante de ce procédé à trois couleurs qui utilise le réseau des franges de moiré de deux codages pour le troisième codage. Le principe et les résultats expérimentaux sont présentés.

I. — INTRODUCTION

Frequently, high resolution optical information is encoded through the use of grey level images. A common enhancement process used to aid in the analysis of these images is pseudocolor encoding. A number of methods to accomplish the encoding have been developed that use coherent [2], as well as incoherent white-light sources [3]. One of the first methods was proposed by Yu *et al.* [1]. The process described in Yu's paper uses three sequential spatial encodings of the positive, negative, and the product of the positive and negative images. A white-light source was used and the three components were processed using red, blue, and green filters to produce the output image. A shortened variation of this procedure will be described in this paper in which the three components are achieved using only two spatial encodings.

II. — DISCUSSION

The image shown in figure 1a will be used to help illustrate the process. The image is composed of three distinct grey levels: white, grey, and black. The figure 1a image was contact printed to obtain

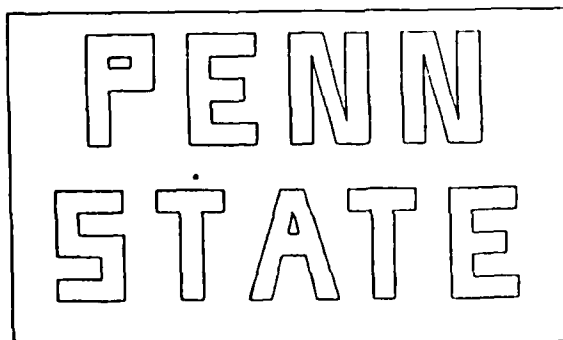


FIG. 1a. — Sample object to be encoded

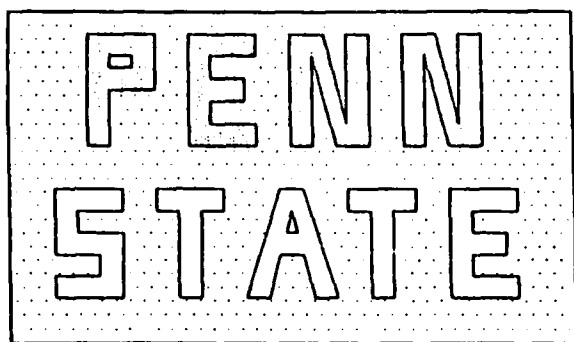


FIG. 1b. — Negative of sample object.

the negative image shown in figure 1b. To facilitate the encoding procedure, pin registration was used during the contact printing operation. Next, the positive image was encoded using a sampling grating oriented as shown in figure 2a. The negative was

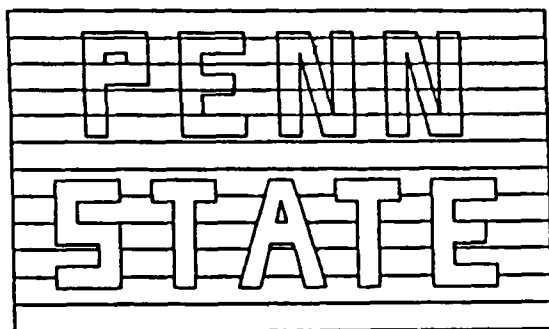


FIG. 2a. — Encoding of positive image.

then encoded with the sampling grating rotated by an angle θ with respect to the previous encoding, as shown in figure 2b. The cumulative result of the two encodings is shown in figure 2c. Note the moiré pattern that is formed in the grey areas.

The intensity transmittance of the encoded image can be written as

$$(x, y) = K \{ T_1(x, y) [1 + \operatorname{sgn}(\cos px)] + T_2(x, y) [1 + \operatorname{sgn}(\cos p(x \cos \theta + y \sin \theta))] \}^{-1}, \quad (1)$$

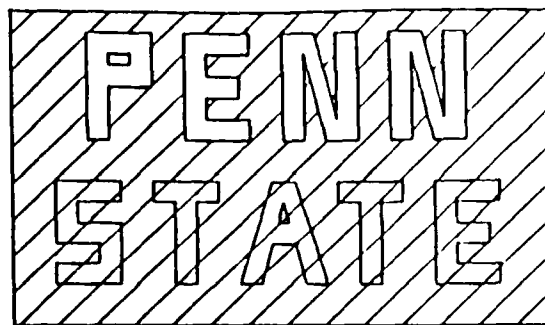


FIG. 2b. — Encoding of negative image.

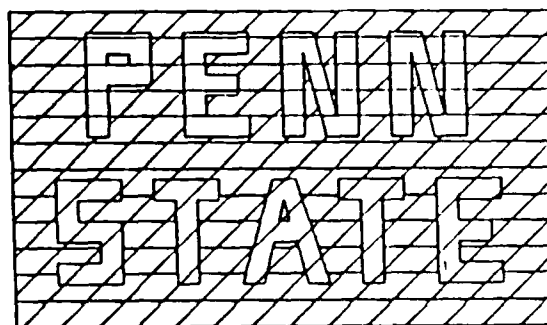


FIG. 2c. — Result of two encodings, note moiré pattern.

where K is a proportionality constant, T_1 and T_2 are the positive and negative image exposures, p is the spatial encoding frequency, γ is the film gamma, and

$$\operatorname{sgn}(\cos x) = \begin{cases} 1, & \cos x \geq 0 \\ -1, & \cos x < 0 \end{cases} \quad (2)$$

The resulting transparency is then bleached to obtain a surface relief phase object. Assuming that this encoding is within the linear region of the diffraction efficiency versus log-exposure curve, the amplitude transmittance can be written as

$$t(x, y) = \exp[i\phi(x, y)], \quad (3)$$

where $\phi(x, y)$ represents the phase delay distribution which is proportional to $T(x, y)$, the exposure of the encoded film.

Placing the bleached transparency at the input of a white-light processing system, the complex light field at the Fourier transform plane can be determined by evaluating the integral

$$\begin{aligned} S(\alpha, \beta; \lambda) &= \iint t(x, y) \exp\left[-i \frac{2\pi}{\lambda f} (\alpha x, \beta y)\right] dx dy \\ &= \iint \exp[i\phi(x, y)] \exp\left[-i \frac{2\pi}{\lambda f} (\alpha x, \beta y)\right] dx dy. \end{aligned} \quad (4)$$

The transmittance function $\exp[i\phi(x, y)]$ can be expanded to obtain

$$S(\alpha, \beta; \lambda) = \iint \left\{ 1 + i\phi(x, y) + \frac{1}{2} [i\phi(x, y)]^2 + \dots \right\} \times \exp \left[-i \frac{2\pi}{\lambda f} (\alpha x, \beta y) \right] dx dy. \quad (5)$$

Substituting Eq. (3) into (5) and retaining the first order terms, the following expression results

$$S(\alpha, \beta; \lambda) = \hat{T}_1 \left\{ \alpha \pm \frac{\lambda f}{2\pi} p, \beta \right\} + \hat{T}_2 \left\{ \alpha \pm \frac{\lambda f}{2\pi} p \cos \theta, \beta + p \sin \theta \right\} + \hat{T}_1 \left\{ \alpha \pm \frac{\lambda f}{2\pi} p, \beta \right\} * \left[\hat{T}_2 \left\{ \alpha + \frac{\lambda f}{2\pi} p \cos \theta, \beta + \frac{\lambda f}{2\pi} p \sin \theta \right\} + \hat{T}_2 \left\{ \alpha - \frac{\lambda f}{2\pi} p \cos \theta, \beta - \frac{\lambda f}{2\pi} p \sin \theta \right\} \right], \quad (6)$$

where \hat{T}_1 and \hat{T}_2 are the Fourier transforms of T_1 and T_2 , * denotes the convolution operation. The proportionality constants have been neglected for simplicity. The convolution term can be written

$$\hat{T}_1(\alpha, \beta) * \hat{T}_2(\alpha, \beta) * \left[\delta \left\{ \alpha \pm \frac{\lambda f}{2\pi} p [1 + \cos \theta], \beta + \frac{\lambda f}{2\pi} p \sin \theta \right\} + \delta \left\{ \alpha \pm \frac{\lambda f}{2\pi} p [1 - \cos \theta], \beta - \frac{\lambda f}{2\pi} p \sin \theta \right\} \right], \quad (7)$$

which shows the locations of the moire spectra.

The moire pattern can be decomposed into a two dimensional signal that has fundamental periods in the directions shown in figure 3. This pattern is in

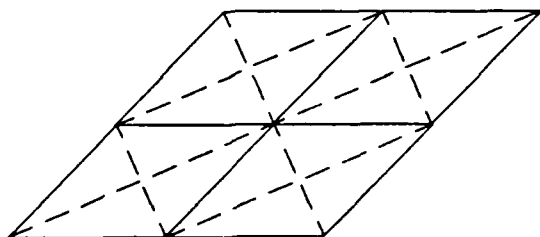


FIG. 3. — Dashed lines indicate orientation of fundamental periods for the moire pattern.

agreement with the convolution terms given in Eq. (6). Figure 4 shows the diffraction pattern formed by

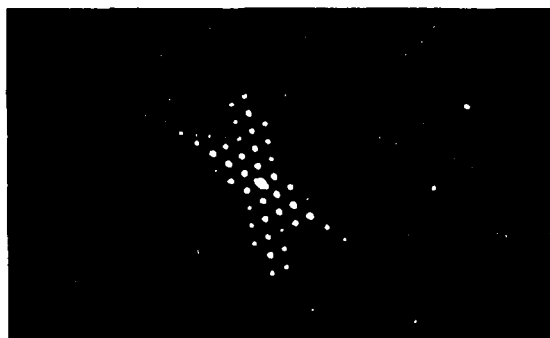


FIG. 4. — Image of diffraction pattern produced by encoded transparency.

the encoded transparency. If filters are placed in the Fourier plane as shown in figure 5, the image irradiance at the output plane becomes

$$I(x, y) = T_1^2(x, y) + T_2^2(x, y) + |T_1(x, y) T_2(x, y)|, \quad (8)$$

thus, the image irradiance expressed by Eq. (8) is the superposition of the positive, negative, and cross-product terms.

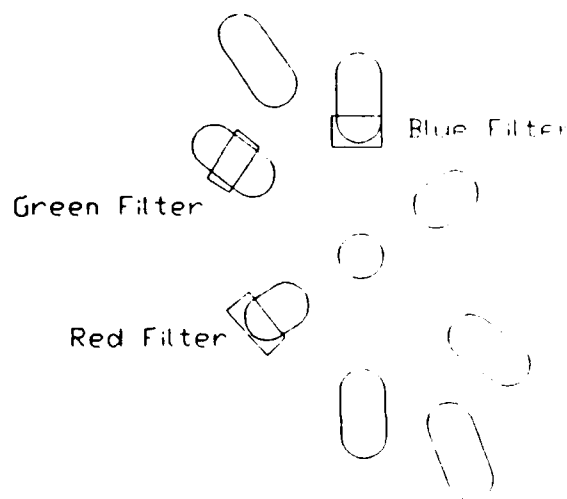


FIG. 5. — Location of filters in Fourier plane for reconstructed image.

III. — RESULTS AND CONCLUSIONS

An image of an aluminium fracture specimen obtained from a scanning electron microscope was used for this discussion. Positive and negative images were then encoded using a sampling grating having 40 lines/mm on Kodak 5460 microfilm. To balance the intensities between the primary and convolved spectra, neutral density filters were used along with the color filters for the positive and negative spectra.



FIG. 6a. — Original image.

As can be seen in figure 6b, the output of the pseudocolor encoded image represents a considerable improvement over the black and white image in that the fine detail structure of the image has been enhanced. Figure 6c shows the cross-product term produced by the moiré pattern. By using this new procedure, the pseudocolor encoding was accomplished using a single sampling grating, and two rather than three exposures. This allows greater use of the dynamic range of the film by eliminating one exposure. This method also illustrates an interesting application of moiré patterns.

We acknowledge the support of the U.S. Air Force, Rome Air Development Center, Hanscom AFB, Mass., under contract no. F19628-87-C-0086.



FIG. 6b. — Pseudocolored image.



FIG. 6c. — Cross-product of image recorded by moiré pattern.

REFERENCES

- [1] YU (F. T. S.), CHEN (X. X.), CHAO (I. H.). — "White-Light Pseudocolor Encoding with Three Primary Colors", *J. Opt.*, 15, 55 (1984).
- [2] ARRIBAS (S.), SANTAMERIA (J.), BESCOS (J.). — "Density Pseudocolor Encoding by Holographic Techniques with Three Primary Colors", *Opt. Eng.*, 23(1), 98 (1984).
- [3] SANTAMERIA (J.), PLAZA (A.), BESCOS (J.). — "Colour Image Enhancement by White Light Spatial Filtering", *Opt. Com.*, 45(4), 244 (1983).

(Manuscript received in August 25, 1988.)

Holographic associative memory system using a thresholding microchannel spatial light modulator

Q. W. Song, MEMBER SPIE
Francis T. S. Yu, FELLOW SPIE
The Pennsylvania State University
Electrical Engineering Department
University Park, Pennsylvania 16802

Abstract. Experimental implementation of a holographic optical associative memory system using a thresholding microchannel spatial light modulator (MSLM) is presented. The first part of the system is basically a joint transform correlator, in which a liquid crystal light valve is used as a square-law converter for the inner product of the addressing and input memories. The MSLM is used as an active element to recall the associated data. If the device is properly thresholded, the system is capable of improving the quality of the output image.

Subject terms: optical signal processing; holographic associative memory; image processing; spatial light modulators; neural networks.

Optical Engineering 28(5): 533-536 (May 1989).

CONTENTS

1. Introduction
2. Principle
3. Experimental results
4. Concluding remarks
5. Acknowledgments
6. References

1. INTRODUCTION

It is well known that optical associative memory can also be defined as fault tolerant memory,¹ which can be addressed by a partial or distorted input object to recall the stored, and possibly noise-free, information. The technique has significant applications to optical pattern recognition and image processing.

The concept of optical associative memory can be traced back as early as the work published by Van Heerden² and later strengthened by the holographic associative memory of Gabor.³ Their techniques are often called the ghost image method. With the recent surging activities in neural networks (e.g., Refs. 4-6), several optical associative memory architectures have been developed.^{1,7-11} Different methods to perform the inner product operation for optical associative memory have been investigated. For instance, Paek and Psaltis demonstrated a method using a Vander Lugt correlator to implement the inner product of the input object and reference data.⁷ The stored data can then be addressed with the detected correlation peak by pinhole sampling. To improve the storage capacity, Owechko et al. used an angularly multiplexed Fourier hologram technique.¹ They used a phase conjugate mirror to address the Fourier hologram.

In this paper, we present a system using an active microchannel spatial light modulator (MSLM) to improve the readout process. With the hard clipping property of the MSLM, and at the sacrifice of shift invariance, we were able to improve the quality and increase the intensity of the addressing beams so that high quality recalled data were obtained. Experimental results for binary objects are provided.

2. PRINCIPLE

The two-dimensional outer product associative memory can be expressed in the inner product form as⁷

$$h(x,y) = \sum_{m=1}^M \left[\int f_m(\xi,\eta) f(\xi,\eta) d\xi d\eta \right] h_m(x,y), \quad (1)$$

where $f(\xi,\eta)$ is the system input function, $h(x,y)$ is the corresponding system output, $f_m(\xi,\eta)$ is the m th reference memory, $h_m(x,y)$ is its associated output pattern, and M is the total number of stored memories.

Equation (1) shows that the overall process is composed of three steps, namely, inner product (the input object with reference data), multiplication (the inner product with the associated memory), and summation.

Our experimental setup to implement the above process is shown in Fig. 1. The first half of the system is a joint transform correlator with an addressing object and multiple reference data (input memories) at the input plane P_1 . The second half of the system has an active MSLM to improve the quality of the output addressed data. In operation, the addressing data and multiple reference functions are Fourier transformed by lens L_1 . The joint transform power spectrum is detected by the square-law converter liquid crystal light valve (LCLV). By inversely Fourier

Invited Paper IA-105 received Nov. 19, 1988; revised manuscript received Jan. 18, 1989; accepted for publication Feb. 15, 1989.
© 1989 Society of Photo-Optical Instrumentation Engineers.

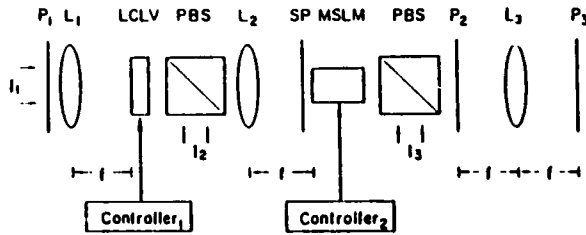


Fig. 1. Holographic associative memory system using an active MSLM. P₁—input plane; P₂—hologram plane; P₃—output plane; SP—sampling pinholes; PBS—polarizing beam splitter.

transforming the power spectrum with lens L₂, we obtain a group of correlation peaks. To eliminate all of the unwanted light, a set of sampling pinholes (SPs) is used. Only selected correlation peaks can be written onto the MSLM. If the addressing object is most similar to one of the stored memories (i.e., the reference functions), its correlation peak will be the strongest. Thus, the output of the MSLM can be considered as a spatially encoded array of light sources, with the strength of each source proportional to the correlation peak value. If we have an array of Fourier transform holograms inserted at P₂ in accordance with the association rule, a recalled image (addressed data) can be seen on the output plane P₃. The analytical description of the process is given in the following.

For simplicity, we assume that the addressing function and input memories are lined up along the *x* axis. The amplitude transmittance of the input plane is given by

$$t(x, y) = f(x - x_0, y) + \sum_{m=1}^M f_m(x + x_0 + mx_1, y), \quad (2)$$

where x_0 and x_1 are two constants and M is the number of input memories. The Fourier power spectrum at the input side of the LCLV can be written as

$$\begin{aligned} E(p, q) &= |F(p, q)|^2 + \sum_{m=1}^M F_m(p, q) F_m^*(p, q) \exp[-j(2x_0 + mx_1)p] \\ &+ \sum_{m=1}^M F_m^*(p, q) F_m(p, q) \exp[j(2x_0 + mx_1)p] \\ &+ \sum_{m=1}^M \sum_{n=1}^M F_m^*(p, q) F_n(p, q) \exp[j(m - n)x_1 p], \end{aligned} \quad (3)$$

where $F(p, q)$ and $F_m(p, q)$ are the Fourier transform of $f(x, y)$ and $f_m(x, y)$, respectively. Notice that the amplitude transmittance of the LCLV is proportional to the intensity distribution of its input end. Therefore, the light field distribution on the SP is the inverse Fourier transform of Eq. (3), i.e.,

$$\begin{aligned} i_2(x, y) &= c \left[f(x, y) \otimes f(x, y) + \sum_{m=1}^M f(x, y) \otimes f_m(x - 2x_0 - mx_1, y) \right. \\ &+ \sum_{m=1}^M f_m(x, y) \otimes f(x + 2x_0 + mx_1, y) \\ &\left. + \sum_{m=1}^M \sum_{n=1}^M f_m(x, y) \otimes f_n(x + (n - m)x_1, y) \right], \end{aligned} \quad (4)$$

where \otimes denotes the correlation operation and c is a proportionality constant.

Note that as long as the quantity $x_1 - Mx_1$ is larger than the distance between two adjacent correlation peaks, they can be detected. When the MSLM is adjusted in its thresholding mode, the input and output light intensities are related by¹²

$$I_r(x, y) = \begin{cases} AI_w(x, y), & \text{if } I_w(x, y) \geq I_T, \\ 0, & \text{otherwise,} \end{cases} \quad (5)$$

where $I_w(x, y)$ and $I_r(x, y)$ are the write-in and readout light intensities of the device, A is an arbitrary constant, and I_T is the intensity threshold value. Thus, only the correlation peak intensities exceeding the threshold value would be responded at the output end of the MSLM. By setting I_T at a reasonably low value and blocking out all but the second term in Eq. (4) with the SP, the readout light field of the MSLM can be explicitly expressed as

$$i_m = c_1 \sum_{m=1}^M \int f_m^*(x - 2x_0 - mx_1, y) f(x - 2x_0 - mx_1, y) dx dy, \quad (6)$$

where c_1 is a proportionality constant and the asterisk denotes complex conjugation.

To complete the operation, a spatially multiplexed Fourier transform hologram is inserted in P₂ plane, in which the sub-hologram takes the form

$$\begin{aligned} H_m(p, q) &= \hat{F} \left\{ h_m(x, y) \exp \left[-j \frac{2\pi}{\lambda f} x(2x_0 - mx_1) \right] \right\}, \\ m &= 1, 2, \dots, M, \end{aligned} \quad (7)$$

where λ is the wavelength of illumination, f is the focal length of the inverse Fourier transform lens L₃, and \hat{F} represents the Fourier transform operation. If the hologram is aligned in a position such that each H_m is exactly illuminated by the m th term of Eq. (6), then the light field at the output plane P₃ can be shown as

$$\begin{aligned} h'(x, y) &= c_1 \sum_{m=1}^M \left[\int f_m^*(\xi, \eta) f(\xi, \eta) d\xi d\eta \right] h_m(x, y) \\ &\times \exp \left[-j \frac{2\pi}{\lambda f} x(2x_0 - mx_1) \right]. \end{aligned} \quad (8)$$

Except the exponents, the above equation is the same as the outer product associative memory of Eq. (1), in which f_m is assumed to be a real function. We further note that the exponents of Eq. (8) represent oblique plane wavefronts, which result in undesired interference fringes at the output plane P₃. It is apparent that if x_1 is made adequately large, the interference fringes can be removed from the output retrieved data by a low pass spatial filtering technique.

A very interesting feature of the system is its controllability. For example, if the MSLM is set at a reasonably low threshold value such that all of the peaks at the SP are responded at the output end of the MSLM, the output is the weighted sum of the associations as expressed by Eq. (8). On the other hand, if the threshold value of the MSLM is adjusted to allow only the highest correlation peak intensity at the SP to be responded at

the readout end of the device, we can call it the winner-take-all. Then the complex output light of Eq. (8) reduces to

$$h''(x,y) = c_1 \left[\int f_m^*(\xi,\eta) f(\xi,\eta) d\xi d\eta \right] h_m(x,y) \times \exp \left[-j \frac{2\pi}{\lambda f} (2x_0 - mx_1) \right], \quad (9)$$

which is proportional to $h_m(x,y)$. Notice that in the above equation, f_m is the input memory closest to the addressing function. Therefore, the process can be interpreted as the retrieval of the information that has the shortest Hamming distance to the m th memory. Furthermore, if $h_m(x,y)$ is equal to $f_m(x,y)$, the system is an autoassociative memory system; otherwise, it is heteroassociative.

3. EXPERIMENTAL RESULTS

Because of easy implementation, the experimental demonstrations are for "winner-take-all" auto- and heteroassociative memories. The first consideration in the experiment is the number of input memories to be used. Under the ideal condition (i.e., the addressing object and the m th input memory are identical and noise free and the transmittance dynamic range of the LCLV is from zero to one), the m th correlation peak intensity value at the SP can be expressed as

$$i_m = \frac{1}{(1+M)^2 |F_m(0,0)|^4} \left| \int \int |f_m(\xi,\eta)|^2 d\xi d\eta \right|^2, \quad (10)$$

where M is the number of input memories and $F_m(0,0)$ is the dc component of the m th memory. This equation shows that the autocorrelation peak intensity on the SPs dramatically decreases as the number of input memories increases. From a physics point of view, this decrease is due to the effect of mutual modulation between the input memories. The effect results in low diffraction efficiency of the LCLV. When the autocorrelation peak is too weak, the poor signal-to-noise ratio will make the thresholding MSLM not operate properly. Thus, for easy demonstration we used three input memories (i.e., $M = 3$) in our experiment.

Another problem we need to consider is the resolution requirement. The size of the SPs has to be very small (about $200 \mu\text{m}$) in order to get the correlation peak (inner product) values only. Therefore, direct readout of the pinholes onto the Fourier transform holograms will produce poor resolution on the output data because of the loss of high frequency components. To overcome this, we used an imaging lens (not shown in Fig. 1) to enlarge the SPs onto the input window of the MSLM. Thus, the illumination beam size on each subhologram can be made large enough. By using this method, the small pinhole size does not put much limitation on the system resolution.

In the experiment, the bias voltages of the MSLM were set so that the device responded only to the brightest correlation peak. Figure 2 shows the experimental results obtained from the autoassociative memory. We used "penn" as the addressing object and the other three words as the reference functions. In our experiment, we blocked a portion of the addressing object and then adjusted the intensity threshold value of the MSLM to examine the variations in the output response. We have observed that when the input is about 50% of the input memory, the system can still produce a satisfactory output result. We also tried blocking different parts of the addressing object. The sys-

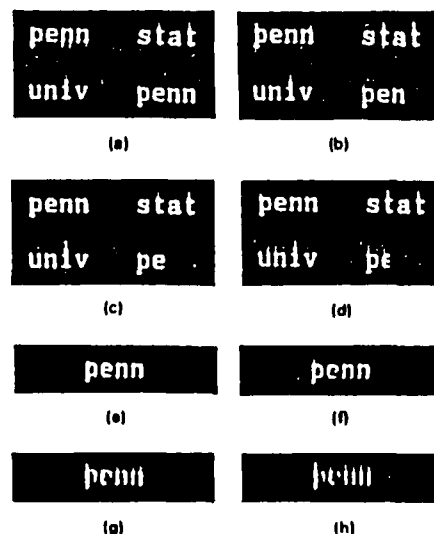


Fig. 2. Experimental results obtained from the autoassociative memory. (a)–(d) Addressing function and reference memories; (e)–(h) corresponding output responses.

tem responded satisfactorily. For example, when we blocked the lower half of the word "penn," the output data showed little difference from the result of Fig. 2(h) subjectively.

Figure 3 demonstrates a set of experimental results of the heteroassociative memory. These results were obtained by arranging the memory bank (i.e., the Fourier transform hologram of "Optical Computing") according to our association rule. When the input is a complete function (i.e., "penn"), a satisfactory output response can be obtained, as shown in Fig. 3(a). If the addressing function is a partial object as given in Figs. 2(b) to 2(d), the corresponding output responses [shown in Figs. 3(b) to 3(d)] deteriorate somewhat but are still recognizable. The system with a complete addressing function can be viewed as a symbolic substituter, as noted by Huang.¹³ On the other hand, the system with an incomplete addressing function can be regarded as an inference machine as introduced by Caulfield.¹⁴

The above experimental results show the feasibility of the technique. We believe that if the input and input memories are preprocessed by an edge enhancement technique and the holograms are optimally recorded on dichromated gelatin film, the performance of the system can be further improved.

4. CONCLUDING REMARKS

We have presented a holographic associative memory system with a controllable MSLM. Since the MSLM is used as an active device in the system, the quality of the output addressed data can be improved as compared with a passive holographic method. Another advantage of the system is its controllability, by which the memory addressing mode can be adjusted to either "winner-take-all" or "weighted sum" operations. The joint transform method has the merit of easy system alignment and real-time filter synthesis. It is apparent that if programmable spatial light modulators were used at the input plane P_1 and the hologram plane P_2 and a feedback loop were constructed between them, the memory capacity of the system could be further enhanced.

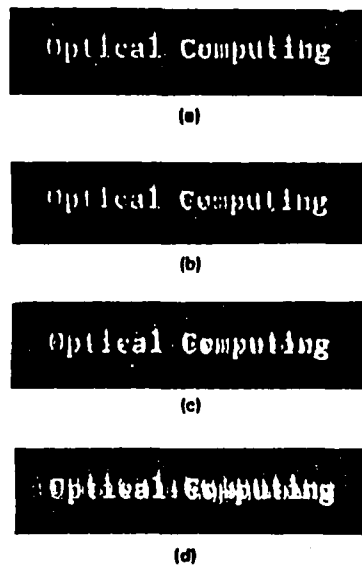


Fig. 3. Experimental results of heteroassociative memory: output results from the complete and partial addressing functions of Figs. 2(a)-2(d), respectively.

5. ACKNOWLEDGMENTS

We acknowledge the support of Rome Air Development Center, Hanscom Air Force Base, under contract No. F19628-87-C-0086, and the MSLM from Hamamatsu Photonics.

6. REFERENCES

1. Y. Owechko, G. J. Dunning, E. Marom, and B. H. Soffer, "Holographic associative memory with nonlinearities in the correlation domain," *Appl. Opt.* 26(10), 1900-1910 (1987).
2. P. J. Van Heerden, "A new optical method of storing and retrieving information," *Appl. Opt.* 2, 387 (1963).
3. D. Gabor, "Associative holographic memories," *IBM J. Res. Dev.* 13, 156 (1969).
4. J. Hopfield, "Neural networks and physical systems with emergent collective computational abilities," *Proc. Natl. Acad. Sci. USA* 79, 2554 (1982).
5. T. Kohonen, *Self-Organization and Associative Memory*, Springer-Verlag, New York (1984).
6. J. Anderson, "A simple neural network generating an interactive memory," *Math. Biosci.* 14, 197 (1972).
7. E. O. Paek and D. Psaltis, "Optical associative memory using Fourier transform holograms," *Opt. Eng.* 26(5), 428-433 (1987).
8. D. Psaltis and N. Farhat, "Optical information processing based on an associative memory model of neural nets with thresholding and feedback," *Opt. Lett.* 10(2), 98 (1985).
9. R. Athale, H. Szu, and C. Friedlander, "Optical implementation of associative memory with controlled nonlinearity in the correlation domain," *Opt. Lett.* 11, 482 (1986).
10. B. Javidi, "Programmable optical associative memory," in *Real-Time Signal Processing for Industrial Applications*, B. Javidi, ed., Proc. SPIE 960, 233-241 (1989).
11. Francis T. S. Yu, C. H. Zhang, S. Jutamulia, "Application of one-step holographic associative memories to symbolic substitution," *Opt. Eng.* 27(5), 399-402 (1988).
12. C. Warde and J. Thackara, "Operating modes of the microchannel spatial light modulator," *Opt. Eng.* 22(6), 695-703 (1983).
13. A. Huang, "Parallel algorithms for optical digital computers," in *Proc. IEEE 10th Int. Optical Computing Conf.*, pp. 13-17, Publ. No. R3C11880-4 (1983).
14. H. J. Caulfield, "Optical inference machines," *Opt. Commun.* 55, 259 (1985).

DIGITAL OPTICAL ARCHITECTURES FOR MULTIPLE MATRIX MULTIPLICATION

Francis T.S. YU and Taiwei LU

Department of Electrical Engineering, Pennsylvania State University, University Park, PA 16802, USA

Received 2 April 1987; revised manuscript received 4 May 1988

Two digital optical architectures utilizing a binary number encoding technique for multiple matrix multiplication are presented. An inner-product method with grating masks is used in one of the architectures, so that multiple matrix multiplication can be performed in parallel. The second architecture, a mixture of systolic array and the inner-product processing method are used. These two architectures can offer high accuracy with moderate speed processing capability.

1. Introduction

Optical matrix multiplication is one of the prominent areas in optical computing. In early 1970's, Lee et al. [1] proposed a method to perform multiple matrix multiplication using Fourier transform property of lenses. Another technique was later developed by Nakano et al. [2]. They utilized a linear array of LED's along with a combination of spherical lenses and cylindrical lenses to perform triple matrix multiplication. Several other methods have also been reported to carry out high speed matrix-matrix and triple matrix multiplication with optics [3-10].

We shall however describe an encoding technique for multiple binary number, where the multiplications and summations of digits are performed in parallel. Nevertheless, we shall discuss two optical architectures for multiple matrix multiplication (MMM) using this technique. The first architecture employs the inner-product method to carry out multiple matrix multiplication. Grating masks are introduced into this architecture to separate the output vectors, so that a fully parallel matrix multiplication can be achieved. The second architecture combines the inner-product method with the systolic array engagement technique. This inner-product-systolic technique is capable for large matrix multiplication and can also be applied to linear and bilinear transformations [11]. Several preliminary experimental demonstrations of these proposed techniques are provided.

2. System description

2.1. Multiple binary number multiplication

In most electronic computers, the binary number multiplication is performed sequentially. The triple multiplication of binary numbers can be carried out as described in the following.

For example, given three binary numbers such as, $a=101$, $b=110$, $c=011$. The product of ab can be obtained by shifting the binary digits of b and then multiply by each bit of a , as shown below

$$\begin{array}{r} 110 \times 1 \\ 110 \times 0 \\ + 110 \times 1 \end{array}$$

$$11110$$

$$ab = a \times b = 101 \times 110 = 11110.$$

Similarly the product of abc can be obtained by shifting the binary digits of c , and then multiply by each bit of ab , as shown in the following

$$\begin{array}{r} 011 \times 0 \\ 011 \times 1 \\ 011 \times 1 \\ 011 \times 1 \\ + 011 \times 1 \end{array}$$

$$1011010$$

$$abc = ab \times c = 11110 \times 011 = 1011010.$$

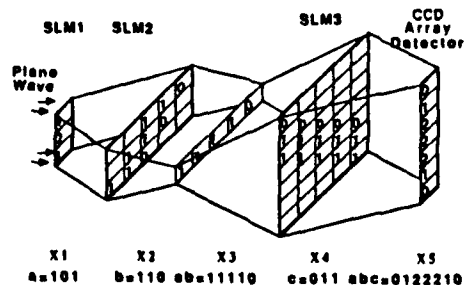


Fig. 1. Optical system for triple binary number multiplication, (a) basic architecture, (b) optical implementation.

However, the triple product of binary numbers can be easily performed in parallel using an optical technique, as shown in fig. 1. We note that a is encoded onto a 1-D spatial light modulator (SLM), while b and c are encoded onto two 2-D SLM's, in which the binary numbers can be shifted by a microcomputer. The digit 1 and 0 can be represented by the transparent and opaque pixels of the SLM. The three SLMs are located at planes X1, X2 and X4, and the intermediate product ab is displayed at plane X3. Thus the product abc can be obtained at the plane X5. To avoid the carries, the products ab and abc are represented by mixed binary form. Fig. 2 shows a hybrid optical system which is able to carry out this operation. Three magneto-optic spatial light modulators (MOSLMs) serve as inputs. The output result is detected by a CCD array and fed back to a high speed memory. A microcomputer is used as a data flow controller. In the system, the multiplications can be performed by the binary transmittances of the SLM's, and the sum can be carried out by simply focusing the light onto a photo detector. An incoherent

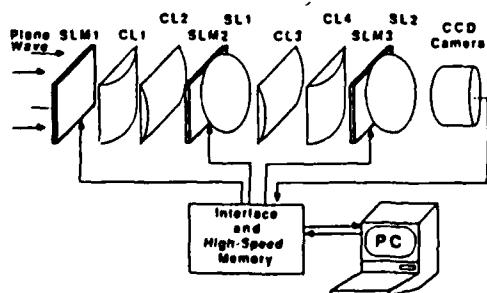


Fig. 2. A hybrid optical system for optical computing.

collimated light is used to illuminate SLM1, in which the cylindrical lens CL1 will horizontally expand each bit of a (SLM1) onto the corresponding row of b (SLM2). Thus the logical AND operations can be taken place at plane X2. Since CL2 is placed behind CL1, it will vertically image a onto the corresponding column of b (SLM2). This optical arrangement will increase the space-bandwidth-product of the processing system. Finally, the spherical lens SL1 will vertically focus the light onto plane X3, to perform the summation. Similarly, a cylindrical lens CL3 at X3 will expand each bit of the intermediate product ab onto the corresponding column of c (SLM3). An unidirectional diffuser is suggested to be placed at the focal plane of SL2, in order to obtain an uniform illumination of vector $[U]$ onto SLM3 [2]. In our experimental setup, instead of unidirectional diffuser, a short focal length cylindrical lens CL3 ($f=10$ mm) is placed near the focal plane of SL1, and SLM3 is placed far enough from CL3 (about 250 mm), then the vertically blurred image would give a uniform illumination on SLM3. CL4 serves the same purpose as CL2. Notice again, spherical lens SL2 will perform the vertical summation and the final result abc can be detected by a CCD detector at plane X5.

2.2 Multiple matrix multiplication (MMM)

We shall describe an architecture for vector-matrix-matrix multiplication. For simplicity, we consider 2×2 matrix multiplication, which can be written as

$$\begin{aligned} \begin{bmatrix} x_{11} & x_{12} \\ x_{21} & x_{22} \end{bmatrix} \begin{bmatrix} y_{11} & y_{12} \\ y_{21} & y_{22} \end{bmatrix} &= \begin{bmatrix} x_{11}y_{11} + x_{12}y_{21} & x_{11}y_{12} + x_{12}y_{22} \\ x_{21}y_{11} + x_{22}y_{21} & x_{21}y_{12} + x_{22}y_{22} \end{bmatrix} \\ &= \begin{bmatrix} u_{11} & u_{12} \\ u_{21} & u_{22} \end{bmatrix} \\ &= \begin{bmatrix} u_{11} & u_{12} \\ u_{21} & u_{22} \end{bmatrix} \end{aligned}$$

where

$$u_{11} = x_{11}y_{11} + x_{12}y_{21}$$

$$u_{12} = x_{11}y_{12} + x_{12}y_{22}$$

$$v_{11} = u_{11}z_{11} + u_{12}z_{21},$$

$$v_{12} = u_{11}z_{12} + u_{12}z_{22},$$

and

$$\begin{aligned} & \begin{bmatrix} x_{21} & x_{22} \end{bmatrix} \begin{bmatrix} y_{11} & y_{12} \\ y_{21} & y_{22} \end{bmatrix} \begin{bmatrix} z_{11} & z_{12} \\ z_{21} & z_{22} \end{bmatrix} \\ &= \begin{bmatrix} x_{21}y_{11} + x_{22}y_{21} & x_{21}y_{12} + x_{22}y_{22} \end{bmatrix} \begin{bmatrix} z_{11} & z_{12} \\ z_{21} & z_{22} \end{bmatrix} \\ &= \begin{bmatrix} u_{21} & u_{22} \end{bmatrix} \begin{bmatrix} z_{11} & z_{12} \\ z_{21} & z_{22} \end{bmatrix} \\ &= \begin{bmatrix} u_{21}z_{11} + u_{22}z_{21} & u_{21}z_{12} + u_{22}z_{22} \end{bmatrix} \\ &= \begin{bmatrix} v_{21} & v_{22} \end{bmatrix}, \end{aligned} \quad (1)$$

where

$$u_{21} = x_{21}y_{11} + x_{22}y_{21},$$

$$u_{22} = x_{21}y_{12} + x_{22}y_{22},$$

$$v_{21} = u_{21}z_{11} + u_{22}z_{21},$$

$$v_{22} = u_{21}z_{12} + u_{22}z_{22}.$$

The matrix $[X]$ can be seen as composed of two vectors $x_1 = [x_{11} \ x_{12}]$ and $x_2 = [x_{21} \ x_{22}]$. An optical architecture to perform this task is shown in fig. 3. Notice that the binary form of vector and matrices $[X]$, $[Y]$ and $[Z]$ can be encoded onto SLM1, SLM2 and SLM3 with a microcomputer, respectively. The spatial encoding form of each element is described in section 2.1. The microcomputer will sequentially shift these vectors into SLM1 which is located at plane X1. Each row of matrix $[Y]$ is multiplied by each corresponding element of vector $[X]$. A vertical summation is carried out between planes X2 and X3 to form vector $[U]$ at plane X3. The same procedures are repeated between planes X3 and X4, X4

and X5 to obtain $[U] \times [Z]$. At the output plane, a CCD detector will sequentially detect each corresponding vector of the output matrix $[V]$, as shown in fig. 3.

2.3. Inner-product architecture using grating masks

To make full use of the parallel processing capability of the optical system, an architecture to perform MMM in parallel is proposed in the following: In figs. 4, time image on plane X3 can be considered as one-dimensional Fourier transform of the input signal at plane X1, by neglecting the existence of SLM2. To separate the two vectors $[u_{11} \ u_{12}]$ and $[u_{21} \ u_{22}]$ at the focal plane X3, two sinusoidal gratings with different spatial frequencies f_1 and f_2 are inserted immediately behind the two input vectors $[x_{11} \ x_{12}]$ and $[x_{21} \ x_{22}]$. The two frequencies are chosen such that the vectors $[u_{11} \ u_{12}]$ and $[u_{21} \ u_{22}]$ can be properly separated at plane X3. In a similar manner, two sinusoidal gratings are placed behind the two vectors $[u_{11} \ u_{12}]$ and $[u_{21} \ u_{22}]$ respectively, at plane X3. Two nonoverlapping vectors $[v_{11} \ v_{12}]$ and $[v_{21} \ v_{22}]$ can be obtained at the output plane X5.

2.4. Systolic-inner-product architecture

We have discussed an optical system for parallel multiple matrix multiplication using the inner-product method. However, this technique requires large size of SLMs to carry out large matrix multiplication. We shall now propose a hybrid optical system to alleviate this shortcoming. Fig. 5 shows the systolic-inner-product architecture. This system uses both the systolic array engagement and inner-product technique, the matrix multiplication is carried out in systolic engagement form, in which the prod-

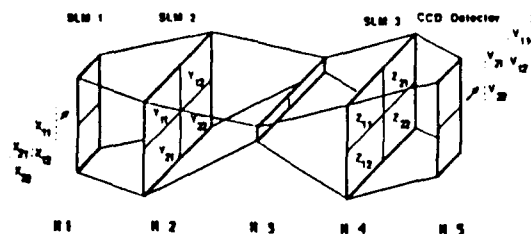


Fig. 3. Architecture for multiple matrix multiplication.

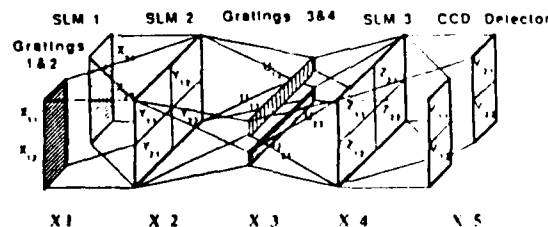


Fig. 4. Architecture for MMM using grating masks.

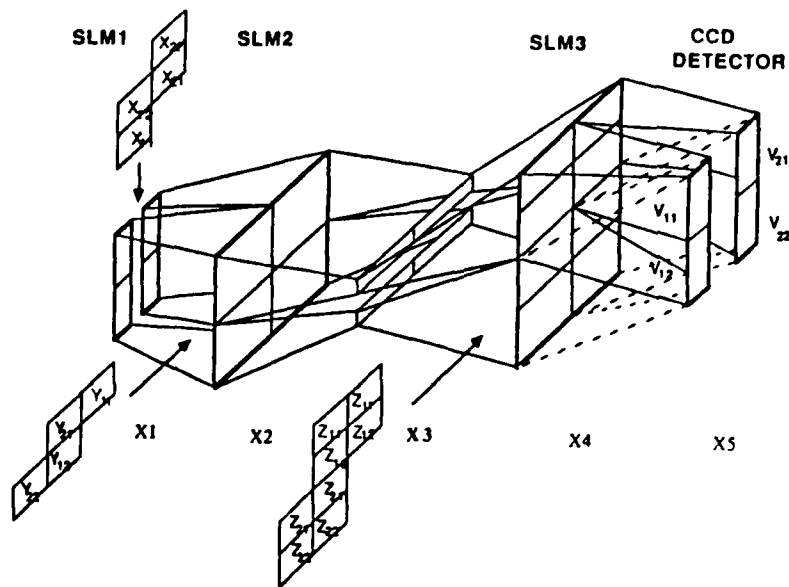


Fig. 5. Architecture for MMM using systolic-inner-product method.

uct of elements is performed in inner-product form depicted in sec. 2.1. Since the hybrid system is basically a microcomputer-based optical processor, the binary number matrix representations in the SLMs can be shifted step-by-step for the systolic array engagement. Array $[X]$ is shifted down to the corresponding columns of SLM1, arrays $[Y]$ and $[Z]$ are shifted to the corresponding rows of SLM2 and SLM3 respectively, as shown in fig. 6. Notice that SLM3 is divided into two parts: upper half and lower half, which are further segmented into a 4×2 array corresponding to the $[Z]$ array. A wedge is placed behind the lower half of SLM3, so that the two parts would overlap on each other at the output plane X5.

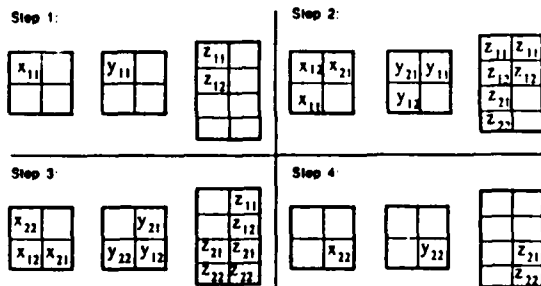


Fig. 6. States of SLMs in four steps.

The intermediate results obtained at the output plane in each step are integrated by a CCD detector. The output matrix $[V]$ is obtained after four steps of time integration. The matrix multiplication can be performed with the hybrid processor shown in fig. 2. There is however a price we paid for using this technique, namely the speed. For example a 2×2 matrix multiplication requires a four-step operation. Nevertheless, the required size of the SLMs used in the processor can be substantially smaller by decomposing the matrices and then applying the systolic-inner-product method.

3. Experimental demonstration

Several experimental demonstrations have been carried out with the proposed hybrid optical architectures for multiple matrix multiplication. We have first use a triple binary number multiplication for the experiment, as illustrated in figs. 1 and 7. To avoid the coherent artifact noise, a white light source is used to carry out the processing. The focal length of the cylindrical and spherical lenses are 10 mm and 100 mm, respectively. To show the feasibility operation of the proposed technique, binary coded transparent

masks, instead of SLMs, are used in our experiments.

Fig. 7(a) shows the binary mask representation of $a=101$, $b=110$ and $c=011$, respectively. The output result is shown in fig. 7(b). Fig. 7(c) shows the output photometer trace, which corresponds to the mixed binary number representation of $abc=0122210$. By proper thresholding of the output signal, the result can be converted into binary form, which is $abc=1011010$, as shown in fig. 7(d).

For another experimental demonstration, we show that triple matrix multiplication can be obtained with a hybrid optical architecture of fig. 3. The binary representation of the encoded masks are shown in fig. 8(a), which represents the matrices in the following,

$$[X] = \begin{bmatrix} 00100 & 01000 \\ 00010 & 00011 \end{bmatrix}, \quad [Y] = \begin{bmatrix} 00100 & 00001 \\ 00011 & 00010 \end{bmatrix},$$

$$[Z] = \begin{bmatrix} 10000 & 00010 \\ 01000 & 00110 \end{bmatrix}.$$

Again fig. 8(b) shows the output intensity distribution, and fig. 8(c) shows the mixed binary form of the output matrix $[V]$, i.e.,

$$[V] = \begin{bmatrix} v_{11} & v_{12} \\ v_{21} & v_{22} \end{bmatrix} \\ = \begin{bmatrix} 0001121001100 & 0001331011000 \\ 0000010132000 & 0000101102000 \end{bmatrix}.$$

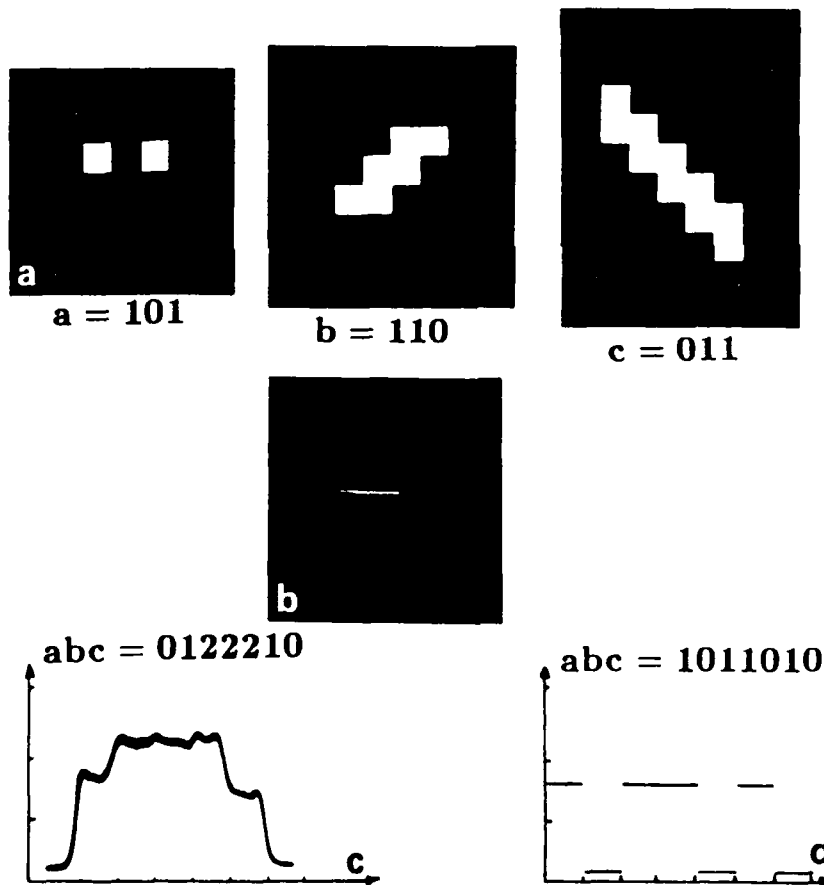
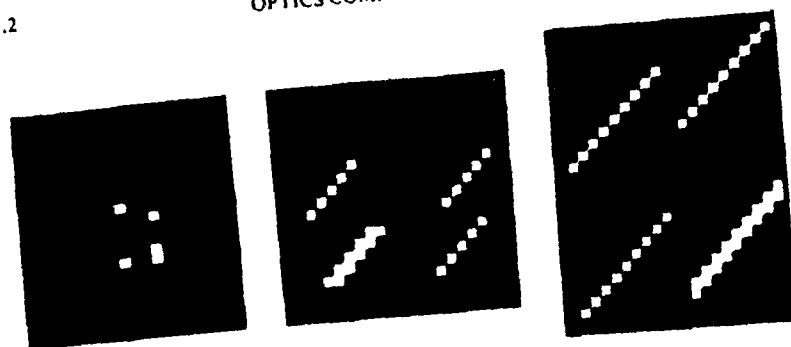
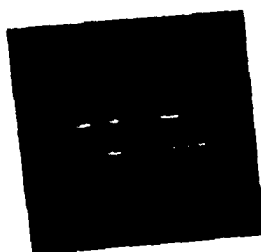


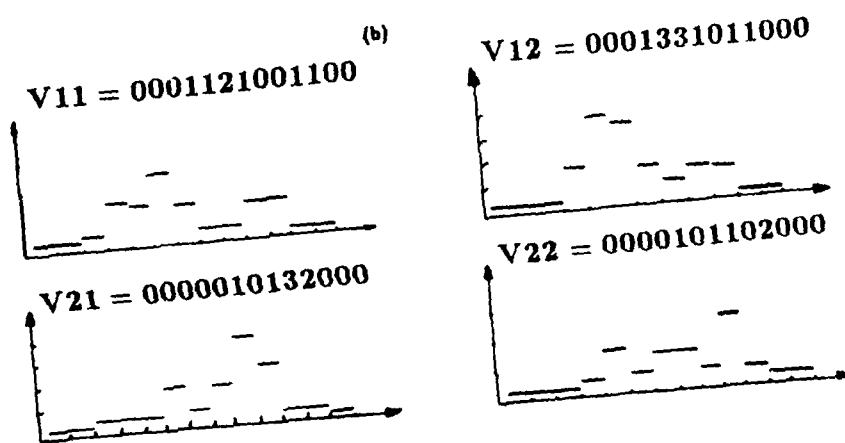
Fig. 7. (a) Three masks for triple binary number multiplication. (b) Output signals detected on plane X5. (c) Result displayed on an oscilloscope in mixed binary form. (d) Final result in binary form.



(a)



(b)



(c)

Fig. 8. (a) Three 2×2 matrix masks for MMM. (b) Output signals detected on plane X5. (c) Output matrix $[V]$ in mixed binary form.

The corresponding output matrix $[V]$ in binary representation is given by

$$[V] = \begin{bmatrix} v_{11} & v_{12} \\ v_{21} & v_{22} \end{bmatrix} = \begin{bmatrix} 0010001001100 & 0011011011000 \\ 0000011100000 & 0000101110000 \end{bmatrix}$$

4. Discussion

The binary number encoding technique provides the optical system a high accuracy and parallel processing capability. The inner-product architecture offers a higher speed operation, whereas the systolic-inner-product architecture trades off a part of the

parallelism for more flexibility. The bottleneck of the proposed hybrid optical processor is the input and output interfacing between electronic and photonic signals. The electronically addressed SLMs and light detection device limited the overall processing speed of the hybrid optical system. However, due to the rapid development in the areas of optical storage and optical logic material, it is expected that the bottleneck problem would be alleviated by using the high speed optical memory and optical parallel logic elements. A high speed process would be achieved by the data flow in the parallel optical processor.

5. Conclusion

We have presented a technique that multiple binary number multiplication can be parallelly performed by a microcomputer-based optical processor. Two basic architectures to perform multiple matrix multiplication are discussed. In the first architecture, we used an inner-product technique, such that multiple matrix multiplication can be simultaneously carried out. For the other architecture, we used a systolic-inner-product technique to carry out the multiple matrix multiplication. Although, in principle, the inner-product technique offers a higher speed operation, however, it requires larger SLMs to carry out the process. Since both techniques use either mixed binary or binary representation, the system

would offer high accuracy with moderate speed multiple matrix multiplication.

Acknowledgement

We wish to acknowledge the support of U.S. Air Force Rome Air Development Center, Hanscom Air Force Base, under contract No. F19628-87-C-0086.

References

- [1] R.A. Heinz, J.O. Artman and S.H. Lee, Appl. Optics 9 (1970) 2161.
- [2] H. Nakano and K. Hotate, Appl. Optics 24 (1985) 4238.
- [3] J.W. Goodman, A.R. Dias and L.M. Woody, Optics Lett. 2 (1978) 1.
- [4] A.A. Sawchuk and B.K. Jenkins, Proc. SPIE Vol. 625 (1986) 143.
- [5] D. Psaltis and R.A. Athale, Appl. Optics 25 (1986) 3071.
- [6] R.A. Athale and J.N. Lee, Optics Lett. 8 (1983) 590.
- [7] D. Psaltis, D. Casasent and M. Carlotto, Optics Lett. 4 (1979) 348.
- [8] F.T.S. Yu, M.F. Cao and J.E. Ludman, Opt. Eng. 25 (1986) 846.
- [9] R.P. Bocker, H.J. Caulfield and K. Bromley, Appl. Optics 22 (1983) 804.
- [10] F.T.S. Yu, M.F. Cao and T. Lu, SPIE Vol. 698 (1986) 276.
- [11] F.T.S. Yu, T. Lu and M.F. Cao, Technical Digest of OSA 1987 Annual Meeting, Vol. 22 (1987) 106.

may provide a means of improving the accuracy of correlation detection.

2. Principle

It is well known that phase conjugation can be produced with a photo-refractive crystal. With referring to the JTC in fig. 1, the readout beam is adjusted beyond the coherent length with respect to the writing beams. In other words, the setup represents a two-wave mixing configuration with a real-time readout beam. Notice that the expanded collimated Ar⁺ laser beam ($\lambda=0.5145 \mu\text{m}$) is divided into three paths. One is directed toward the photo-refractive crystal (BSO, $10 \times 10 \times 2 \text{ mm}^3$) by mirror M_2 and serves as the reference beam. The second is used to illuminate the input objects O_1 and O_2 , which are imaged onto the crystal by lens L_1 . The third is directed by mirror M_1 , M_5 , M_4 and serves as the readout beam. The reconstructed beam from the crystal is then imaged back to the input objects O_1 and O_2 for phase distortion removal. After passing through the input objects, the beam is then joint transformed in the output plane P_0 by lens L_2 , via a beam splitter BS_3 . We notice that a half wave plate Q , between the BSO crystal and mirror M_4 , is used to rotate the polarization of the readout beam. An analyzer A located at the front of the output plane is used to reduce the light scattered from the optical elements in the system.

With reference to the optical configuration of fig. 1, the object beam can be written as

$$\begin{aligned} O(x, y) \exp[i\phi(x, y)] \\ = O_1(x-b, y) \exp[i\phi_1(x-b, y)] \\ = O_2(x+b, y) \exp[i\phi_2(x+b, y)], \end{aligned} \quad (1)$$

where O_1 , O_2 , ϕ_1 and ϕ_2 are the amplitude and phase distortion of the input objects, respectively, b is the mean separation of the two input objects, and O_1 , O_2 are assumed positive real. At the image plane (i.e. the crystal), the object beam is given by

$$\begin{aligned} O(x/M, y/M) \exp[i\phi(x/M, y/M)] \\ \times \exp[ik(x^2+y^2)/2L], \end{aligned} \quad (2)$$

where M represents the magnification factor of the

imaging system, $L=s-f$, s is the image distance, f is the focal length of lens L_1 , $k=2\pi/\lambda$, λ is the wavelength of the light source.

Thus, the reconstructed beam emerging from the crystal is given by

$$\begin{aligned} O'(x/M, y/M) \exp[-i\phi(x/M, y/M)] \\ \times \exp[-ik(x^2+y^2)/2L] \exp[i\theta(x/M, y/M)]. \end{aligned} \quad (3)$$

Notice that expression (3) does not represent the exact phase conjugation of expression (2). The amplitude distribution of $O'(x, y)$ deviates somewhat from $O(x, y)$, which is primarily due to the nonlinearity of the BSO crystal [6]. A phase shift $\theta(x, y)$ between the phase conjugation and the reconstructed beam is also introduced. Later we will see that $\theta(x, y)$ is dependent on the intensity ratio R of the object beam and the reference beam. If there is no voltage applied on the BSO crystal, $\theta(x, y)$ would represent a constant phase of 90° .

As can be seen in fig. 1, the reconstructed beam, imaged back on the object plane, can be written as

$$O'(x, y) \exp[-i\phi(x, y)] \exp[i\theta(x, y)]. \quad (4)$$

After passing through the input objects, the complex light distribution becomes

$$O(x, y) O'(x, y) \exp[i\theta(x, y)]. \quad (5)$$

This expression shows that the phase distortion $\phi(x, y)$ of the input objects can essentially be removed, while the additional amplitude and phase modulation due to the nonlinearity of the BSO remain.

3. Phase distortion compensation

The phase distortion of the input objects (i.e. due to the SLM) can severely degrade the correlation characteristics. We have computer simulated some of these effects. The simulations were obtained with a test input pattern joint correlated with the same pattern added with random phase noise. We assumed that the random phase noise has a uniform probability distribution over a phase interval $[-\sigma, \sigma]$. Fig. 2 shows a plot of correlation peak intensity as a function of phase deviation σ . From this graph, we see that the normalized peak drop of 0.5 corre-

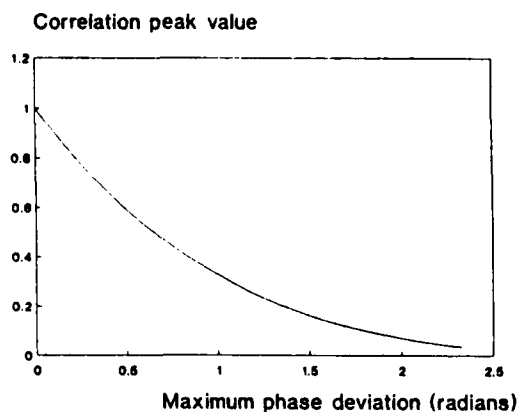


Fig. 2. Correlation peak intensity degraded by phase noise.

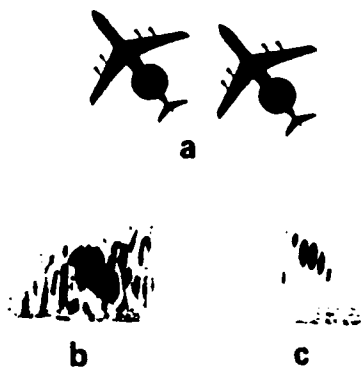


Fig. 3. Joint Fourier transform spectra. (a) A pair of input subjects with random noise. (b) Their joint transform spectrum. (c) The joint transform spectrum with phase compensation.

sponds to a phase deviation of 0.6 radians. In other words, the phase distortion of a SLM should not exceed $1/10$ wavelength, which corresponds to 0.6 radians, otherwise the correlation peak would be severely degraded. However, most SLMs do not meet this requirement.

In order to demonstrate the phase compensation with phase conjugate technique, a pair of input objects, shown in fig. 3a, is added with a random phase plate. Their joint transform spectrum is shown in fig. 3b. Notice that the spectrum is severely corrupted by the phase disturbances. However, with the phase compensation technique, the spectrum, obtained with the experimental setup described in fig. 1, is relatively free from the disturbance as shown in fig. 3c.

Fig. 4 shows the correlation spots reconstructed from these two cases. For no phase compensation, the correlation spots are heavily embedded in random noise, as pictured in fig. 4a, while with phase compensation, the correlation spots can clearly be seen in fig. 4b.

It is, however, necessary to stress the role played by the imaging lens L_1 . First, lens L_1 ensures that all the light scattered by the input objects can be directed toward the BSO crystal (assume that L_1 has a sufficiently large aperture.). Secondly, the reconstructed beam is not the exact phase conjugated beam, it has an additional phase modulation $\theta(x, y)$. Thus, it is apparent that if no imaging lens is employed, the light ray emerging from an arbitrary object point would not longer be reconstructed back at the same point. By using the imaging lens, it ensures that every light ray emerging from the objects would be reconstructed back. As long as all the light scat-

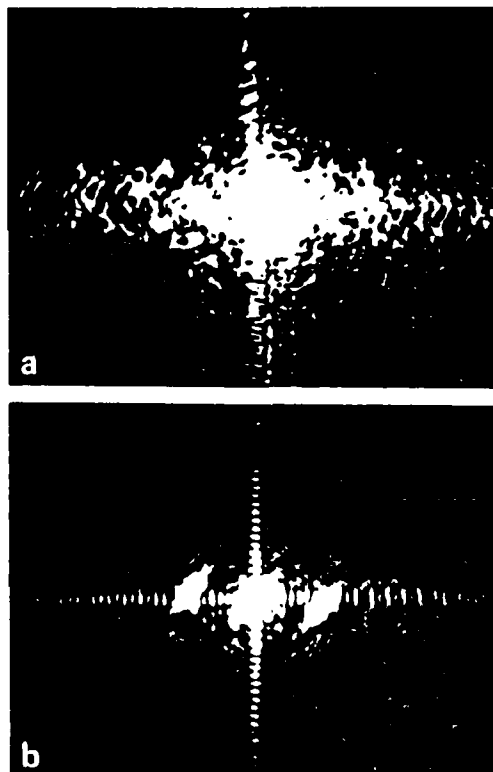


Fig. 4. Reconstructed correlation spots. (a) Without phase compensation. (b) With phase compensation.

tered by the phase distortion of the objects are collected by the aperture of L_1 , the phase distortion of the objects can be compensated by this technique. However, if the aperture is not large enough, the high spatial frequency components of the phase distortion could not be compensated.

4. Pre-encoding

The reconstructed beam, as expressed in eq. (5), is different from the object function $O(x, y)$. The additional amplitude and phase factors within the reconstructed beam can be used for object pre-encoding in a JTC, for which the correlation characteristics can be improved. These factors are dependent on object and reference beam ratio R [6], as defined by

$$R(x, y) = \frac{O^2(x/M, y/M)}{I_r}, \quad (6)$$

where I_r is the intensity of the reference beam.

The phase modulation $\theta(x, y)$ represents the phase difference between the conjugation of the object beam and the actual reconstruction beam (see expression (3)). This phenomenon is due to the interaction between the writing beams [7]. According to Vahey [8], the phase deviation between the writing beams varies along the propagation within the crystal and can be expressed as

$$\psi(z) = \psi(0) - \cotan(\phi_s) \ln\left(\frac{\cosh[Q(z)]}{\cosh[Q(0)]}\right), \quad (7)$$

where

$$Q(z) = 2\Gamma z \sin(\phi_s) + \tan^{-1}[(1-R)/(1+R)], \quad (8)$$

Γ is the coupling constant, ϕ_s is the phase shift between the writing interference pattern and the induced index grating, and $\psi(0)$ is the initial phase deviation between the writing beams. This phase variation would produce grating bending within the crystal. When a readout beam illuminates the crystal, the reconstructed wavefront from the bended volume grating would have a phase shift $\theta(x, y)$ relative to the conjugate wavefront of the object beam. From eqs. (7), (8) and (6), we notice that this phase

shift $\theta(x, y)$ is dependent on R and directly related to the object intensity distribution $O(x, y)$. Therefore the phase modulation $\theta(x, y)$ can be utilized to encode the object functions.

We have computer simulated the effects of pre-encoding the object functions in a JTC. Fig. 5 is the intensity distributions of two objects to be correlated. The autocorrelation curve (for the triangle object) and their cross correlation curve are shown in figs. 6(a) and (b), respectively. We notice that the wide autocorrelation curve and high cross correlation intensity are not desirable. However, if a phase encoding (assumed linear, that is $\theta(x, y) \propto O(x, y)$) is added to the objects the correlation characteristics are improved substantially, as shown in fig. 7, where the maximum encoded phase θ_{\max} is 8 radians. By comparing fig. 6 with fig. 7, we notice that the width of the autocorrelation reduces and the cross correlation intensity decreases. Furthermore, fig. 8 illustrates how the autocorrelation width decreases monotonically as the increase of the linear phase encoding.

In view of expression (5), object encoding can also be accomplished with amplitude modulation. It is obvious that $O'(x, y)$ is proportional to the diffrac-



Fig. 5. Intensity distributions of the object to be correlated.

Correlation

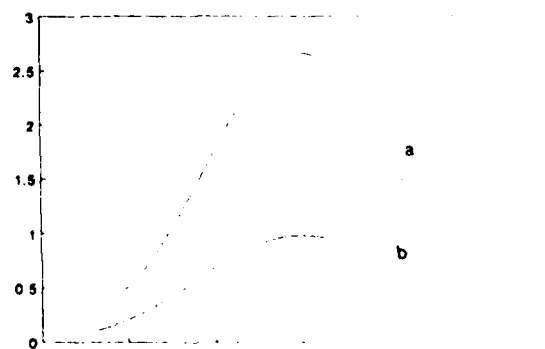


Fig. 6. Correlation without phase encoding. (a) Autocorrelation (b) Cross correlation.

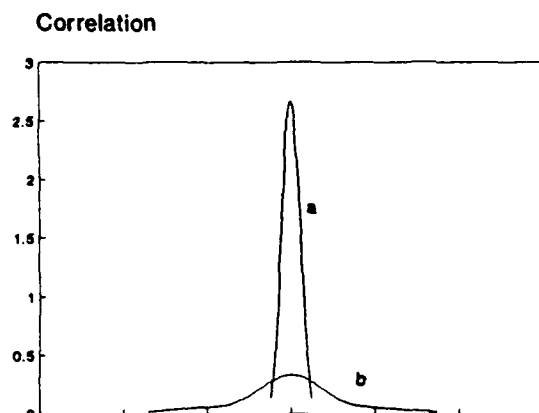


Fig. 7. Correlation with phase encoding, normalized by the cross correlation peak intensity in fig. 6. The maximum encoded phase θ_{\max} is 8 radians. (a) Autocorrelation. (b) Cross correlation.

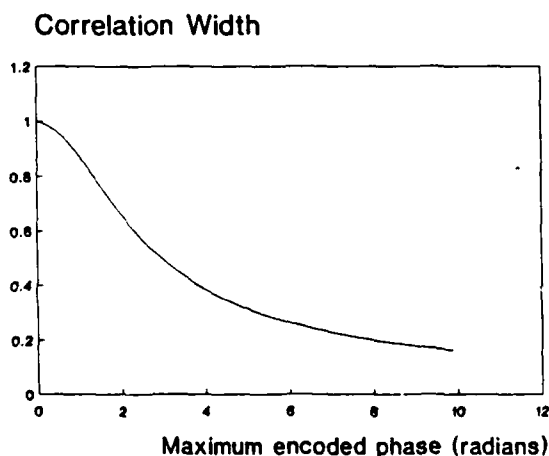


Fig. 8. Autocorrelation width (50% down width) decreases with the increase of linear phase encoding. X axis represents the maximum encoded phase θ_{\max} .

tion efficiency η of the phase grating within the crystal. With reference to Ochoa et al. [6], the diffraction efficiency η of the phase grating in a photo-refractive material is related to the intensity ratio R of two writing beams as

$$\begin{aligned} \eta(x, y) &\propto R, & R < 1. \\ &\propto 1/r, & R > 1. \end{aligned} \quad (9)$$

Thus, different amplitude encoding may be accom-

plished by controlling the intensity of the reference beam, for example, edge enhancement, which is a desirable pre-processing in a JTC [9]. Some discussion for amplitude encoding may be found in ref. [6].

5. Conclusion

Several applications of phase conjugation technique in a JTC have been investigated. It is shown that phase distortion in the input objects (due to SLM) in a coherent image processing system can be efficiently compensated by using phase conjugation technique. The additional amplitude or phase modulations produced by the nonlinearity of phase conjugation can be utilized to pre-encode the object functions, for which correlation characteristics can be improved. Computer simulations indicate that phase pre-encoded objects improve the accuracy of correlation detection, which is resulted from smaller autocorrelation spots and lower cross correlation intensity. This encoding technique would find application to the research of dynamic pattern recognition and robotic vision.

Acknowledgements

We acknowledge the support of the U.S. Air Force Rome Air Development Center, Hanscom Air Force Base, under contract no. F19628-87-C-0086.

References

- [1] R.A. Fisher, ed., Optical phase conjugation (New York, Academic Press, 1983).
- [2] J. Feinberg, Optics Lett. 7 (1982) 486.
- [3] C.S. Weaver and J.W. Goodman, Appl. Optics 5 (1966) 1248.
- [4] F.T.S. Yu and X.J. Lu, Optics Com. 52 (1984) 47.
- [5] B. Loiseaux, G. Illiaquer and J.P. Huignard, Opt. Eng. 24 (1985) 144.
- [6] E. Ochoa, L. Hesselink and J.W. Goodman, Appl. Optics 24 (1985) 1826.
- [7] N.V. Kukhtarev, V.B. Markov, S.G. Odulov, M.S. Soskin and V.L. Vinetskii, Ferroelectrics 22 (1979) 949.
- [8] D.W. Vahey, J. Appl. Phys. 46 (1975) 3510.
- [9] F.T.S. Yu, X. Li, E. Tam, S. Jutamulia and D.A. Gregory, Rotational invariant pattern recognition with a programmable joint transform correlator, submitted to Appl. Optics.

Phase measurement of a Fourier spectrum by a fringe-scanning phase-conjugate interferometer

Francis T. S. Yu, Shudong Wu, and A. W. Mayers

Department of Electrical Engineering, Pennsylvania State University, University Park, Pennsylvania 16802

Jacques E. Ludman

Rome Air Development Center, Hanscom Air Force Base, Massachusetts 01731

Received March 20, 1989; accepted July 26, 1989

We present a novel method for obtaining the phase distribution of an object spectrum by using a fringe-scanning phase-conjugate interferometer. A detailed analysis of the proposed technique is provided, and experimental demonstrations for validating this technique are also given. The major advantages of this method are its potentially high accuracy and its low space-bandwidth-product requirement for the detection system.

Any object function $O(x, y)$ can be represented in the Fourier frequency domain as $|\tilde{O}(u, v)|\exp[j\phi(u, v)]$, where (u, v) is the spatial-frequency coordinate system. However, in many applications the phase distribution $\phi(u, v)$ is more important than the amplitude information $|\tilde{O}(u, v)|$. To measure the phase distribution of an object spectrum, an interferometric method that uses a reference beam may be used. There are two general types of reference beam that can be employed for this purpose: (1) a reference beam having a uniform amplitude and phase distribution (e.g., an oblique plane wave) and (2) a phase-conjugated object spectrum. Thus, in the first case, a problem of fringe contrast variation exists because of the nonuniform object spectrum. On the other hand, by using a phase-conjugate spectrum as the reference, uniform contrast fringes can be obtained. However, since the measured phase is $2\phi(u, v)$, a π phase ambiguity problem exists.

In a recent paper¹ Xu proposed a joint transform configuration that uses a conjugate reference beam for the phase measurement, in which the intensity of the real part and the imaginary part of the object spectrum can be obtained. The method has some drawbacks. First, his technique introduces a carrier frequency that requires a higher space-bandwidth-product detection system. Second, the signs of the real and the imaginary parts of the object spectrum cannot be uniquely determined, resulting in four ambiguous phase values. Third, the phase measurement is derived primarily from two intensity distributions and is vulnerable to system noise.

In this Letter we describe a technique that uses a fringe-scanning phase-conjugate interferometer² (PCI) for the phase measurement of the object spectrum. One of the advantages of using a PCI is the elimination of carrier frequency, for which a low space-bandwidth detection system can be used. With a PCI the output interferometric pattern is not affected by the variations of the optical path difference. Therefore it is not sensitive to turbulence and is capa-

ble of self-aligning. To improve the accuracy of the measurement, a fringe-scanning method is introduced into the system. In a PCI, however, fringe scanning cannot be achieved by changing the optical path difference, as in conventional fringe-scanning techniques. In a recent paper Wu *et al.*³ suggested a polarization-encoding method that we will apply for fringe scanning in the PCI.

Figure 1 shows the proposed experimental setup. The light source is a 45° linearly polarized collimated Ar⁺ laser beam ($\lambda = 488$ nm). A Bi₁₂SO₂₀ (BSO) crystal is used as the phase-conjugate mirror. Two pumping beams are derived from beam splitters BS₁ and BS₂, respectively, and then directed toward the BSO crystal at opposite directions with mirrors M₁-

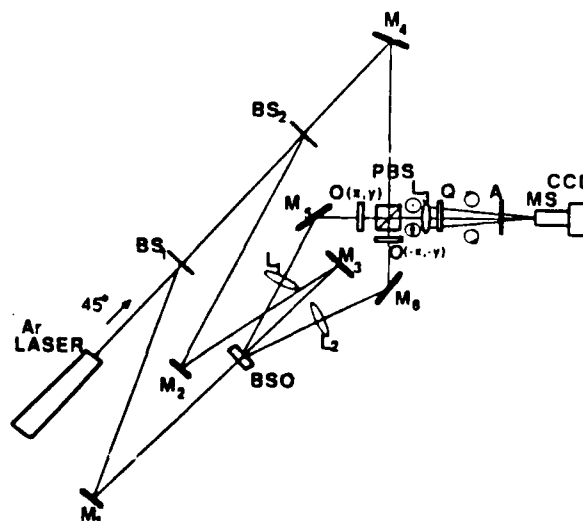


Fig. 1. Experimental setup for phase measurement. M's, mirrors; BS's, beam splitters; PBS, polarizing beam splitter; L's, lenses; Q, quarter-wave plate; A, analyzer; MS, microscope; CCD, charge-coupled device camera.

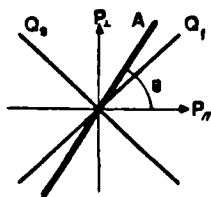


Fig. 2. Orientation of polarizing components: P_{\perp} , P_{\parallel} , S and P polarization, respectively; Q_s , Q_f , slow and fast axes, respectively, of the quarter-wave plate; A , analyzer.

M_3 . The beam reflected by M_4 is split by the polarizing beam splitter PBS. The resulting beams illuminate the object transparencies $O(x, y)$ and $O(-x, -y)$ and are directed toward the BSO crystal by mirrors M_5 and M_6 , respectively. Thus two phase-conjugate beams emerge from the BSO crystal, retracing the input paths to be combined by the polarizing beam splitter as the output of the PCI. In the PCI all phase distortions are automatically compensated for. Notice that an object transparency $O(x, y)$ is placed in one arm of the interferometer, and its antisymmetric copy $O(-x, -y)$ is placed in the other arm. [A change of relative position between $O(x, y)$ and $O(-x, -y)$ in the PCI would only introduce a linear phase factor to the object spectrum and is equivalent to a change of the object origin.] Thus the corresponding object spectra $\tilde{O}(u, v)$ and $\tilde{O}^*(u, v)$ are present at the back focal plane of lens L_3 .

With reference to the PBS, two output phase-conjugated beams, in the two arms of the interferometer, are orthogonally linearly polarized. The corresponding output spectra can be expressed in a Jones vector as

$$\begin{bmatrix} O(x, y) \\ O(-x, -y) \end{bmatrix} \xrightarrow{FT} \begin{bmatrix} |\tilde{O}(u, v)| \exp[j\phi(u, v)] \\ |\tilde{O}(u, v)| \exp[-j\phi(u, v)] \end{bmatrix}. \quad (1)$$

The quarter-wave plate Q in Fig. 1 is at a 45° (angle) orientation, as shown in Fig. 2. The Jones vector behind the quarter-wave plate Q can then be written as

$$\begin{bmatrix} j & 1 \\ 1 & j \end{bmatrix} |\tilde{O}(u, v)| \begin{bmatrix} \exp[j\phi(u, v)] \\ \exp[-j\phi(u, v)] \end{bmatrix} \\ = 2|\tilde{O}(u, v)| \exp\left(j\frac{\pi}{4}\right) \begin{bmatrix} \cos\left[\phi(u, v) + \frac{\pi}{4}\right] \\ \sin\left[\phi(u, v) + \frac{\pi}{4}\right] \end{bmatrix}. \quad (2)$$

The corresponding intensity distribution at the back focal plane of L_3 , behind the analyzer, can be expressed as

$$I(u, v, \theta) = 2|\tilde{O}(u, v)|^2 [1 - \sin[2\phi(u, v) - 2\theta]], \quad (3)$$

which represents an interferometric pattern, where θ is the orientation angle of the analyzer (see Fig. 2). From this result, we see that an additional phase constant (i.e., 2θ) is introduced. It is apparent that, by rotating the analyzer, fringe scanning of the interferometric pattern can be obtained.

By referring to the conventional fringe-scanning techniques,⁴ one may derive the phase distribution from the intensity variation with θ , $I(u, v, \theta)$:

$$2\phi(u, v) = \tan^{-1} \left[\frac{B(u, v)}{A(u, v)} \right], \quad (4)$$

where

$$A(u, v) = n\pi |O(u, v)|^2 \cos[2\phi(u, v)]$$

$$= \int_0^{2\pi} I(u, v, \theta) \sin 2\theta d\theta,$$

$$B(u, v) = n\pi |O(u, v)|^2 \sin[2\phi(u, v)]$$

$$= \int_0^{2\pi} I(u, v, \theta) \cos 2\theta d\theta, \quad (5)$$

and n is an integer. In practical measurements, instead of performing the continuous integration, one uses discrete summations. This can be expressed as

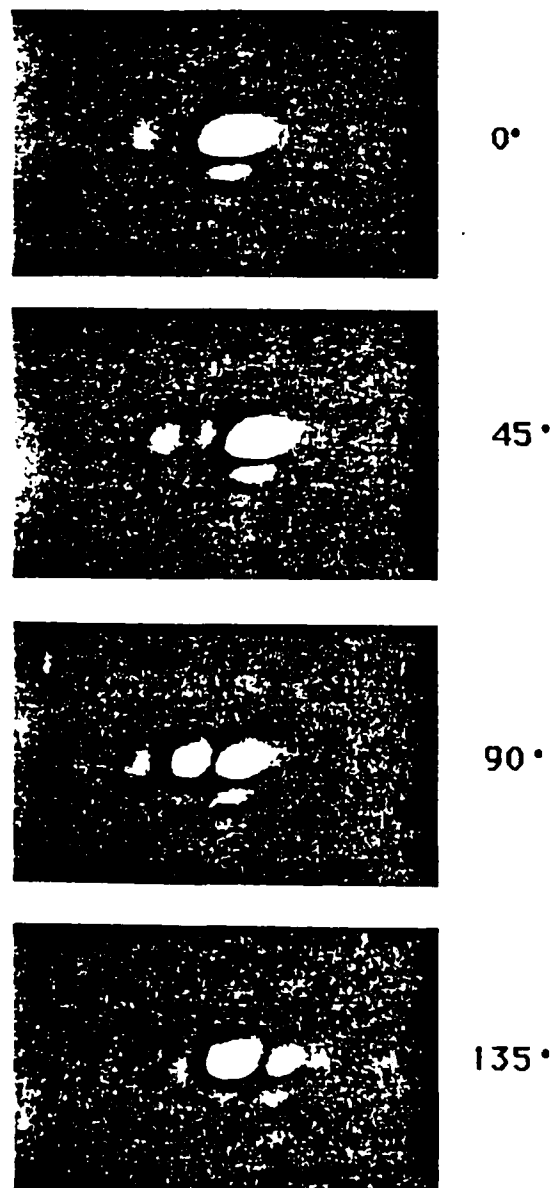


Fig. 3. Output fringe shift with respect to the analyzer orientation angle.

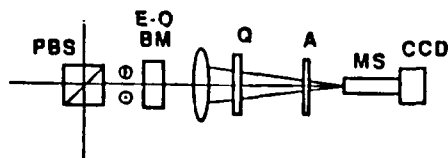


Fig. 4. Implementation of an electro-optic birefringence modulator (E-O BM). Other abbreviations as in Fig. 1.

$$A(u, v) = \sum_{i=1}^m I(u, v, \theta_i) \sin 2\theta_i,$$

$$B(u, v) = \sum_{i=1}^m I(u, v, \theta_i) \cos 2\theta_i, \quad (6)$$

where $\theta_i = i\pi/m$ and m is the number of summation steps. The fringe-scanning technique reduces four ambiguous phase values to two.

In order to demonstrate the principle of the proposed technique, a rectangular aperture with a small displacement from the optical axis in the horizontal direction [i.e., $O(x, y)$] is used as the object. Its anti-symmetric copy, $O(-x, -y)$, is in fact the same aperture but with the displacement in the opposite direction from the optical axis. Figure 3 shows the output interferometric patterns obtained with this proposed PCI, with different angular orientations of the analyzer. Because the diffraction efficiency of our phase-conjugate mirror is low, the sidelobes of the object spectrum cannot be seen clearly in the pictures. We noted that the interferometric fringes are linearly shifted with the changing of θ . This indicates that the phase of the object spectrum is a linear distribution. The period of the fringe shifting with θ is 180° .

One of the striking features of the fringe-scanning technique in the PCI is its invulnerability to noise. Let us now look at the standard deviation of the phase error due to noise, as given by⁴

$$\sigma_\phi = \frac{1}{\sqrt{m} \text{ s/n}}, \quad (7)$$

where s/n is the output intensity signal-to-noise ratio. From this equation we see that phase error σ_ϕ decreases as the summation steps increase.

To increase the measurement speed, an electro-optic birefringence modulator can be used between the PBS and the transform lens L_3 , as illustrated in Fig. 4.

Instead of rotating the analyzer, one can dramatically increase the measured speed using an electro-optic modulator. We now assume that the electro-optic modulator introduces a birefringence phase shift α . The right-hand side of Eq. (1) can now be written as

$$\begin{pmatrix} |\tilde{O}(u, v)| \exp[j\phi(u, v)] \\ |\tilde{O}(u, v)| \exp[-j\phi((u, v) + \alpha)] \end{pmatrix}. \quad (8)$$

Thus Eq. (3) becomes

$$I(u, v, \theta, \alpha) = 2|\tilde{O}(u, v)|^2 [1 - \sin[2\phi(u, v) - 2\theta - \alpha]]. \quad (9)$$

From this equation we see that, by simply changing the modulation angle α , we can accomplish rapid fringe scanning.

It is well known that all fringe-scanning techniques require certain computations. From Eqs. (6), the number of multiplications required is $2mn^2$, where n^2 is the number of sampling points over the spectrum plane. If a digital fast-Fourier-transform algorithm were used, the required number of multiplications for $n \times n$ input data would be of the order of $4n^2 \log_2 n$. This does not, however, appear to be significantly different from the number of multiplications $2mn^2$. In the fringe-scanning method the factors to be multiplied are fixed to only a few values. Instead of performing real-time multiplications, one can use a data look-up table to speed up the computational process. Moreover, the spectral content of the object in the Fourier plane is concentrated mostly in some specific regions. It is generally not necessary to compute the phase distribution over the entire $n \times n$ points. In other words, the computation can be selected based on the spectral intensity distribution; thus the amount of computational time can be substantially reduced.

We acknowledge the support of the U.S. Air Force Rome Air Development Center at Hanscom Air Force Base under contract F19628-87-C-0096.

References

1. K. Xu, *Opt. Commun.* 67, 21 (1988).
2. A. E. Chion, P. Yeh, and M. Khoshnevisan, *Opt. Eng.* 27, 385 (1988).
3. S. Wu, C. Xu, and Z. Wang, in *ICO-13 Conference Digest* (ICO Organizing Committee, Sapporo, Japan, 1984), p. 458.
4. J. H. Brunning, in *Optical Shop Testing*, D. Malacara, ed. (Wiley, New York, 1978), p. 409.

AN ADAPTIVE OPTICAL NEURAL NETWORK USING A HIGH RESOLUTION VIDEO MONITOR

Shudong Wu, Taiwei Lu, Xin Xu, and Francis T. S. Yu
Department of Electrical Engineering
The Pennsylvania State University
University Park, PA 16802

KEY TERMS

Optical neural network, high resolution video monitor, interconnection weight matrix, Hopfield model, orthogonal projection algorithm

ABSTRACT

An adaptive hybrid optical neural network using a high resolution video monitor as a programmable associative memory is proposed. This architecture is capable of implementing larger numbers of neurons with higher dynamic range. The proposed system can be operated in a high speed asynchronous mode with parallel feedback loop. The orthogonal projection algorithm as applied to the proposed system to increase the error correction ability is given.

1. INTRODUCTION

In recent years attention has been drawn to the problems concerning optical implementation of neural networks. Recently, a two-dimensional (2-D) optical neural network has been synthesized by Farhat and Psaltis, for which they used the basic concept of vector-matrix optical processing [1]. This optical neural network is composed of a linear array of LEDs as an input device, which is interconnected to a weighting mask by a lenslet array. To provide the network with self-organization and learning capabilities, a programmable spatial light modulator (SLM) with fine resolution and a large number of distinguishable gray levels is needed as an interconnection weight matrix (IWM). However, currently available SLMs have small space-bandwidth products and limited gray levels, making it difficult to implement such an optical neural network.

In this paper, an optical architecture is proposed, in which a high resolution video monitor is used as a programmable weighting matrix as well as an incoherent light source. The major advantages of this proposed architecture are that it alleviates the drawbacks of low resolution and poor dynamic range of the existing SLMs. To further increase the error-correction ability, an orthogonal projection (OP) algorithm is introduced. Experimental and computer simulated demonstrations for image reconstruction are provided.

II. HOPFIELD MODEL

A model to describe the collective behavior of the neural network, based on the associative process of the human brain, has been introduced by Hopfield [4]. His model consists of a set of interconnected neurons that operates in a binary state. The output from each neuron is assumed dependent on the output from the neighboring neurons, in which the operation can be described by the following iterative formula:

$$V_i(n+1) = f(v_i(n)) \quad v_i(n) = \sum_{j=1}^N T_{ij} V_j(n) \quad (1)$$

where $f(\cdot)$ represents the threshold operation, i.e.,

$$f(x) = \begin{cases} 1 & x \geq 0 \\ -1 & x < 0 \end{cases} \quad (2)$$

T_{ij} is the strength (i.e., weight factor) of connection between i th and j th neurons, $V_j(n)$ is the input value to j th neuron, N represents the total number of neurons in the network, and n denotes the number of iterative operations.

The Hopfield model begins by storing a set of input-output vector pairs $(U^{(m)}, V^{(m)})$, $m = 1, 2, \dots, M$, in a neural network with the aid of reorganized connections, where vectors $U^{(m)}$ and $V^{(m)}$ are N bits long, corresponding to the number of neurons in the network. Thus the storage prescription can be expressed by a collection of outer-product vectors, as given by

$$T_{ij} = \begin{cases} \sum_{m=1}^M (2V_i^{(m)} - 1)(2U_j^{(m)} - 1) & i \neq j \\ 0 & i = j \end{cases} \quad (3)$$

In the case of identical input-output vector pair $(V^{(m)}, V^{(m)})$, T_{ij} can be used to retrieve the stored vector from an incomplete or partially erroneous input V' . The thresholded product vector can be written as

$$V_i = f\left(\sum_{j=1}^N T_{ij} V'_j\right) \quad (4)$$

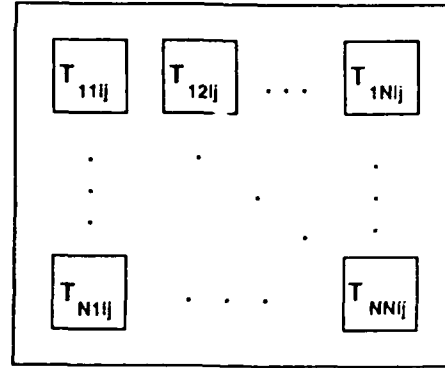


Figure 1 Partition of a 4-D weight matrix T_{ikl} into an array of 2-D submatrices T_{11ij} , T_{12ij} , ..., and T_{NNij} .

Notice that Eq. (4) can be used to estimate the target vector V similar to the input vector V' , for which we have used the Hamming distance as a criterion. If the output vector is fed back, a more accurate vector may be obtained; we have assumed that the iteration would converge to the correct vector for a stable network.

Similarly, for a 2-D neural network of $N \times N$ neurons, the Hopfield model can be written as

$$V_{ik}(n+1) = f(v_{ik}) \quad v_{ik} = \sum_{i=1}^N \sum_{j=1}^N T_{ikij} V_{ij}(n) \quad (5)$$

where V_{ik} and V_{ij} represent $N \times N$ 2-D vectors and T_{ikij} is an $N^2 \times N^2$ 4-D IWM [1]. Matrix T can be partitioned into an array of 2-D submatrices, in which each submatrix is an $N \times N$ array, as depicted in Figure 1. Thus a 4-D IWM can be represented by an array of 2-D submatrices.

III. AN ADAPTIVE OPTICAL NEURAL NETWORK

In a 2-D $N \times N$ neural network, the IWM requires an SLM of N^4 elements with multiple gray levels. However, such SLMs are not quite available at present time.

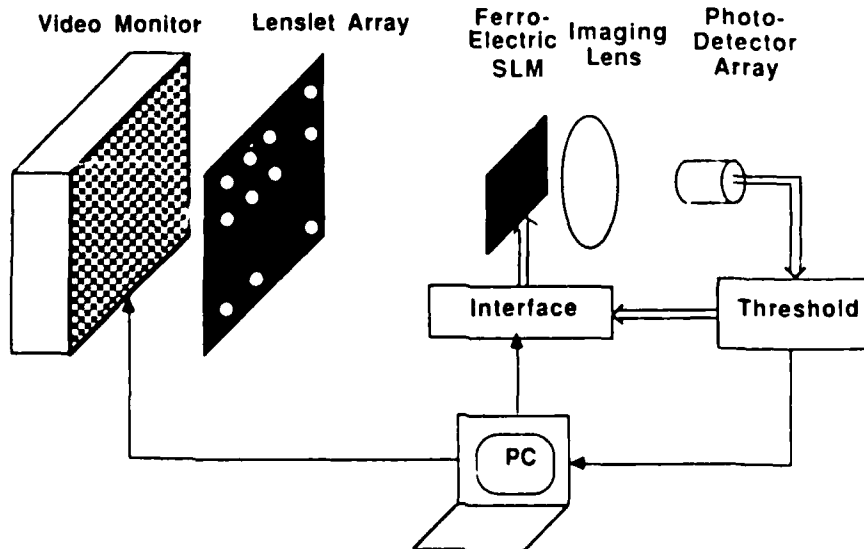


Figure 2 Schematic diagram of an adaptive optical neural network

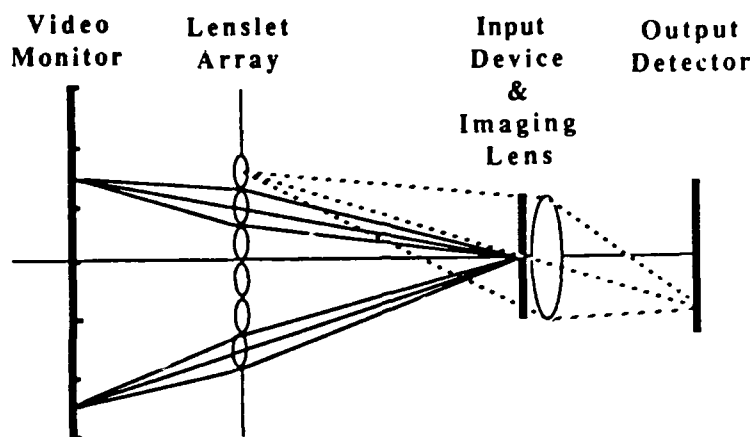


Figure 3 Side view of the optical neural network

We shall now propose an adaptive optical neural network in which a high resolution video monitor is used to display the interconnection weight matrix T and at the same time to provide the light source for the processing operation, as sketched in Figure 2. Notice that the proposed system differs from the matrix-vector processor of Farhat and Psaltis [1] in that the locations of input array and weighting matrix mask are interchanged. This arrangement makes it possible to use a video monitor as the IWM instead of using a low resolution, poor dynamic range SLM. A lenslet array consisting of $N \times N$ small lenses is used to establish the optical interconnections and a moderate sized programmable SLM with $N \times N$ binary pixels is used as the input device. As illustrated in Figure 3, the light beam emitted from each block of the TV screen passes through a specific lens of the lenslet array and is imaged onto the input device (i.e., SLM). The light field behind the SLM is then imaged onto the output plane by a imaging lens that can be picked up by a photodetector array (i.e., CCD). Thus it forms an $N \times N$ output array, which represents the product of the 4-D matrix T and the 2-D input array.

To construct a closed loop neural network, the output signals from the detector array are fed back to the input SLM via a thresholding circuit. By programming the interconnection weight matrix with a computer, the optical neural network can be made adaptive.

A ferroelectric SLM would be a satisfactory input device of the system, since its contrast ratio is as high as 500:1. Moreover, the SLM is parallel addressable—the detector array and the input array can communicate in parallel. Thus the whole electrooptical feedback loop can be established in a completely parallel fashion. This arrangement allows the system to work at a high speed and in an asynchronous mode. Although the interconnection weight matrix (i.e., the video monitor) works at a relatively low speed, it is however not required for the programming speed to match the iteration speed in the loop. Video monitors with 256 gray levels and 1024×1024 pixels are commercially available. Based on this data, one may build a hybrid optical neural network of 32×32 (i.e., 1024) neurons using the commercially available video monitor.

IV. EXPERIMENTAL DEMONSTRATIONS

To show the feasibility of the proposed architecture, an optical neural network with 8×8 (i.e., 64) neurons has been built

using a Panasonic black and white video monitor of 384×512 pixels as the weight matrix. A Seiko liquid crystal TV (LCTV) is used as the real-time input device in the system. An 8×8 lenslet array is constructed to provide the interconnections between the memory matrix and the input object. The output signals are picked up by a CCD array detector and then sent to a microcomputer for the thresholding operation. A Data-Cube AT-428 image capture and display module is used to provide the interfacing between the microcomputer, CCD, LCTV and video monitor.

Figure 4 illustrates an image reconstruction process using the optical neural network described. With reference to the Hopfield model [i.e., Eq. (3)], three capital letters "A", "B", and "X" are stored in the interconnection weight matrix T . Each of these letters occupies a 8×8 array pixels, as shown in Figure 4(a). In our experiments, the positive and the negative parts of T are sequentially displayed on the video monitor, as shown in Figures 4(b) and (c), respectively. An imperfect object of letter "X" is applied at the input SLM, as shown at the left side of Figure 4(d). By sequentially displaying the positive and the negative parts of T onto the video monitor, the output images are captured by the CCD camera, which is then sent to the microcomputer for subtraction and thresholding operations. Thus, a recovered pattern can be obtained, as shown in the right side of Figure 4(d). Needless to say, the positive and negative parts of T can be added with a bias level to avoid the negative quantity and a single step operation can be achieved by thresholding the output signals.

V. ORTHOGONAL PROJECTION (OP) ALGORITHM

Although the error-correction ability of the Hopfield model is rather effective, its correction ability decreases rapidly as the number of stored patterns increases. In order to obtain the desired results, the number of stored vectors M in the Hopfield model must be sufficiently smaller as compared with the number of neurons N , i.e., $M < N/4 \ln N$, as pointed out by Farhat et al. [3], and each stored vector should also be independent. However, in practice, the stored vectors are generally not independent; this may produce some ambiguous results. In computer simulation, we have used an orthogonal projection algorithm to improve the error-correction ability of the Hopfield model. The OP algorithm is described in the following:

Consider an N -dimensional vector space, in which there are M vectors $V^{(m)}$, $m = 1, 2, \dots, M$, of N bits in length.

This set of vectors $\{V^{(m)}\}$ will construct a weight matrix T . The basic concept about the OP algorithm is to project each vector $V^{(m_0)}$ in the vector set $\{V^{(m)}\}$ to the orthogonal subspace spanned by the column vectors $V^{(m)}$, $m = 1, 2, \dots, m_0 - 1$. The orthogonal projection vector can be obtained from a Gram-Schmidt orthogonalization procedure [11], such as

$$V^{o(m_0)} = V^{(m_0)} - \sum_{m=1}^{m_0-1} \frac{(V^{(m)}, V^{(m_0)})}{\|V^{(m)}\|} V^{(m)} \quad (6)$$

where $(V^{(m)}, V^{(m_0)})$ denotes the inner product of two vectors $V^{(m)}$ and $V^{(m_0)}$, and $\|V^{(m)}\|$ is the quadratic vector norm of $V^{(m)}$.

For a given matrix $T^{(m-1)}$, the recursive algorithm for the associative memory matrix $T^{(m)}$ can be expressed as

$$T^{(m)} = \begin{cases} T^{(m-1)} + (U^{(m)} - T^{(m-1)}V^{(m)}) \frac{V^{o(m)T}}{\|V^{o(m)}\|} & \text{for } \|V^{o(m)}\| \neq 0 \\ T^{(m-1)} & \text{otherwise} \end{cases} \quad (7)$$

where $U^{(m)}$ stands for the desired output vector. The initial memory matrix $T^{(0)}$ can be either a zero or an identity matrix.

Using the OP algorithm as described, computer simulations have been conducted and the results obtained are shown in Figure 5. Four letters, "A", "B", "W," and "X" are used as the reference patterns, as shown in Figure 5(a). By applying Eqs. (6) and (7), the weight matrix T is constructed. Figures 5(b) and (c) illustrate the reconstruction of the letter "X" from a partial image, by using the OP algorithm and the Hopfield model, respectively. The input pattern is a small portion of pattern X, which is displayed on the left side of Figures 5(b) and (c), respectively. The successive patterns, as displayed in these figures, represent the output of successive iterations. Under the same conditions, the OP algorithm is more robust and has a higher convergent speed than the Hopfield model, as can be seen in these figures. In this example, the OP algorithm requires only one iteration [see Figure 5(a)], while the Hopfield model converges after three iterations [see Figure 5(b)].

VI. DISCUSSION

The advantages of using a video monitor as the memory matrix are its high resolution (e.g., 1024×1024 pixels), large dynamic range (about 256 gray levels), and low cost. A further

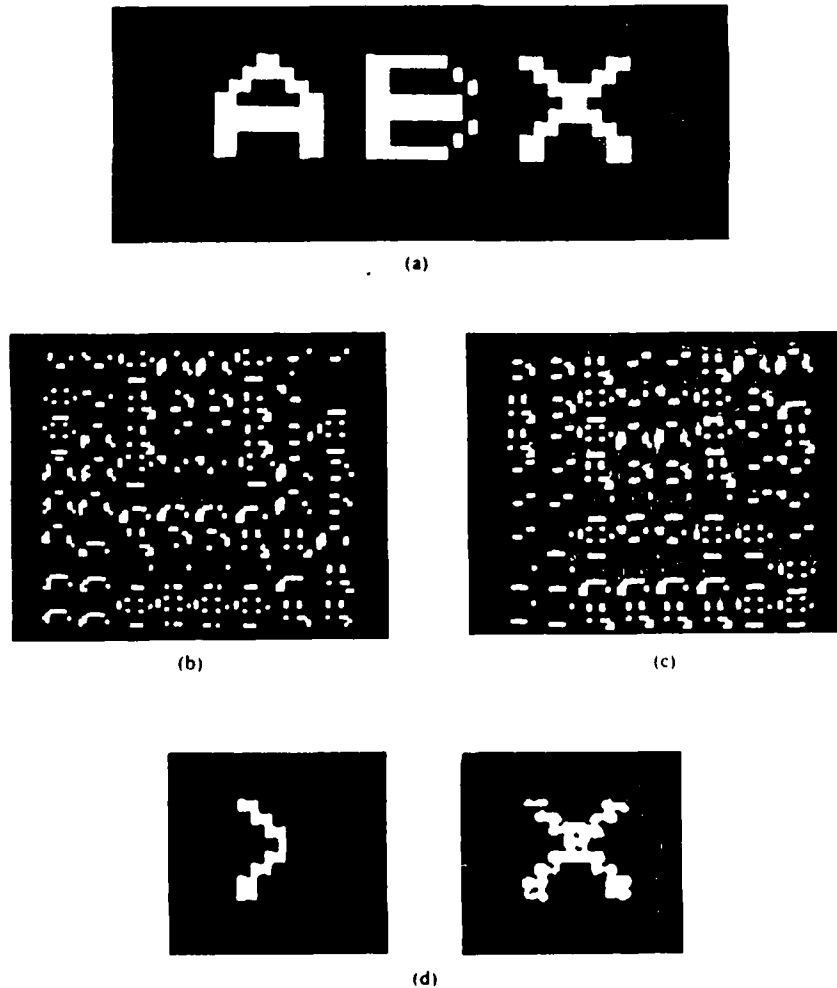
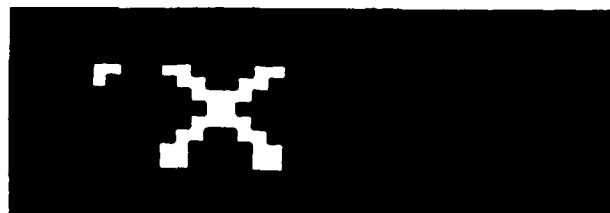


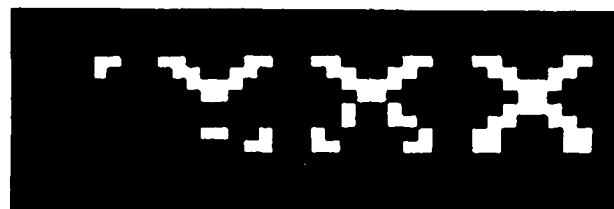
Figure 4 Experimental result of an image reconstruction process. (a) Three capital letters to be stored in the weight matrix. (b) and (c) Positive and negative weight matrix of Hopfield model. (d) Reconstruction of pattern X by using the optical neural network.



(a)



(b)



(c)

Figure 5 (a) Four letters to be stored in the weight matrix. (b) and (c) Reconstruction of pattern A by using both the OP algorithm and the Hopfield model, respectively

development of high-definition TV technology would enable us to build an even larger neural network with higher speed. Currently, integrated optics technology may provide us with a microlens array containing 30,000 interconnections on a glass substrate [14]. Given the addressing time of the ferroelectric SLM on the order of 10^{-5} s and TV frame rate of 30 frames per second, the operation speed of the proposed system, with $1024 \times 1024 = 1.05 \times 10^{11}$ interconnection operations per second, and the learning process would have a speed of $30 \times 1024 \times 1024 = 3.146 \times 10^7$ operations per second.

Notice that modifications of the Hopfield model, such as the orthogonal projection and the multilevel recognition algorithms have been applied in the proposed system. This proposed neural network can also be used to implement multilayer self-learning algorithms and high-order neural networks, as will be discussed in our forthcoming papers.

ACKNOWLEDGMENT

We acknowledge support by the U.S. Air Force, Rome Air Development Center, Hanscom Air Force Base, MA, under contract F19628-87-C-0086.

REFERENCES

1. N. H. Farhat and D. Psaltis, "Optical Implementation of Associative Memory Based on Models of Neural Networks," *Optical Signal Processing*, J. L. Horner, ed., Academic, New York, 1987, pp. 129-162.
2. D. Psaltis, J. Yu, X. G. Gu, and H. Lee, "Optical Neural Nets Implemented with Volume Holograms," *Optical Computing, Tech Digest Series*, Vol. 11, 1987, p. 129.
3. N. H. Farhat, D. Psaltis, A. Prata, and E. Pack, "Optical Implementation of the Hopfield Model," *Appl. Opt.*, Vol. 24, No. 10, 1985, p. 1469.
4. J. J. Hopfield, "Neural Network and Physical System with Emergent Collective Computational Abilities," *Proc. Natl. Acad. Sci. USA*, Vol. 79, 1982, p. 2554.
5. M. Takeda and J. W. Goodman, "Neural Networks for Computation: Number Representations and Programming Complexity," *Appl. Opt.*, Vol. 25, No. 18, 1986, p. 3033.
6. R. A. Athale, H. H. Szu, and C. B. Friedlander, "Optical Implementation of Associative Memory with Controlled Nonlinearity in the Correlation Domain," *Opt. Lett.*, Vol. 11, No. 7, 1986, p. 482.
7. P. Lalanne, J. Taboury, J. C. Saget, and P. Chavel, "An Extension of the Hopfield Model Suitable for Optical Implementation," *Proc. SPIE*, Vol. 813, 1987, p. 27.
8. A. D. Fisher and J. N. Lee, "Optical Associative Processing Elements with Versatile Adaptive Learning Capabilities," *Optical Computing, Tech. Digest Series*, Vol. 11, 1987, p. 137.
9. J. Jang, S. Jung, S. Lee, and S. Shin, "Optical Implementation of the Hopfield Model for Two-Dimensional Associative Memory," *Opt. Lett.*, Vol. 13, No. 3, 1988, p. 248.
10. B. Macukow and H. H. Arsenault, "Optical Associative Memory Model Based on Neural Networks Having Variable Interconnection Weights," *Appl. Opt.*, Vol. 26, No. 5, 1987, p. 924.

11. G. H. Golub and C. F. Van Loan, *Matrix Computation*, Johns Hopkins, Baltimore, 1983.
12. G. Eichmann and M. Stojancic, "Superresolving Signal and Image Restoration Using a Linear Associative Memory," *Appl. Opt.*, Vol. 26, No. 10, 1987, p. 1911.
13. R. Hecht-Nielsen, "Performance Limits of Optical, Electro-Optical, and Electronic Neurocomputers," *Optical and Hybrid Computing*, H. H. Szu, ed., SPIE, Vol. 634, 1986, p. 277.
14. M. Veldkamp, "Amacronic Sensors," *Tech. Digest of International Neural Network First Annual Meeting*, 1988.

Received 4-19-89

Microwave and Optical Technology Letters, 2/7, 252-257
 © 1989 John Wiley & Sons, Inc.
 CCC 0895-2477/89/\$4.00

A SIMPLE MODEL OF THICK STRIPS IN ANISOTROPIC MULTILAYERED DIELECTRIC MEDIA*

G. Plaza, R. Marqués, and M. Horno
 Departamento de Electrónica y Electromagnetismo
 Facultad de Física
 Universidad de Sevilla
 41012-Sevilla, Spain

KEY TERMS

Thick microstrip, anisotropic dielectric, multilayer, MIC, MMIC

ABSTRACT

A theoretical model is presented for the analysis of microstrip multiconductor structures embedded in anisotropic lossless nonmagnetic multilayered dielectric media with finite strip thickness. The model reduces the thick conductor problem to the thin strip case. Calculations are made in the spectral domain. Numerical results are given and compared with published data.

1. INTRODUCTION

The TEM transmission-line properties of a microstrip on anisotropic lossless nonmagnetic multilayered substrates can be characterized by three parameters: the capacitance C , the capacitance without the substrate C_0 , and the series resistance R . The solutions for C and C_0 are usually obtained by supposing that the strip is infinitely thin. However, strip thickness may have an important influence on the values of C and C_0 , especially in MMICs and MICs using thick film technology. Also, the thickness of metallizations must be taken into account to determine the series resistance R by using the incremental-inductance rule [1].

Several general methods are currently available to solve the problem of the thick strip on multilayered substrate, such as the finite-element method [2], the network analog approach [3], and the finite difference method [4]. In spite of their generality, these methods involve, in many cases, an extremely large computation time and so they may not be suitable to be put into a more general design or analysis program. There are also other useful methods when simple substrates are to be considered. These methods can be divided into two general

types: the integral equation methods [5, 6] and the approximate conformal mapping techniques [7]. For a more general structure including anisotropic and multilayered dielectric media, it may be rather difficult to apply these methods even if strip thickness is neglected. In this paper, we present a new model to study the influence of metallization thickness on the characteristic parameters of planar transmission lines. This model is applied to the analysis of a single microstrip on an anisotropic lossless nonmagnetic multilayered substrate.

II. THE M-STRIPS MODEL

Figure 1(a) shows the cross section of the generic subject line and Figure 1(b) shows the model suggested. In this model, the thick strip has been removed and replaced by a set of M infinitely thin strips; the charge is allowed to flow among them until the strips reach the same potential.

These structures are equivalent when the number of strips M goes to infinity. When M is a finite number, the electric energy of both, the real structure and the model, is only similar. Dealing with this model we can use the methods previously developed to compute the transmission-line parameters when the thickness of metallization is neglected (thin strip case).

II.1. Method of Analysis

a. *Variational algorithm.* In the spectral domain, the electric energy per unit length of the structure shown in Figure 1(b), can be expressed as a function of the charge densities on the conductors as

$$U = \frac{1}{4\pi} \sum_{i=1}^M \sum_{j=1}^M \int_{-\infty}^{\infty} q_i^*(\beta) G_{ij}(\beta) q_j(\beta) d\beta \quad (1)$$

where $q_i(\beta)$ is the Fourier transform of the charge density on the i th strip $q_i(x)$ and $G_{ij}(\beta)$ is the Fourier transform of the Green's function $G(x, x'; y_i, y'_j)$, where $x' = 0$ and y_i, y'_j the coordinates of the i th and j th strips, respectively.

The expression given in (1) for energy is variational. The equivalence between the energy of the real and the model structure when M goes to infinity is guaranteed by the additional condition

$$\sum_{i=1}^M \int_{-a/2}^{a/2} q_i(x) dx = 1 \quad (2)$$

The total charge on the strips is $Q = 1$.

The charge distribution on each strip is now represented by a set of functions in the following way:

$$q_i(x) = \sum_{k=0}^{N_i} a_k^i \Gamma_k^i(x) \quad (3)$$

where $\Gamma_k^i(x)$ are the trial functions and a_k^i are variational coefficients to be computed.

A mathematical requirement is now imposed on the trial functions in order to simplify the problem:

$$\int_{-a/2}^{a/2} \Gamma_k^i(x) dx = \delta_{ik} \quad (4)$$

*This work was supported by the Conserjería de Educación y Ciencia de la Junta de Andalucía, Spain.

Two-dimensional programmable optical neural network

Taiwei Lu, Shudong Wu, Xin Xu, and Francis T. S. Yu

A 2-D hybrid optical neural network using a high resolution video monitor as a programmable associative memory is proposed. Experiments and computer simulations of the system have been conducted. The high resolution and large dynamic range of the video monitor enable us to implement a hybrid neural network with more neurons and more accurate operation. The system operates in a high speed asynchronous mode due to the parallel feedback loop. The programmability of the system permits the use of orthogonal projection and multilevel recognition algorithms to increase the robustness and storage capacity of the network.

I. Introduction

In recent years attention has been paid to problems concerning the optical implementation of neural networks.¹⁻¹⁰ A 2-D optical neural network has been synthesized by Farhat and Psaltis, for which they used the basic concept of vector-matrix optical processing.¹ This optical neural network is composed of a linear array of LEDs as an input device, which is interconnected to a weighting mask by a lenslet array. To provide the network with self-organization and learning capabilities, a programmable spatial light modulator (SLM) with fine resolution and a large number of distinguishable grey levels is needed as a weighting mask. However, the currently available SLMs generally have very limited space-bandwidth products, fewer grey levels, and high cost, which make it difficult to implement such an optical neural network.

In this paper, we propose an optical architecture in which a high resolution video monitor is used to display the interconnection weight matrix (IWM). The video monitor also provides the incoherent light source for processing. This proposed optical neural network alleviates the low resolution and limited dynamic range problem for generating the IWM encountered in previous investigations. To increase further the error correction and system storage capacities, orthogonal projection (OP) and multilevel recognition (MR) algo-

rithms are used. Experiments and computer simulations of pattern reconstruction using the proposed optical neural network are provided.

II. Description of the Hopfield Model

Based on the process of association by which the human brain stores information, various models have been introduced to describe the collective behavior of a neural network. Among them, the Hopfield model¹¹ is a single layer neural network with an outer product learning algorithm, which can also be found in the earlier literature.^{12,13}

The Hopfield model consists of a set of neurons which are mutually interconnected. He assumed that each neuron operates in a binary state. The output from each neuron depends on the output of the neighboring neurons. With this assumption, the operation of a neuron can be described by an iterative formula, as given by

$$V_i(n+1) = f\{v_i(n)\}, \quad v_i(n) = \sum_{j=1}^N T_{ij} V_j(n), \quad (1)$$

where $f(\cdot)$ represents the threshold operation, namely,

$$f(x) = \begin{cases} 1, & x \geq 0, \\ -1, & x < 0. \end{cases} \quad (2)$$

In Eq. (1), T_{ij} is the strength or the weight factor of the connection between the i th and j th neurons, and $V_j(n)$ is the input value to the j th neuron for the n th iteration, N represents the number of neurons in the network, and n denotes the number of iterative operations.

Note that the Hopfield model begins by storing a set of input-output vector pairs $\{U^{(m)}, V^{(m)}\}$, $m = 1, 2, \dots, M$ in a neural network with the aid of reorganized connections. Vectors $U^{(m)}$ and $V^{(m)}$ are N bits long, which equals the number of neurons N in the network. The storage prescription can be expressed by a collection of outer product vectors, such as

The authors are with Pennsylvania State University, Department of Electrical Engineering, University Park, Pennsylvania 16802.
Received 31 October 1988.
0003-6935/89/224908-06\$02.00/0.
© 1989 Optical Society of America.

$$T_{ij} = \begin{cases} \sum_{m=1}^M [2V_i^{(m)} - 1](2U_j^{(m)} - 1), & i \neq j, \\ 0, & i = j. \end{cases} \quad (3)$$

In the case of an identical input-output vector pair $[V^{(m)}, V^{(m)}]$, T_{ij} may be used to retrieve the stored information about a certain vector V' , which is incomplete or partially erroneous. The thresholded product vector can be written as

$$v_i = f\left(\sum_{j=1}^N T_{ij} V_j\right). \quad (4)$$

This relationship estimates the target vector V that is most similar to the input vector V' . The Hamming distance is used as a measure of their similarity. If the output vector is used as the next input vector (i.e., first iteration), the new output vector would be closer to the stored vector, where we assume that the iteration would converge to the correct vector in a stable network.

For a 2-D neural network with $N \times N$ neurons, the Hopfield model can be extended to the following form:

$$V_{ik}(n+1) = f(v_{ik}), \quad v_{ik} = \sum_{i=1}^N \sum_{j=1}^N T_{ikij} V_{ij}(n), \quad (5)$$

where V_{ik} and V_{ij} represent 2-D vectors (i.e., patterns) and T_{ikij} is a 4-D interconnection weight matrix.¹

We note that matrix T can be partitioned into an array of $N \times N$ submatrices, and each submatrix has an $N \times N$ size, as depicted in Fig. 1. Thus we see that a 4-D memory matrix can be easily extended by arrays of 2-D submatrices.

III. Hybrid Optical Neural Network

The major difficulty in implementing 2-D neural networks is the actual construction of the weighting matrix T using real time SLMs. For an $N \times N$ neural network, the weighting matrix requires an SLM of N^4 elements with several grey levels. However, the currently available SLMs provide poor resolution and a limited number of grey levels, which limit the processing capacity of the neural network.

We propose a programmable optical neural network in which a high resolution video monitor is used to display the IWM,¹⁴ as shown in Fig. 2. This proposed system differs from the matrix-vector processor of Farhat and Psaltis, in which the positions of the input SLM and IWM have been exchanged. We note that this arrangement makes it possible to use a video monitor for associative memory matrix generation instead of a low resolution and low contrast SLM. Again a lenslet array consisting of $N \times N$ small lenses is used to establish the optical interconnections between the IWM and input patterns, where a moderate sized SLM with $N \times N$ binary pixels serves as the input device. As depicted in Fig. 3, the light beam emitted for each submatrix from the video screen would be imaged by a specific lens of the lenslet array onto the input SLM. Thus $N \times N$ submatrices would be added to the input device. The overall transmitted light can be imaged at

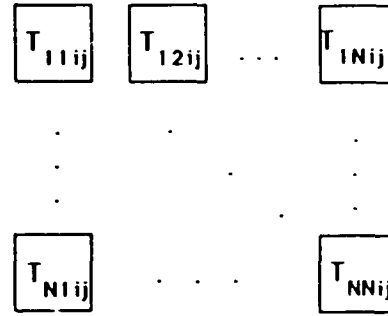


Fig. 1. Partition of a 4-D matrix T_{klij} into an array of 2-D submatrices T_{11ij} , T_{12ij} , ..., and T_{NNij} .

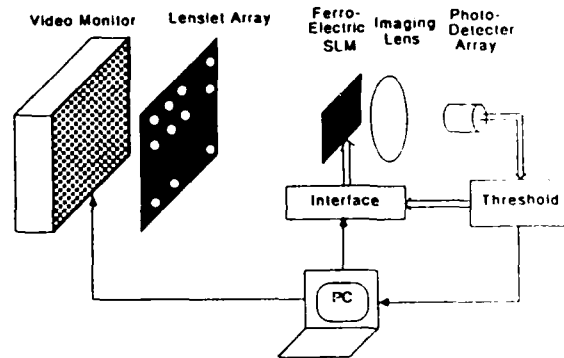


Fig. 2. Schematic diagram of a hybrid optical neural network.

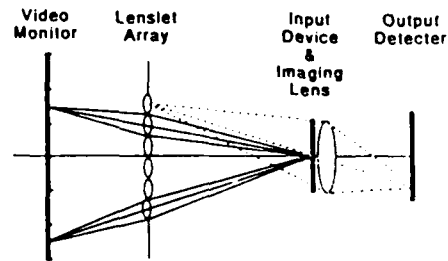


Fig. 3. Optical arrangement of the neural network.

the output plane to form an $N \times N$ output array, which represents the product of the 4-D matrix and the 2-D input pattern. Needless to say, the output pattern can be picked up by an $N \times N$ photodetector array for thresholding and feedback iterations.

To form a closed loop neural network operation, the output signals from the detector array are fed back to the input SLM via a thresholding circuit. It is apparent, by the intervention of a computer, that the proposed optical neural network can be made adaptive.

We propose that a ferroelectric liquid crystal SLM be used as the input device of the system. Accordingly, its contrast ratio can be as high as 125:1.^{15,17} Since the SLM can be addressed in parallel, the detector and input arrays can communicate in parallel. Thus the electrooptic feedback loop can be performed in a com-

pletely parallel manner. This arrangement would allow the system to operate in a high speed asynchronous mode. Thus the sequential electronic bottleneck can be alleviated to some extent with the feedback loop. Although displaying memory matrices using a video monitor is relatively slow, the programming speed of the IWM is not required to match the iteration speed in the feedback loop. Accordingly, 1024×1024 -pixel video monitors are available commercially, for which it is possible to build a hybrid optical neural network with 32×32 (i.e., 1024) neurons.

The resolution requirement of the lenslet array is modest. An array of 32×32 lenses, each with a diameter of 2.5 mm, can provide at least 10 times the resolution of a commercial TV monitor, which has a resolution of ~ 3 lines/mm.

However, alignment of the optical system is rather critical for the matrix-vector operations. The submatrices on the TV screen must be precisely imaged onto the input SLM by the lenslet array in a superimposing position. Since the proposed optical neural network is essentially a closed-loop feedback system, the precise alignment can be corrected by adjusting the position of each submatrix on the TV screen using the computer. The intensity of the TV screen can also be adjusted. Thus the proposed optical system can indeed perform in an adaptive mode.

IV. Experimental Demonstrations

To demonstrate the feasibility of the proposed architecture, a 2-D optical neural network with 8×8 (i.e., 64) neurons has been built. The experimental setup is shown in Fig. 4. A Sony video monitor of 384×512 pixels is used to generate the associative memory matrix. An 8×8 lenslet array ($f = 125$ mm, $\phi = 15$ mm) that provides the interconnections between the memory matrix and input SLM is constructed. The output signals are picked up by a Fairchild CCD camera and then sent to a microcomputer for thresholding operation. A Data-Cube AT-428 image capture with a display module is used to provide the interfacing among the microcomputer, input SLM, CCD detector, and TV monitor. We have used a transparency instead of a ferroelectric SLM for the preliminary experimental demonstrations. Note that a Seiko liquid crystal television (LCTV) built with thin film transistor (TFT) technology has also been used as a real time input SLM in our later experiments.

Figure 5 illustrates an image reconstruction process based on the system described above. With reference to the Hopfield model [i.e., Eq. (3)], four letters, A, B, W, and X, are stored in the memory matrix T . Each letter occupies an 8×8 array pixel, as shown in Fig. 5(a). The positive and negative parts of the memory matrix T are shown in Figs. 5(b) and (c), respectively. As depicted in Fig. 5(d), an imperfect image of A is fed to the input SLM of the system [see the leftmost pattern in Fig. 5(d)]. The positive and negative parts of the memory matrix are sequentially displayed on the video monitor using the microcomputer. The positive and negative output images are picked by the CCD



Fig. 4. Experimental setup. Left to right: TV monitor, 8×8 lenslet array, LCTV, imaging lens, and CCD camera.

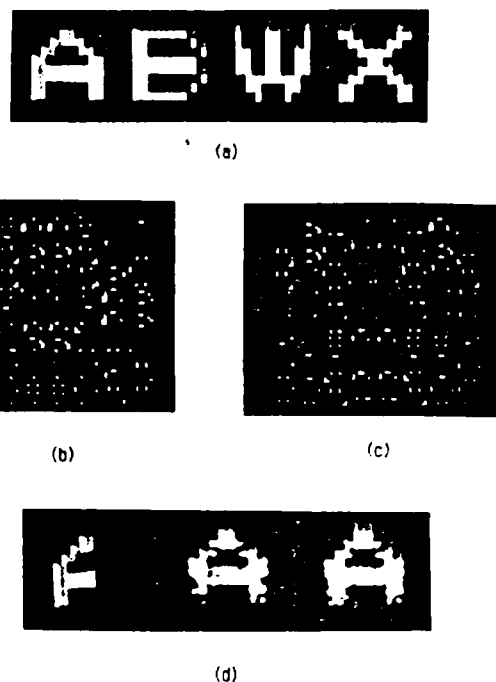


Fig. 5. Experimental result of an image reconstruction process: (a) four capital letters stored in the memory mask; (b), (c) positive and negative memory masks of the Hopfield model; (d) reconstruction of pattern A by using the optical neural network.

camera and then sent to the microcomputer for subtraction and thresholding operations. Thus a partially recovered pattern is obtained at the output end, as shown in the middle of Fig. 5(d). Since the output pattern is not quite complete, this pattern is fed back to the input SLM for another iteration, a more completely recovered pattern can be found at the output plane, which is depicted on the right-hand side of Fig. 5(d). Needless to say, the positive and negative parts of T can be added with a bias level to avoid the negative quantity, in which a single step operation can be achieved by properly thresholding the output signals.

V. Orthogonal Projection Algorithm

The error correction ability of the Hopfield model is effective with the assumption that the stored vectors are significantly different. The correction ability decreases rather rapidly as the number of stored patterns increases. To obtain the desired results, the number of stored vectors M in the Hopfield model should be sufficiently smaller than the number of neurons in the network, as pointed out by Farhat *et al.*,² i.e., $M < N/4 \ln N$. However, in practice, the stored vectors are generally not independent, and some ambiguous output results.

We note that orthogonization techniques have been used in associative memory and digital image processing.^{12,15} In this section, we use the orthogonal projection (OP) algorithm to improve the error correction ability of the optical neural network.

The OP algorithm can be described as follows:

Let us consider an N -dimensional vector space consisting of a set of M vectors $V^{(m)}$, which will be used to construct an interconnection weight matrix T . The basic concept of the OP algorithm is to project each vector $V^{(m_0)}$ within the vector set $\{V^{(m)}\}$ onto the orthogonal subspace spanned by the independent vectors $V^{*(m)}$, $m = 1, 2, \dots, m_0 - 1$. The orthogonal projection vector can be described by the Gram-Schmidt orthogonalization procedure,¹⁸ such as

$$V^{*(m_0)} = V^{(m_0)} - \sum_{m=1}^{m_0-1} \frac{[V^{(m)}, V^{*(m)}]}{\|V^{*(m)}\|} V^{*(m)}, \quad (6)$$

where $[V^{(m)}, V^{*(m)}]$ denotes the inner product, and $\|V^{*(m)}\|$ is the norm of $V^{*(m)}$.

Hence, for a given matrix $T^{(m-1)}$, the recursive algorithm for the associative memory matrix $T^{(m)}$ can be expressed as

$$T^{(m)} = \begin{cases} T^{(m-1)} + [U^{(m)} - T^{(m-1)}V^{(m)}] \frac{V^{*(m)T}}{\|V^{*(m)}\|}, & \text{for } \|V^{*(m)}\| \neq 0, \\ T^{(m-1)}, & \text{otherwise,} \end{cases} \quad (7)$$

where $U^{(m)}$ stands for the desired output vector, and the initial memory matrix $T^{(0)}$ can be either a zero or an identity matrix.

Using the OP algorithm described above, computer simulations of the proposed optical neural network have been conducted, and the result is in Fig. 6. Note that four capital letters, as in Fig. 5(a), are used for the reference patterns. By applying Eqs. (6) and (7), the associative memory matrix T is constructed, for which the positive and negative parts of T are shown in Figs. 6(a) and (b). The reconstruction of a partial pattern of letter A by using the OP algorithm and Hopfield model is shown in Figs. 6(c) and (d), respectively. The successive patterns in these figures represent the successive iterations. Thus we see that the OP algorithm is generally more robust and has a higher convergent speed compared with the Hopfield model. Furthermore, in this example the OP algorithm requires only two iterative operations to obtain the correct re-

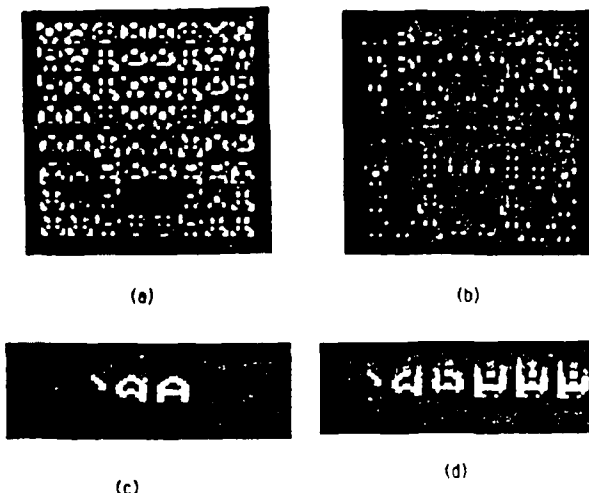


Fig. 6. (a), (b) Positive and negative memory masks of the OP algorithm. (c) Reconstruction of pattern A by using both the OP algorithm and Hopfield model, respectively.

sult [Fig. 6(c)]. In contrast, the Hopfield model converges into a local minima, which gives an incorrect result [Fig. 6(d)].

A numerical analysis of the robustness of an 8×8 -neuron single layer neural network is evaluated. Twenty-six capital English letters are used as the reference patterns, each occupying an 8×8 -pixel array. The average Hamming distance of the reference patterns is ~ 26 pixels, and the minimum distance is 4 pixels. We assume that the input patterns are embedded in random noise, where the input SNRs are chosen to be ~ 5 dB (i.e., 50% noise), 7 dB (i.e., 33% noise), and 10 dB (i.e., 10% noise), respectively. Figure 7 represents the output error pixels against the number of stored patterns for various values of an input SNR. From this figure, we see that using the Hopfield model the neural network becomes unstable after storing five reference patterns. However, using the OP algorithm, the neural network can retrieve all the letters with 50% input noise for twenty-six stored letters. We also note that the error correction ability decreases substantially as input noise and the number of stored patterns increase. Nevertheless, the OP algorithm generally provides better error correction capability.

VI. Multilevel Recognition Algorithm

For the case of an ill-conditioned weight matrix, the Hamming distances between the stored vectors are very short, which may result in the Hopfield model in incorrect results. For example, four capital English letters, T, I, O, and G, are stored in the associative memory matrix, as shown in Fig. 8(a). Although the input pattern is a partial letter G, the Hopfield neural network failed to reproduce the pattern for which the output result falls into a local minima, as shown in Fig. 8(b). We note that, in some cases, the output would not converge to a correct result, even when the input is exactly the same as one of the reference patterns. In

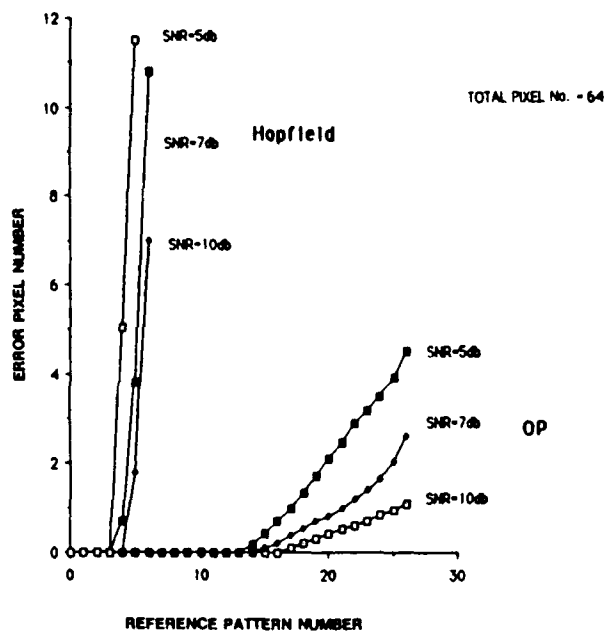


Fig. 7. Performance of the Hopfield and OP models.



Fig. 8. (a) Four letters stored in the memory mask. (b) Reconstruction of G by using the Hopfield model.

other words, the Hopfield model is effective only in dealing with independent patterns.

From the above example we see that the smaller the Hamming distances among the stored patterns, the less the error correction ability. However, it is also known that the less information stored in the memory, the more effectively the neural network can correct the error. Using the advantages of the programmability of the proposed optical neural network, a multilevel recognition (MR) algorithm is developed. This algorithm adopts the tree search strategy that increases the error correction ability by reducing the number of vectors stored in each memory matrix.¹⁹ The MR algorithm first classifies the reference patterns into subgroups and then develops a tree structure according to the similarity (i.e., Hamming distance) of the reference patterns. A smaller number of reference patterns can be stored in the memory matrix built for each subgroup. The MR algorithm then changes the memory matrices with reference to the Hamming distances between the intermediate result and the patterns in different subgroups. In this manner, the storage capacity is not limited by the size of the neural network. However, the trade-off is that the processing speed is slowed down due to changes in the memory matrices.

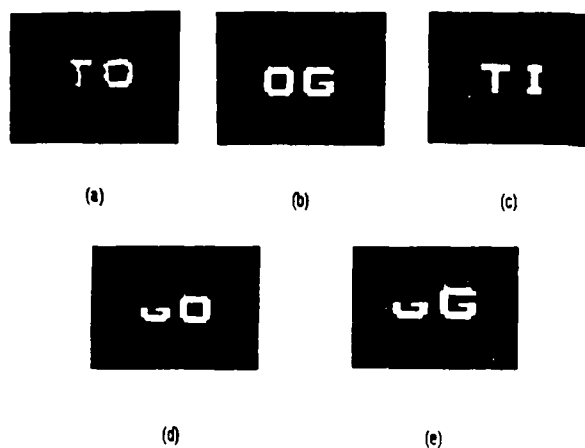


Fig. 9. Three subgroups of letters used in the MR algorithm. (b), (c) Reconstruction of G by T_O and T_{OG} , respectively.

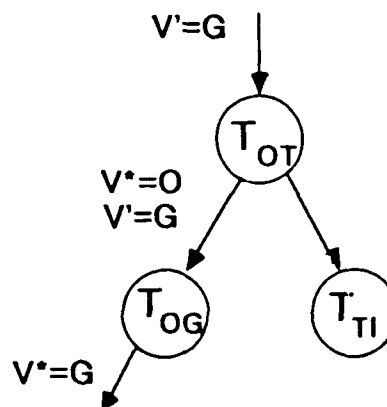


Fig. 10. Flow chart diagram of the MR algorithm.

As an example, we consider once more the four letters shown in Fig. 8(a). According to the similarity of the patterns, the above four letters can be classified into two groups, namely, [O,G] and [T,I]. T and O are arbitrarily selected from these two subgroups to form a root group [T,O], as shown in Figs. 9(a), (b), and (c), respectively. Instead of constructing an associative memory matrix T_{TIOG} , three submemory matrices, T_{TO} , T_{OG} , and T_{TI} , are composed and stored in the microcomputer. In the first demonstration, the memory matrix T_{OT} is displayed on the video monitor, and an input vector V' , which represents the partial image of G, is presented on the input SLM of the system. After converging to a stable state, the output vector V^* , as shown in Fig. 9(d), is compared with the stored vectors O and T by using the Hamming distance as a criterion. More specifically, if the Hamming distance between the vectors V^* and O is shorter than that of T, the memory matrix T_{OG} will be used to replace the matrix T_{OT} . Afterward, the input vector V^* is fed into the network for a new round of iteration, for which the letter G is retrieved, as shown in Fig. 9(e). A flow chart diagram to illustrate this tree search operation is shown in Fig. 10.

VII. Concluding Remarks

A video monitor displaying the IWM offers the advantages of high resolution (1024×1024 pixels or more), a large dynamic range (~ 256 grey levels), and low cost. Further development of high definition TV technology would enable us to synthesize even larger neural networks with higher speed operation. Currently, integrated optics technology may provide a microlens array containing 30,000 interconnections on a glass substrate.²⁰ Given an addressing time of the ferroelectric SLM of the order of 10^{-4} s and a TV frame rate of 30 frames/s, the operational speed of the proposed system with 1024 fully interconnected neurons can be as high as $10^4 \times 1024 \times 1024 = 1.05 \times 10^{10}$ operations/s. However, if the MR algorithm is used, in which the operation speed is dependent on the addressing speed of the TV monitor, the system would have a speed of $30 \times 1024 \times 1024 = 3.146 \times 10^7$ operations/s.

Modifications of the Hopfield model, such as the orthogonal projection and multilevel recognition algorithms, are implemented in the proposed system as shown in this paper. We stress that the proposed optical neural network can also be used to implement multilayer and high-order neural networks. The preliminary experimental demonstrations and simulated results have revealed that the proposed optical neural network possesses high programmability and parallel operation, which in principle can be made highly adaptive.

References

1. N. H. Farhat and D. Psaltis, "Optical Implementation of Associative Memory Based on Models of Neural Networks," in *Optical Signal Processing*, J. L. Horner, Ed. (Academic, New York, 1987), pp. 129-162.
2. N. H. Farhat, D. Psaltis, A. Prata, and E. Paek, "Optical Implementation of the Hopfield Model," *Appl. Opt.* **24**, 1469-1475 (1985).
3. R. A. Athale, H. H. Szu, and C. B. Friedlander, "Optical Implementation of Associative Memory with Controlled Nonlinearity in the Correlation Domain," *Opt. Lett.* **11**, 482-484 (1986).
4. P. Lalanne, J. Taboury, J. C. Saget, and P. Chavel, "An Extension of the Hopfield Model Suitable for Optical Implementation," *Proc. Soc. Photo-Opt. Instrum. Eng.* **813**, 27-30 (1987).
5. A. D. Fisher and J. N. Lee, "Optical Associative Processing Elements with Versatile Adaptive Learning Capabilities," in *Technical Digest, Topical Meeting on Optical Computing* (Optical Society of America, Washington, DC, 1987), paper TUA5-1.
6. J.-S. Jang, S.-W. Jung, S.-Y. Lee, and S.-Y. Shin, "Optical Implementation of the Hopfield Model for Two-Dimensional Associative Memory," *Opt. Lett.* **13**, 248-250 (1988).
7. B. Macukow and H. H. Arsenault, "Optical Associative Memory Model Based on Neural Networks Having Variable Interconnection Weights," *Appl. Opt.* **26**, 924-928 (1987).
8. D. Psaltis, J. Yu, X. G. Gu, and H. Lee, "Optical Neural Nets Implemented with Volume Holograms," in *Technical Digest, Topical Meeting on Optical Computing* (Optical Society of America, Washington, DC, 1987), paper TUA3-1.
9. M. Takeda and J. W. Goodman, "Neural Networks for Computation: Number Representations and Programming Complexity," *Appl. Opt.* **25**, 3033-3046 (1986).
10. R. Hecht-Nielsen, "Performance Limits of Optical, Electro-Optical, and Electronic Neurocomputers," *Proc. Soc. Photo-Opt. Instrum. Eng.* **634**, 277-306 (1986).
11. J. J. Hopfield, "Neural Network and Physical System with Emergent Collective Computational Abilities," *Proc. Natl. Acad. Sci. USA* **79**, 2554-2558 (1982).
12. K. Kohonen, *Self-Organization and Associative Memory* (Springer-Verlag, Berlin, 1984).
13. D. E. Rumelhart and J. L. McClelland, Eds., *Parallel Distributed Processing: Explorations in the Microstructure of Cognition, Vols. 1 and 2* (MIT Press, Cambridge, 1986).
14. S. Wu, T. Lu, X. Xu, and F. T. S. Yu, "An Adaptive Optical Neural Network Using a High Resolution Video Monitor," *Microwave and Optical Technology Letters*, **2**, 252-257 (1989).
15. G. Eichmann and M. Stojancic, "Superresolving Signal and Image Restoration Using a Linear Associative Memory," *Appl. Opt.* **26**, 1911-1918 (1987).
16. K. M. Johnson, M. A. Handschy, and L. A. Pagano-Stauffer, "Optical Computing and Image Processing with Ferroelectric Liquid Crystals," *Opt. Eng.* **26**, 385-391 (1987).
17. J. S. Patel and J. W. Goodby, "Properties and Applications of Ferroelectric Crystals," *Opt. Eng.* **26**, 373-384 (1987).
18. G. H. Golub and C. F. Van Loan, *Matrix Computation* (Johns Hopkins Press, Baltimore, 1983).
19. G. Z. Sun, H. H. Chen, and Y. C. Lee, "Learning Decision Trees Using Parallel Sequential Induction Network," in *Technical Digest, First Annual Meeting, International Neural Network* (Pergamon Press, Boston, 1988).
20. W. Veldkamp, "Amacronic Sensors," in *Technical Digest, First Annual Meeting, International Neural Network* (Pergamon Press, Boston, 1988).

We acknowledge the support by the U.S. Air Force, Rome Air Development Center, Hanscom Air Force Base, MA, under contract F19628-87-C-0086.

RAPID COMMUNICATIONS

This section was established to reduce the lead time for the publication of Letters containing new, significant material in rapidly advancing areas of optics judged compelling in their timeliness. The author of such a Letter should have his manuscript reviewed by an OSA Fellow who has similar technical interests and is not a member of the author's institution. The Letter should then be submitted to the Editor, accompanied by a LETTER OF ENDORSE-

MENT FROM THE OSA FELLOW (who in effect has served as the referee and whose sponsorship will be indicated in the published Letter), A COMMITMENT FROM THE AUTHOR'S INSTITUTION TO PAY THE PUBLICATIONS CHARGES, and the signed COPYRIGHT TRANSFER AGREEMENT. The Letter will be published without further refereeing. The latest Directory of OSA Members, including Fellows, is published in the July 1988 issue of Optics News.

Optical disk based neural network

Taiwei Lu, Kyusun Choi, Shudong Wu, Xin Xu, and Francis T. S. Yu

Pennsylvania State University, Department of Electrical Engineering, University Park, Pennsylvania 16802.

Received 21 August 1989.

Sponsored by Jacques Ludman, Rome Air Development Center.

0003-6935/89/224722-03\$02.00/0.

© 1989 Optical Society of America.

Using an optical disk as a large capacity associative memory in an optical neural network is described. The proposed architecture is capable of data processing at high speed.

It is well known that optics is capable of performing massive interconnection in 3-D space. Several optical neural network architectures have shown potential for high speed parallel processing.^{1,2} Recently, the rapid growth of optical disk (OD) storage techniques has provided another advantage for optics in large capacity information storage and processing.³ In this Communication, we propose an OD based optical neural network architecture for high speed and large capacity associative processing.

The OD stores information in a binary form. Two neural network models, i.e., the binary pattern associator (BPA)⁵ and the tristate interpattern association (IPA) model⁶ are suitable for mapping the interconnection weight matrix (IWM) on an optical disk. Since the IWM for the BPA is a binary matrix, it can be directly recorded on an OD. The IPA model assigns to each element [either a 1 (i.e., excitation) or -1 (i.e., inhibition) or 0 (i.e., no relation) in the IWM] based on the association of special and common features among reference patterns. Since the IWM can be written into positive and negative binary matrices T^+ and T^- , respectively, T^+ and T^- can be separately recorded on an OD.

Figure 1 shows an optical neural network using an OD for the large capacity storage of IWMs. In this figure, a pulse laser beam is divided into two orthogonally polarized beams by a polarized beam splitter PBS1. These beams are directed to the moving heads scanning on both sides of the OD, on which T^+ and T^- can be simultaneously read out. Thus the positive and negative matrices of IWM are orthogonally polarized. Each moving head consists of a mirror, polarized beam splitter, quarterwave plate, and microscopic lens to enlarge the readout matrix. The moving heads travel along the diagonal lines of the disk that cover the most inner to the most outer tracks. Polarized beam splitters PBS2 and PBS3 are aligned in the same direction as the incoming beams. Since each reading beam passes the quarterwave plate twice, it rotates the polarization plane by 90° and is reflected by

PBS2 and PBS3. The readout beams are then enlarged by the microscopic lenses L2 and L3, respectively, and then superimposed on a diffuser. Notice that the structure behind the diffuser is basically the same optical neural network as described in Ref. 2.

For a single layer neural network with $N \times N$ neurons, the IWM is a 4-D matrix of N^4 elements, which can be partitioned into an array of $N \times N$ submatrices, and each submatrix is of $N \times N$ size.⁶

A lenslet array consisting of $N \times N$ small lenses is used to establish the optical interconnections between the IWM and input pattern, where a moderate sized SLM with $N \times N$ pixels serves as the input device. As depicted in Fig. 2, the light beam emitted for each submatrix from the diffuser is imaged by a specific lens of the lenslet array onto the input SLM. Thus an $N \times N$ number of submatrices is added onto the input device. The overall transmitted light can be separated by PBS4 and then imaged at the output plane to form two $N \times N$ output arrays, which represent the product of the 4-D interconnection weight matrix (i.e., T^+ and T^-) and 2-D input pattern.

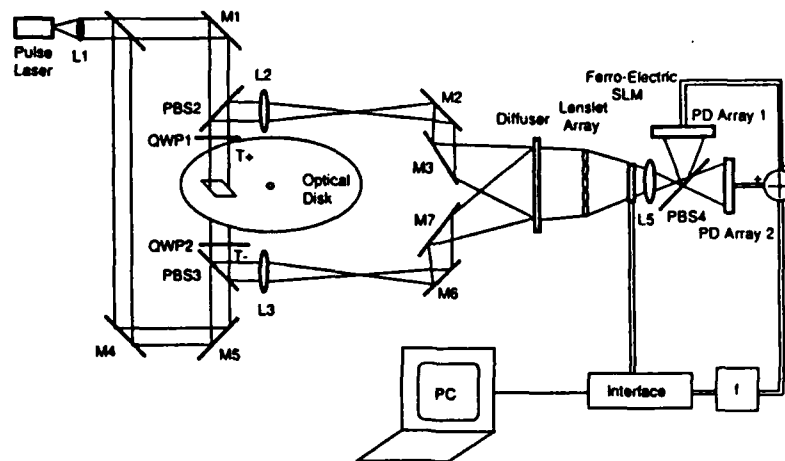
To form a closed loop neural network, the electronic signals from two detector arrays PD1 and PD2 are sent to a parallel electronic postprocessing array. The circuit would consist of a buffer, comparator array, and thresholding array. The output pattern can be fed back to the input SLM for further iterations or sent to the microcomputer for decision making via an interfacing circuit.

We propose that a ferroelectric liquid crystal SLM be used as the input device of the system. Accordingly, its contrast ratio can be as high as 125:1.⁷ Since the SLM can be parallelly addressed, the detector and input arrays can communicate in parallel. Thus the electrooptical feedback loop can be performed in a completely parallel manner.

Several types of optical disk are commercially available, such as the read-only CD-ROM, the write-once optical disk, and the magneto-optical erasable disk. Here we select Optimen 1000, a 30-48-cm (12-in.) diam read-only OD, as an example, which can store as much as 2.05 Gbytes of information on two sides of the disk.⁸

The area on the disk surface on which the laser beam is focused is chosen to be 1 mm². This is primarily due to the limitation of L2 and L3, the microscopic lenses' field of view, in which the magnification factor is ~70. An area of 1 mm² consisting of 529 × 529 bits can be used to store the IWM for a 23 × 23-neuron network. The configuration of an Optimen 1000 OD and the arrangement of blocks in tracks and sectors on the disk are illustrated in Fig. 3. Note that the number of blocks varies radially in different sectors. Although there is a slight distortion of the blocks due to the radial structure of the disk, it can be compensated by either lenses L2 and L3 or input SLM with photodetector arrays.

To retrieve an association, the moving heads would simply



L: Lens
M: Mirror
PBS: Polarized Beam Splitter
QWP: Quarter Wave Plate
T+: Positive Part of IWM
T-: Negative Part of IWM
f: Nonlinear Thresholding Function
PD: Photo-Detector

Fig. 1. Optical disk based neural network architecture.

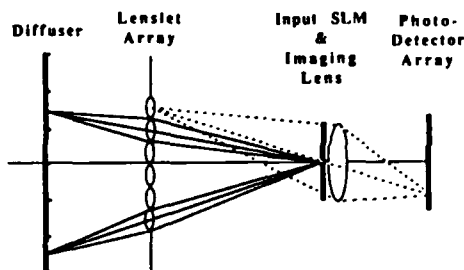


Fig. 2. Optical arrangement of the neural network.

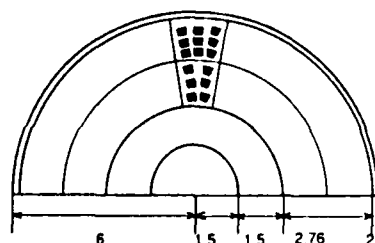


Fig. 3. Optimen 1000 disk and the IWM blocks on disk.

aim at the right blocks to capture the IWM with pulse laser and then image them on the diffuser. The pulse width and power of the laser are related to the response time and sensitivity of the photodetector array. The response time of a typical photodetector is in the 1-ns range for which a pulse laser in nanosecond width should be chosen. The required power of the laser can be estimated:

$$\eta P_L > S_P \quad (1)$$

where P_L is the power of the laser, S_P is the sensitivity of the detector, and the absorption coefficient η of the system can be written $\eta = 0.5t_1t_2t_3$, t_1 represents the reflectivity of the OD, t_2 the transparency of the input SLM, and t_3 the energy loss factor between the diffuser and input device.

We assume, for example, that $t_1 = 0.5$, $t_2 = 0.2$, $t_3 = 5 \times 10^{-3}$, and $S_P = \sim 10^{-5}$ W; the laser power can be estimated as

$$P_L > 10^{-5} / (0.5 \times 0.5 \times 0.2 \times 5 \times 10^{-3}) = 40 \text{ mW}.$$

Now let us consider the requirement for the rotation speed of an OD driver. The size of a pit is $\sim 1 \mu\text{m}$ on the OD surface. The traveling distance of the moving heads should not exceed $1 \mu\text{m}$ in pulse duration (i.e., 1 ns) to avoid blurring. Therefore, the maximum spinning speed of OD is given by

$$V_{OD} = 10^{-6} \times 10^9 \times 60 / (\pi \times 12 \times 0.025) = 63,662 \text{ rpm},$$

which well exceeds the speed of the commercially available OD driver ($\sim 1122 \text{ rpm}$). We shall use the 1122 rpm to estimate the performance of the proposed optical neural network.

Based on the above design parameters, there are $\sim 14,600$ blocks of the 529×529 matrix on each side of the OD. Assume that each block can store fifty associations by using the IPA model; there would be $\sim 730,000$ associations per disk. Notice that this number is almost 5 times the 150,000 entries of a Webster's Collegiate Dictionary.

Since the existent OD driver spins at 1122 rpm, the reading

heads take $\sim 45 \mu\text{s}$ on average to move from one block to another. We assume that the parallel electronic circuit performs postprocessing within this duration. Since each block consists of 279,841 connections, this yields an average processing rate of about

$$V_p = 2 \times 279,841 / (45 \times 10^{-6}) = 12.4 \times 10^9 \text{ connections/s.}$$

Compared with the currently available electronic processor (designed for neurocomputing) at $\sim 22 \times 10^6$ connections/s,⁹ the speed up factor of the proposed optical neural network is ~ 560 .

If we assume that the parallel electronic postprocessing can be completed in $2 \mu\text{s}$ and the disk driver can spin at $\sim 31,800$ rpm instead of 1122 rpm, the processing rate of the proposed system would be as high as

$$V_{p\text{max}} = 2 \times 279,841 / (2 \times 10^{-6}) = 279.841 \times 10^9 \text{ connections/s.}$$

There are, however, several problems that should be addressed before constructing the optical disk based neural network.

The readout head has to be redesigned for reading the whole block of an IWM rather than sequential readout techniques.¹⁰

The existent SLM still cannot catch up with the processing speed of the proposed system (i.e., $\sim 10^9$ Hz). However, the optical disk based neural network is suitable for applications to a huge database associative search, which does not require a frequent change of input patterns.

The electronic bottleneck in the feedback loop may be alleviated to some extent by using parallel buffers. However, a decision making circuit for postprocessing the output data in $2\text{--}45 \mu\text{s}$ has to be developed.

Nevertheless, the proposed optical disk based neural network offers a large capacity associative database for which high speed operation can be achieved.

We acknowledge the support by U.S. Air Force, Rome Air Development Center, Hanscom Air Force Base, MA, under contract F19628-87-C-0086.

References

1. N. H. Farhat, D. Psaltis, A. Prata, and E. Pack, "Optical Implementation of the Hopfield Model," *Appl. Opt.* **24**, 1469-1475 (1985).
2. T. Lu, S. Wu, X. Xu, and F. T. S. Yu, "A 2-D Programmable Optical Neural Network," *Microwave and Opt. Tech. Lett.*, **2**, 252-257 (1989).
3. R. P. Freese, "Optical Disks Become Erasable," *IEEE Spectrum* **41-45** (Feb. 1988).
4. J. A. Anderson, "Cognitive and Psychological Computation with Neural Models," *IEEE Trans. Syst. Man Cybernet.* **SMC-13**, 799-815 (1983).
5. T. Lu, X. Xu, S. Wu, and F. T. S. Yu, "A Neural Network Model Using Inner-Pattern Association," submitted to *Appl. Opt.*
6. N. H. Farhat and D. Psaltis, "Optical Implementation of Associative Memory Based on Models of Neural Networks," in *Optical Signal Processing*, J. L. Horner, Ed., (Academic, New York, 1987), pp. 129-162.
7. K. M. Johnson, M. A. Handschy, and L. A. Pagano-Stauffer, "Optical Computing and Image Processing with Ferroelectric Liquid Crystals," *Opt. Eng.* **26**, 385-391 (1987).
8. *Optimem 1000 Sales Brochure* (Optimem, Inc., Mountain View, CA, 1989).
9. Technology News, "SAIC Ships DELTA II," *Neural Networks* **2**, 157-158 (1989).
10. D. Psaltis, A. A. Yamamura, M. A. Neifeld, and S. Kobayashi, "Parallel Readout of Optical Disk," in *Technical Digest, Topical Meeting on Optical Computing* (Optical Society of America, Washington, DC, 1989), paper ME3-1.

A REMINDER

Authors submitting Rapid Communications for publication must remember to include a letter from their institution agreeing to honor the publication charge. Otherwise publication will be delayed—and the whole idea of this section of Letters to the Editor is defeated.

SYMBOLIC LOGIC PROCESSOR USING CASCADED LIQUID CRYSTAL TELEVISIONS (LCTVs)

Francis T. S. Yu, Yong Jin, and Chenhua Zhang

Electrical Engineering Department
The Pennsylvania State University
University Park, Pennsylvania 16802

KEY TERMS

Optical logic processor, liquid crystal televisions, optical computing, signal processing

ABSTRACT

A shadow casting optical logic array processor using cascaded programmable liquid crystal televisions (LCTVs) is described. We have shown that the 16 basic logic operations can be easily achieved with this technique. A technique of performing two-level logic function using a modified version of this proposed architecture is also given. We have shown that any two-level logic function can be performed with this technique. The experimental demonstrations of this optical symbolic logic processor are also provided.

I. INTRODUCTION

An optical logic array processor using shadow casting technique was first proposed by Tanida and Ichioka [1]. They have shown that efficient binary logic operations can be performed with the parallelism of optics. Subsequently, Li, Eichmann and Alfano [2] have demonstrated a hybrid encoding logic using shadow casting for digital optical computing. A technique of using polarization-encoding for the shadow casting logic unit was reported by Karim, Awwal, and Cherri [3]. Interesting optical space-variant logic array based on the shadow casting principle was also discussed by Yatagai [4].

Recently, liquid crystal televisions (LCTVs) have been frequently applied to optical signal processing, because of their low cost and programmability [5-8]. We have proposed a symbolic logic processor utilizing cascaded LCTVs to perform the logic operation [9], in which two input patterns and the operational mask are, respectively, written on three cascaded LCTVs.

In this paper, we shall discuss the basic logic operation as obtained from this hybrid optical processor. A technique to perform two-level logic functions based on this architecture is also included. Experimental demonstrations obtained with this proposed symbolic logic processor are provided. The apparent advantages of using the cascaded LCTVs as applied to symbolic logic processing must be the low cost and programmability.

II. LCTV SYMBOLIC LOGIC PROCESSOR

A LCTV symbolic logic processor using the shadow casting technique is depicted in Figure 1. A collimated light which can be either coherent or incoherent light is used to illuminate three cascaded LCTVs. Two input encoded patterns are written on LCTV1 and LCTV2, respectively. The third LCTV generates the operational mask corresponding to a particular logic operation. The product of three patterns is then imaged onto a CCD area detector, in which the output data represent the logic operation. To encode input logic data, a binary pattern is divided into 2×2 cells, called logic units. As an example, input logic units (or patterns) a and b are, respectively, illustrated in Figure 2(a). Since LCTV1 and LCTV2 are closely cascaded, the combination states of these encoded

input logic units can be represented by the patterns shown in Figure 2(b). The operational mask displayed on LCTV3 is depicted in Figure 2(c), in which $(\alpha, \beta, \gamma, \delta)$ represent the switching states (0 or 1). Thus, we see that the complete 16 logic operations can be easily obtained by using the cascaded LCTV technique, as given in Figure 3.

The experimental demonstrations have been obtained with this proposed LCTV architecture. As an example, the results of the exclusive-OR (EOR) logic operation are presented in Figure 4. Although, in principle, a logic unit can be encoded onto 2×2 LCTV pixels, due to alignment difficulty, 8×8 pixels have been used in our experiment.

III. SYMBOLIC LOGIC FUNCTION PROCESSOR

In this section, a technique of performing two-level logic functions, based on the proposed architecture mentioned above, is described. We note that any two-level logic function can be expressed in the sum-of-product form as

$$\begin{aligned} f(x_1, x_2, \dots, x_n) \\ = a_1 x_1 x_2 + a_2 \overline{x_1} x_2 + a_3 x_1 \overline{x_2} + a_4 \overline{x_1} \overline{x_2} + \dots \\ + a_{m-3} x_{n-1} x_n + a_{m-2} \overline{x_{n-1}} x_n \\ + a_{m-1} x_{n-1} \overline{x_n} + a_m \overline{x_{n-1}} \overline{x_n} \end{aligned} \quad (1)$$

where a_i is 0 or 1 determined by the particular function, x_i and $\overline{x_i}$ are the logic and the inverted logic variables, respectively, and

$$m = n(n-2) \quad (1a)$$

To perform a two-level logic function as described in Eq. (1), the product term of every two logical variables must first be obtained and then added accordingly to the particular function. To obtain the combinations of any two logic variables, the variable patterns and operational mask are generated into the cascaded LCTVs as schematically depicted in Figure 5. For example, each variable pattern is written in row direction in LCTV1, and in column direction in LCTV2, respectively. The operational masks determined by the required function are programmed into LCTV3. The corresponding output light distribution behind LCTV3 must be the combinations of two logic variables. Figure 6 depicts the optical setup of a modified symbolic logic function processor. The basic difference between this architecture and the previous one is using a focusing lens L_2 to integrate the output intensity from the cascaded LCTVs. It is therefore apparent that the logic OR operation can be obtained with this setup. A photocell located at the focal point of L_2 is to detect the intensity which represents the output logic function. If there is a logical "1" behind LCTV3, a peak can be detected by this photocell indicating a "1"; otherwise, it has "0" output. To increase the system accuracy, an electrical thresholding circuit is used after the photocell. Since the output function is represented by an electrical signal, it can be directly stored into the high-speed memory subsystem of a microcomputer for further usage. Furthermore, if one uses high contrast spatial light modulators (LCTVs), this proposed architecture will provide a possible method to perform multilevel logic functions.

We now provide a couple of experimental demonstrations obtained with this proposed architecture. Two logic functions

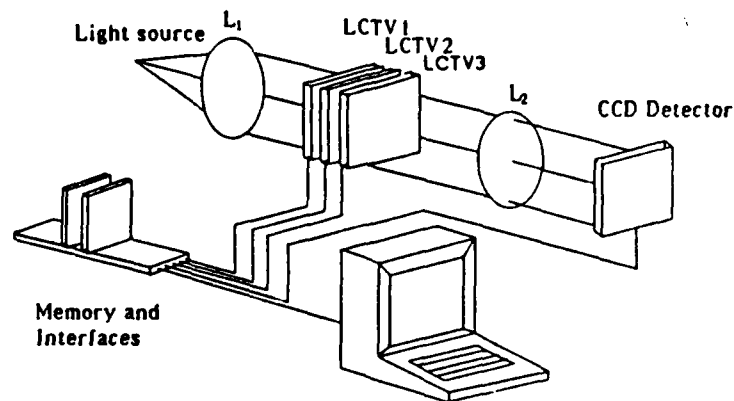


Figure 1 A symbolic logic operation processor using cascaded LCTVs

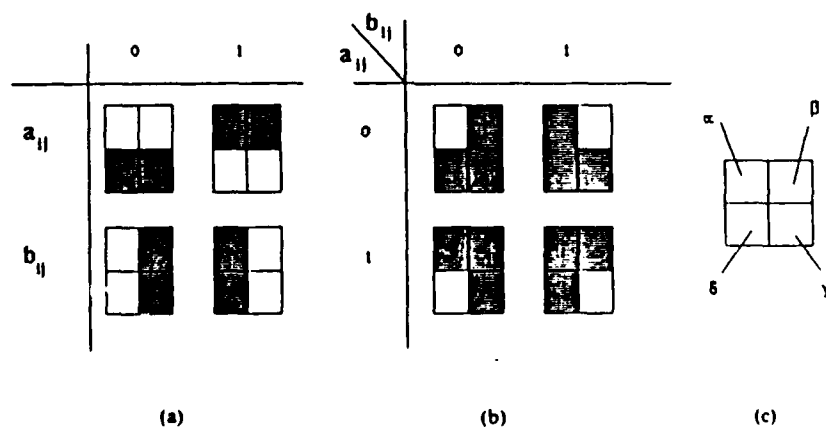


Figure 2 (a) Encoded input patterns. (b) Product of the input patterns. (c) A logic mask

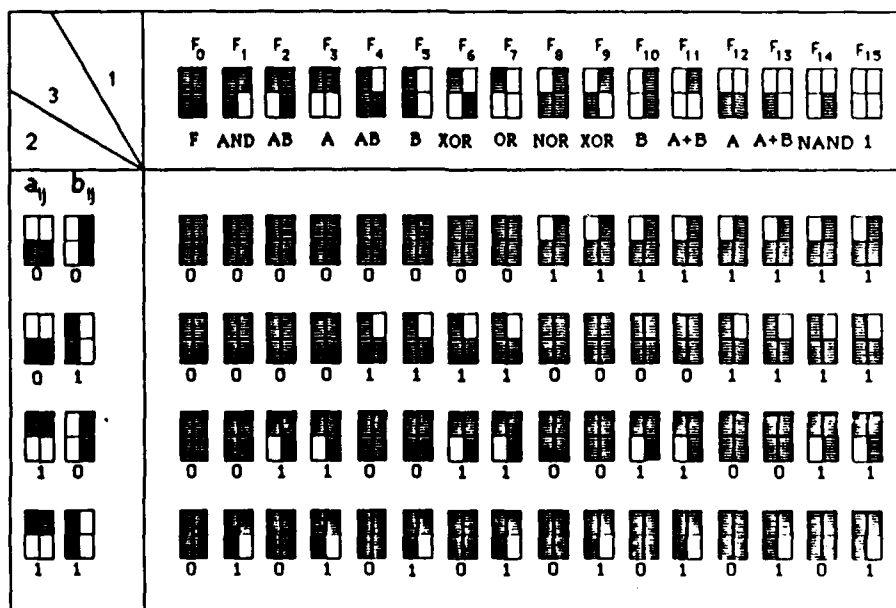


Figure 3 Representation of the 16 logic operations

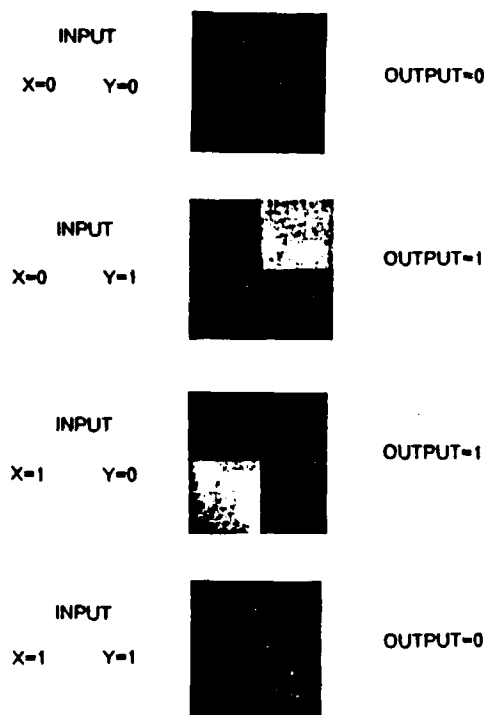


Figure 4 Outputs of exclusive-OR operation

A	B	C	F ₁	F ₂
0	0	0	0	1
0	0	1	0	0
0	1	0	0	1
0	1	1	1	1
1	0	0	0	1
1	0	1	1	0
1	1	0	1	0
1	1	1	1	0

Figure 7 Truth tables of the two logic functions

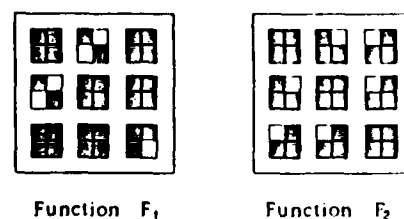


Figure 8 Operational masks for (a) function 1 and (b) function 2

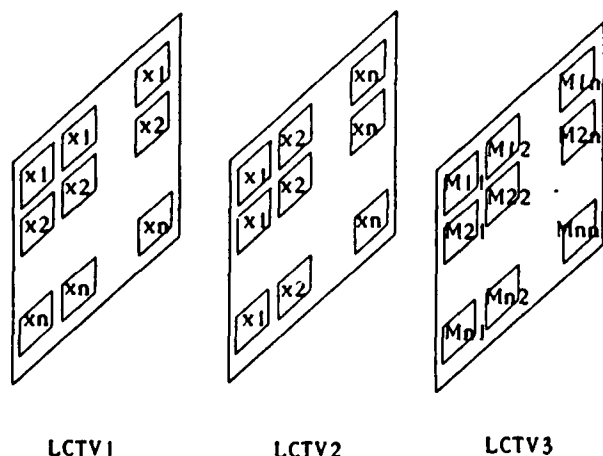


Figure 5 Spatial arrangements of logic variables in logic function processor

are chosen as examples:

$$f_1(A, B, C) = A \oplus B + C; \quad (2)$$

$$f_2(A, B, C) = \bar{A}\bar{C} + A\bar{B} + BC. \quad (3)$$

Figure 7 illustrates the truth table of these functions. With reference to the logic functions of Eqs (2) and (3), two operational masks (i.e., LCTV3) for Eqs (2) and (3) are as depicted in Figure 8(a) and (b), respectively. We note that $CC = C$ is used to obtain C in the operational mask (LCTV3) of $f_1(A, B, C)$. The output intensity distributions corresponding to the two logic functions F_1 and F_2 by using the input logic variables (LCTV1 and 2) and the logic operational masks of Figure 8(c) and (d) (LCTV3), respectively, are given in Figure 9. By detecting the zero-order intensities, binary values of the logic functions of f_1 and F_2 can be obtained. This can be easily done by thresholding the output intensity

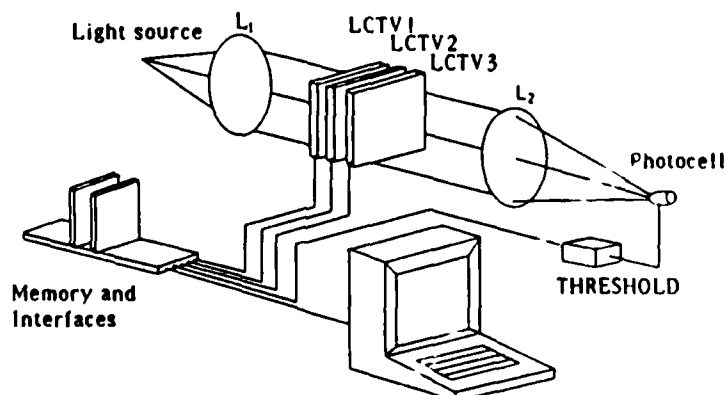


Figure 6 A symbolic logic function processor

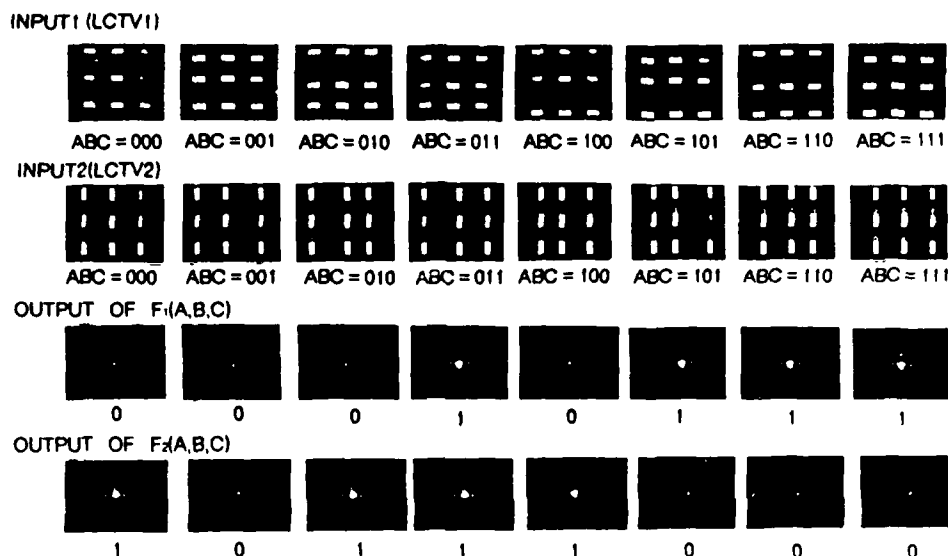


Figure 9 Output of function 1 and function 2 with different inputs

level. For example, as shown in the fourth column, the output logic value of F_1 is measured as 1, with respect to input $A = 0$, $B = 1$, and $C = 1$. For the fifth column, the logic value of F_1 is 0, with respect to the input $A = 1$, $B = 0$, and $C = 0$. Thus, we see that any two-level logic function can be performed easily with this proposed symbolic logic processor.

IV. DISCUSSION

Since a one-cell-to-one-cell shadow casting relationship is required in the proposed technique, the separation of the cascaded LCTVs must be adequately small, so that the diffraction effect from one cell imaged onto another cell is negligibly small, i.e. [10, 11],

$$Z \ll \frac{d^2}{\lambda} \quad (4)$$

where λ is the illuminating wavelength, Z is the overall distance between LCTV1 and LCTV3, and d is the width of a square cell. In our experimental demonstration the wavelength of the He-Ne laser is $\lambda = 632.8 \text{ nm}$ and the width of the unit cell is $d = 370 \mu\text{m}$. Then the overall separation of cascaded LCTVs is required as

$$Z \ll 22 \text{ cm} \quad (5)$$

In our experiments, we have used $Z = 5 \text{ cm}$, which is well within the constraint of the calculated result of Eq. (5). Since the transmittance of the LCTV is rather low (about 10% for the Radio Shack Pocketvision 5), the overall transmittance of the cascaded LCTVs would be about 0.1%. Nevertheless, relatively good results have been obtained from our experiments. The absorption of the transmitted light is primarily due to the low-quality polarizer used in the LCTV. Thus, to improve the performance of the LCTV, a high quality polarizer should be implemented.

V. CONCLUSIONS

We have demonstrated that optical symbolic logic operation can be easily achieved with cascaded low-cost LCTVs. Aside

from the basic 16 logic operations, we have shown that the same processor can perform any two-level logic function. Major limitations of using LCTV must be the low resolution, low contrast, low speed and low transmittance, which prevents widespread practical applications. Nevertheless, the low cost and programmability of the LCTV would stimulate some interest in the application of symbolic logic processing. Since the digital computation can be divided into a series of specific logic functions, perhaps some specialized digital uniprocessors may be implemented based on this proposed optical processor.

ACKNOWLEDGMENTS

We acknowledge the support of the U.S. Air Force, Rome Air Development Center, Hanscom Air Force Base, Massachusetts, under contract F19628-87-C-0086.

REFERENCES

1. J. Tanida and Y. Ichioka, "Optical Logic Array Processor," in *Proceedings, Tenth IOCC*, 1983, p. 18.
2. Y. Li, G. Eichmann, and R. R. Alfano, "Optical Computing using Hybrid Encoding Shadow Casting," *Appl. Opt.*, Vol. 25, 1986, p. 2636.
3. M. A. Karim, A. A. S. Awwal, and A. K. Chenni, "Polarization-Encoded Optical Shadow-Casting Logic Units: Design," *Appl. Opt.*, Vol. 26, 1987, p. 2720.
4. T. Yatagai, "Optical Space-Variant Logic Gate Array Based on Spatial Encoding Technique," *Opt. Lett.*, Vol. 11, 1986, p. 260.
5. H. K. Liu, J. A. Davis, and R. A. Lilly, "Optical-Data-Processing Properties of a Liquid-Crystal Television Spatial Light Modulator," *Opt. Lett.*, Vol. 10, 1985, p. 635.
6. D. A. Gregory, "Real-Time Pattern Recognition Using a Modified Liquid Crystal Television in a Coherent Optical Correlator," *Appl. Opt.*, Vol. 25, 1986, p. 467.
7. A. M. Tai, "Low-Cost LCD Video Display for Optical Processing," *Appl. Opt.*, Vol. 25, 1986, p. 1380.
8. F. T. S. Yu, "Real-Time Polychromatic Signal Detection Using a Color Liquid Crystal Television," *Opt. Eng.*, Vol. 26, 1987, p. 453.
9. F. T. S. Yu, "Hybrid Optical Computing," *IEEE Potentials*, Vol. 6, 1987, p. 34.
10. A. W. Lohmann, *Optical Information Processing*, Erlangen, 1978.

11. F. T. S. Yu, S. Jutamulia, and D. A. Gregory, "Real-Time Liquid Crystal TV XOR- and XNOR-Gate Binary Image Subtraction Technique," *Appl. Opt.*, Vol. 26, 1987, p. 2736.

Received 5-29-89

Microwave and Optical Technology Letters, 2/9, 309-313
 © 1989 John Wiley & Sons, Inc.
 CCC 0895-2477/89/\$4.00

NEW DESIGN OF FLAT GAIN AND WIDEBAND FIELD EFFECT STRUCTURE

Christophe Byl and Yves Crosnier
 Centre Hyperfréquences et Semiconducteurs
 U.A. 287 CNRS — Bât P4
 Université des Sciences et Techniques de Lille Flandres Artois
 59655 Villeneuve D'Ascq Cedex, France

KEY TERMS

Traveling wave field effect transistor, wideband integrated amplifiers

ABSTRACT

This paper provides a new possibility of realizing in chip form wideband amplifiers with simple wide gate field effect structures, by taking advantage of especially designed electrode terminations to overcome inherent traveling wave losses. Demonstration of these properties is performed through various realizations and is based on distributed equivalent circuit modelling.

1. INTRODUCTION

Applications of the traveling wave concept to GaAs long electrode field effect devices have been widely studied in the past few years and have given rise to various attempts in the range of microwave functions as couplers, isolators, phase shifters, modulators, and amplifiers [1-5]. Among all these functions, amplification is one of the more exciting but it presents inherent difficulties due to the extreme complexity of the involved phenomena.

The present paper provides new insight on this topic and shows that the fundamental limitation related to propagation losses can be overcome, to a large extent, by using particular electrode configurations in association with on-chip implemented terminal lumped impedances. Such a property is first illustrated through experimental results carried out with a test single gate structure exhibiting a 1 mm gate width. Terminal impedances of various kinds are investigated and optimum configurations are demonstrated to greatly influence amplification bandwidth. Then these results are interpreted with the help of a simulation using a distributed circuit small signal approach operated with the SPICE program. Finally, taking advantage of properties stated throughout this study, we extend the application to moderate gate width (150-300 μm) FETs and we show, with especially realized devices, the possibility of achieving directly integrated amplifiers with very wide frequency bandwidth.

2. TEST STRUCTURE

A schematic representation of the test structure is given in Figure 1. The source electrode is uniformly grounded. Terminations 2 and 4, which correspond to parts of gate and drain

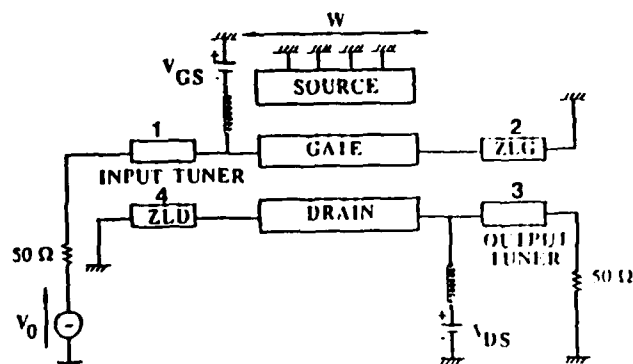


Figure 1 Schematic diagram of the test structure and its measurement mounting

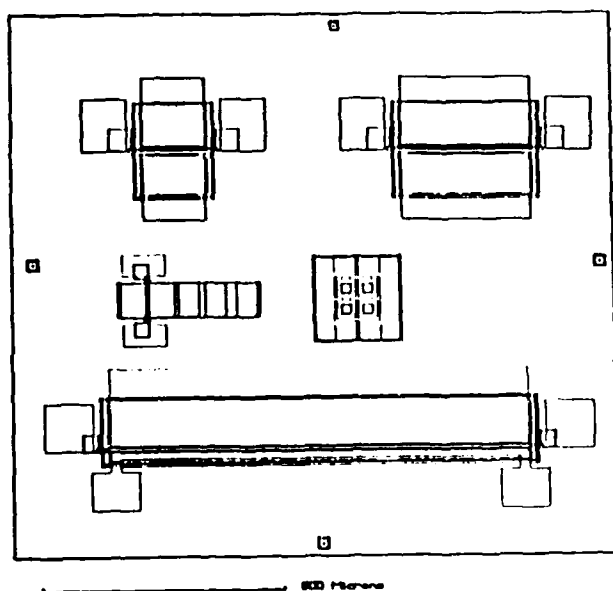


Figure 2 Mask topologies of the 1, 0.3, and 0.15 mm gate width structures studied

electrodes that would be open ended in a conventional FET configuration, are here connected to lumped impedances Z_{LG} and Z_{LD} . The choice of the nature of these impedances is performed according to the criteria of an optimization of the S parameters of the structure considered in a two port configuration, with termination 1 as input and termination 3 as output. This optimization consists of obtaining a substantial value for the maximum available gain (MAG) on the widest frequency bandwidth, but with minimized values of $|S_{11}|$ and $|S_{22}|$ in order to keep reasonable automatching conditions.

The structure has been realized in our laboratory with a 1 μm gate length, a 1 mm total width, and a 3 μm drain-source distance. Its exact topology is represented in Figure 2. As can be seen, its drain electrode width is only 8 μm in order to behave as a propagation line. The main characteristics of this structure are

- $g_m = 120 \text{ mS}$ (transconductance)
- $V_p = -2 \text{ V}$ (pinch off voltage)
- $R_g = 35 \Omega$ (gate resistance)

Letters to the Editors should be addressed to the Editor, APPLIED OPTICS, Georgia Institute of Technology, Atlanta, GA 30332-0252. If authors will state in their covering communications whether they expect their institutions to pay the publication charge, publication time should be shortened (for those who do).

Generalized perfect shuffle using optical spatial filtering

Q. W. Song and Francis T. S. Yu

Pennsylvania State University, Electrical Engineering Department, University Park, Pennsylvania 16802.

Received 1 August 1987.

0003-6935/88/071222-02\$02.00/0.

© 1988 Optical Society of America.

One of the inherent advantages of the optical computer is its noninteractive interconnecting capability. The optical perfect shuffle (PS) which forms the basis of such an interconnection network is a useful concept in optical computer architecture. Recently, proposals of optical PS have been made by Goodman *et al.*¹ and Marchic² for application to VLSI systems and single-mode optical fibers, respectively. More recently, Lohmann *et al.* implemented the optical PS with the use of four prisms.³ In this Letter, we shall demonstrate that two sets of data can be shuffled using an optical spatial filter. An experimental demonstration is also provided.

Originally, the term PS referred to a method of shuffling N number of cards ($N = 2^j$, and j is an integer). The upper half of the cards are removed and then interlaced with the lower half. Examples of PS applications to FFT and sorting algorithms have been discussed by Stone⁴ and Parker.⁵ In some applications, however, the use of other composite integer (M) inputs instead of N inputs is required. The perfect interlacing of the upper half of the M inputs with the lower half is called $G_{2,M/2}(i)$ class generalized perfect shuffle (GPS).⁶ Figure 1 shows a demonstration of $G_{2,3}(i)$ (i.e., $M = 6$). We note that PS is only a special case of the GPS in the class of $G_{2,M/2}(i)$, and this kind of shuffling of data can be quickly achieved by optical spatial filtering.⁷

The optical system to perform the $G_{2,M/2}(i)$ class GPS is depicted in Fig. 2. Two sets of data are designated by $s_1(x,y)$ and $s_2(x,y)$, which are separated by a distance 2β at the input plane P_1 . With coherent illumination, the complex light distribution at the spatial frequency plane P_2 can be described as

$$E(p,q) = S_1(p,q) \exp(-i\beta q) + S_2(p,q) \exp(i\beta q), \quad (1)$$

where $S_1(p,q)$ and $S_2(p,q)$ are the Fourier spectra of the input data $s_1(x,y)$ and $s_2(x,y)$, respectively. To implement perfect shuffle, we would place a sinusoidal grating in the Fourier plane P_2 . We assume that the grating formula is

$$H(q) = \frac{1}{2} [1 + \cos(q\beta + \Delta\beta)], \quad (2)$$

where $\Delta\beta$ is a small displacement constant. Thus, the output light field distribution on P_3 can be shown as

$$\begin{aligned} H(x,y) = & \frac{1}{2} s_1(x,y - \beta) + \frac{1}{2} s_2(x,y + \beta) \\ & + \frac{1}{4} [s_1(x,y - \Delta\beta) + s_2(x,y + \Delta\beta)] \\ & + \frac{1}{4} [s_1(x,y - 2\beta + \Delta\beta) + s_2(x,y + 2\beta + \Delta\beta)]. \end{aligned} \quad (3)$$

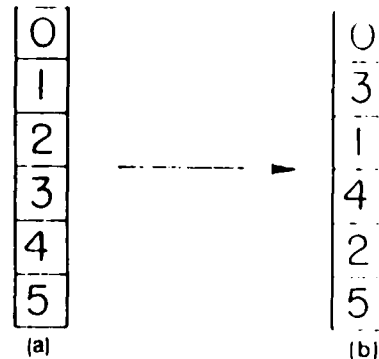


Fig. 1. Demonstration of $G_{2,3}(i)$ (i.e., $M = 6$) class GPS permutation: (a) input data; (b) the shuffled version. The numbers in small boxes represent the address of data.

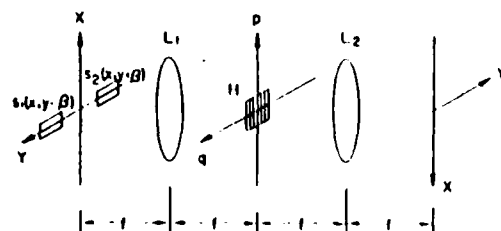


Fig. 2. Optical PS system: s_1 and s_2 , input data; L_1 , L_2 , lenses; H , filtering grating.

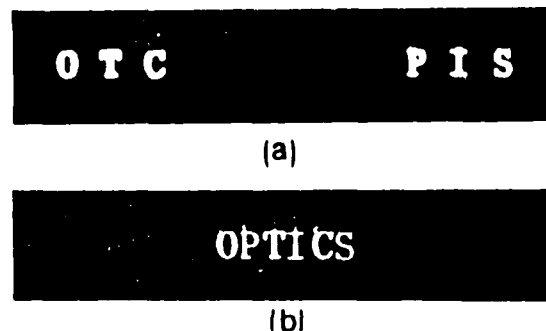


Fig. 3. Experimental result of the $G_{2,3}(i)$ GPS: (a) input data; (b) the shuffled version.

From the third term of Eq. (3), we see that $s_1(x,y)$ and $s_2(x,y)$ are slightly shifted in opposite directions along the Y axis. If the incremental shift $\Delta\beta$ is equal to the separation between the processing data, s_1 and s_2 would be perfectly interlaced. Thus, the two sets of input data would be perfectly shuffled.

In the experiment, we used two sets of English letters as input data for demonstration. Figure 3(a) shows the input data. Figure 3(b) gives the shuffled data obtained with the proposed technique. Note that the input and output format are not compatible. This will present no problem if we tailor design either the input or output data system. Suppose the input bit spot size is 0.1 mm, and their spacing in the X and Y directions is 0.25 and 0.5 mm, respectively, an 80 × 80-mm² aperture optical GPS can shuffle as many as 12,800 light channels. Furthermore, if two of the systems are cascaded in tandem, the PS operation can be applied to a 2-D data array, such that one shuffles horizontally and the other vertically. Obviously, the major disadvantage of the system is that it represents a negative process. With a phase-only sinusoidal grating, however, the energy efficiency can be increased to 33%. Considering the massive amounts of data it handles, the GPS might be a viable trade off for some applications.

We acknowledge the support of the U.S. Air Force Rome Air Development Center, Hanscom Air Force Base, under contract no. F19628-87-C-0086.

References

1. J. W. Goodman, J. F. Leonberger, S. Y. Kung, and R. A. Athale, "Optical Interconnections for VLSI Systems," *Proc. IEEE* 72, 850 (1984).
2. M. E. Marchic, "Combinatorial Star Couplers for Single-Mode Optical Fibers," *FOC/LAN 84* (1984), pp. 175-179.
3. A. W. Lohmann, W. Stork, and G. Stucke, "Optical Perfect Shuffle," *Appl. Opt.* 25, 1530 (1986).
4. H. S. Stone, "Parallel Processing with the Perfect Shuffle," *IEEE Trans. Comput.* C-20, 153 (1971).
5. D. S. Parker, Jr., "Notes on Shuffle/Exchange Type Switching Networks," *IEEE Trans. Comput.* C-29, 213 (1980).
6. G. Eichmann and Y. Li, "Compact Optical Generalized Perfect Shuffle," *Appl. Opt.* 26, 1167 (1987).
7. F. T. S. Yu, *Optical Information Processing* (Wiley, New York, 1983).

Curvature sensing and compensation: a new concept in adaptive optics

François Roddier

National Optical Astronomy Observatories, Advanced Development Program, P.O. Box 26732, Tucson, Arizona 85726.

Received 25 September 1987.

0003-6935/88/071223-03\$02.00/0.

© 1988 Optical Society of America.

We propose here a new concept for real time sensing and compensation of atmospherically distorted wavefronts using incoherent broadband sources. While light wavefront sensors currently used in adaptive optical systems all aim at measuring a vector field, the local wavefront tilts (or wavefront first derivatives) along two orthogonal directions.¹ We propose to measure instead the local wavefront curvature $\rho(x,y)$, Laplacian of the wavefront surface $z(x,y)$,

$$\rho(x,y) = \frac{\partial^2 z}{\partial x^2} + \frac{\partial^2 z}{\partial y^2} = \nabla^2 z, \quad (1)$$

together with wavefront tilts at the aperture edge in a direction perpendicular to the edge, i.e., for a circular aperture, radial tilts at the edge. Radial tilts provide the boundary conditions required to solve the Poisson Eq. (1) and estimate the wavefront $z(x,y)$, given the measured curvature distribution $\rho(x,y)$. This approach has several advantages:

(1) The wavefront curvature is a scalar field. It requires only one measurement per sample point. This is certainly easier than measuring a tilt vector field, which requires measuring the two components of the tilt vector at each sample point. Indeed we describe below a simple optical setup which gives both the local wavefront curvature inside the pupil and the wavefront slope at the pupil edge.

(2) Assuming inertial turbulence, the power spectrum of the wavefront surface decreases as $k^{-11/3}$, where k is the wavenumber. Hence, the power spectrum of the curvature varies as $k^{1/3}$; it is almost flat. This implies that curvature fluctuations at two different points are only slightly correlated. Since the process is Gaussian, they are almost statistically independent. This is not the case for tilts which are known to be highly correlated. Curvature measurements are therefore expected to be more efficient than tilt measurements.

(3) Perhaps the most interesting property of this approach is that membrane or bimorph mirrors can be used as analog devices which automatically solve the Poisson equation when proper voltages are applied. Hence the signal from a curvature sensor can be amplified and directly applied to the mirror without any computer processing.

Bimorph and membrane mirrors have been widely described in the literature. Bimorph mirrors are obtained by gluing a thin plate of glass or any other polished material to a sheet of piezoelectric material.²⁻⁵ The dynamic equation of state for an ideal mirror has the form¹

$$\frac{\partial^2 z'}{\partial t^2} = A \nabla^2 z' + B \nabla^2 V, \quad (2)$$

where $z'(x,y,t)$ is the mirror surface and $V(x,y,t)$ is the voltage distribution on the piezoelectric sheet as a function of time t ; A and B are constant coefficients. Membrane mirrors consist of an aluminum-coated stretched polymer foil. Deformation is obtained by means of electrostatic forces.⁶⁻⁹ The dynamic equation of state for an ideal membrane has the form⁷

$$\frac{\partial^2 z'}{\partial t^2} = A \nabla^2 z' + BP, \quad (3)$$

where $z'(x,y,t)$ is the membrane surface and $P(x,y,t)$ is the electrostatic pressure applied as a function of time t ; A and B are again constant coefficients. In both cases equilibrium is obtained when the mirror surface is the solution of a Poisson equation with appropriate boundary conditions. In other words, the effect of applying a local voltage or pressure is to

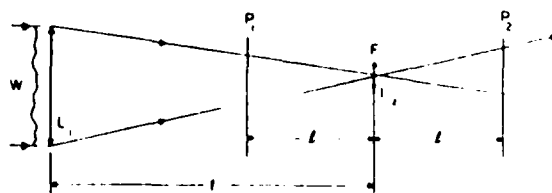


Fig. 1 Difference in illumination between planes P_1 and P_2 is a measure of the local curvature distribution in the incoming wavefront W . It also measures the wavefront radial tilt at the edge.

APPLICATIONS OF PHASE CONJUGATION TO A JOINT TRANSFORM CORRELATOR

Francis T.S. YU, Shudong WU and A.W. MAYERS

Pennsylvania State University, Department of Electrical Engineering, University Park, PA 16802, USA

Received 24 October 1988

An investigation of using phase conjugate techniques to remove phase distortion in a joint transform correlator (JTC) is presented. For improving the accuracy of detection, a phase encoding method based on the nonlinearity of phase conjugation is also proposed. Experimental results and computer simulations are provided.

1. Introduction

Recently, advances in photorefractive materials have stimulated interest in the application of phase conjugation techniques to a number of signal processing problems [1]. Presently, the phase conjugation mirror, based on the self pumped configuration [2] in photorefractive crystals, exhibits reflectivities as high as 70%, while requiring only a few tens of milliwatts of optical input power. Thus, this greatly extends the range of practical applications of phase conjugation mirrors. In this paper we will explore its application to a joint transform correlator (JTC). The JTC [3,4] is a powerful image processor, particularly for pattern recognition application, since it avoids the synthesis and alignment problems of a matched spatial filter. In most coherent image processing applications, the input objects are required to be free from any phase distortion. The input objects of a real time optical processor are usually generated by means of a spatial light modulator (SLM), however, most SLMs introduce some sort of phase distortion. We note that phase distortion can severely degrade the correlation characteristics in a JTC. Although liquid gates may be used to compensate the phase distortion to some extent, they can only remove the external distortion but generally can not compensate the internal distortion of the devices. Furthermore, holographic optical elements (HOE) may provide another means of phase distortion removal [5], but they have the disadvantages of critical alignment and cumbersome fabrication.

Another problem common to the JTC, as well as other coherent correlators, is that the width of the correlation spot is too broad, and the cross correlation intensity is too high. To improve the accuracy of correlation detection, the object functions can be pre-encoded. The inherent nonlinearities in phase conjugation may be used for this encoding process. Let us now consider a four-wave mixing JTC, as shown in fig. 1. We propose the object beam of the four-wave mixing is applied to the input of a JTC. Notice that this configuration would have two major advantages.

1. The phase distortion due to the input SLM can be automatically compensated by the conjugated wavefront.
2. An additional amplitude or phase modulation produced by the nonlinearity of phase conjugation

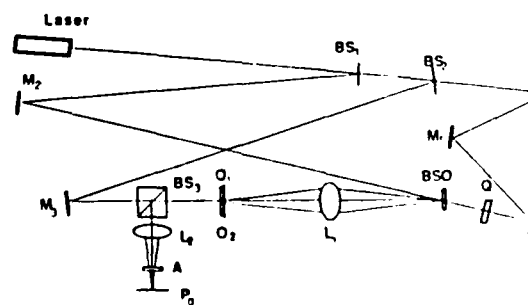


Fig. 1. Experimental setup. BS, Beam splitter; M, mirror; Q, quarter wave plate; A, analyzer; L₁, imaging lens; Fourier transform lens; P₀, output plane.

0030-4018/89/\$03.50 © Elsevier Science Publishers B
(North-Holland Physics Publishers Division)

may provide a means of improving the accuracy of correlation detection.

2. Principle

It is well known that phase conjugation can be produced with a photo-refractive crystal. With referring to the JTC in fig. 1, the readout beam is adjusted beyond the coherent length with respect to the writing beams. In other words, the setup represents a two-wave mixing configuration with a real-time readout beam. Notice that the expanded collimated Ar⁺ laser beam ($\lambda=0.5145 \mu\text{m}$) is divided into three paths. One is directed toward the photo-refractive crystal (BSO, $10 \times 10 \times 2 \text{ mm}^3$) by mirror M_2 and serves as the reference beam. The second is used to illuminate the input objects O_1 and O_2 , which are imaged onto the crystal by lens L_1 . The third is directed by mirror M_1 , M_5 , M_4 and serves as the readout beam. The reconstructed beam from the crystal is then imaged back to the input objects O_1 and O_2 for phase distortion removal. After passing through the input objects, the beam is then joint transformed in the output plane P_0 by lens L_2 , via a beam splitter BS_3 . We notice that a half wave plate Q , between the BSO crystal and mirror M_4 , is used to rotate the polarization of the readout beam. An analyzer A located at the front of the output plane is used to reduce the light scattered from the optical elements in the system.

With reference to the optical configuration of fig. 1, the object beam can be written as

$$\begin{aligned} O(x, y) \exp[i\phi(x, y)] \\ = O_1(x-b, y) \exp[i\phi_1(x-b, y)] \\ = O_2(x+b, y) \exp[i\phi_2(x+b, y)], \end{aligned} \quad (1)$$

where O_1 , O_2 , ϕ_1 and ϕ_2 are the amplitude and phase distortion of the input objects, respectively, b is the mean separation of the two input objects, and O_1 , O_2 are assumed positive real. At the image plane (i.e. the crystal), the object beam is given by

$$\begin{aligned} O(x/M, y/M) \exp[i\phi(x/M, y/M)] \\ \times \exp[ik(x^2+y^2)/2L], \end{aligned} \quad (2)$$

where M represents the magnification factor of the

imaging system, $L=s-f$, s is the image distance, f is the focal length of lens L_1 , $k=2\pi/\lambda$, λ is the wavelength of the light source.

Thus, the reconstructed beam emerging from the crystal is given by

$$\begin{aligned} O'(x/M, y/M) \exp[-i\phi(x/M, y/M)] \\ \times \exp[-ik(x^2+y^2)/2L] \exp[i\theta(x/M, y/M)]. \end{aligned} \quad (3)$$

Notice that expression (3) does not represent the exact phase conjugation of expression (2). The amplitude distribution of $O'(x, y)$ deviates somewhat from $O(x, y)$, which is primarily due to the nonlinearity of the BSO crystal [6]. A phase shift $\theta(x, y)$ between the phase conjugation and the reconstructed beam is also introduced. Later we will see that $\theta(x, y)$ is dependent on the intensity ratio R of the object beam and the reference beam. If there is no voltage applied on the BSO crystal, $\theta(x, y)$ would represent a constant phase of 90° .

As can be seen in fig. 1, the reconstructed beam, imaged back on the object plane, can be written as

$$O'(x, y) \exp[-i\phi(x, y)] \exp[i\theta(x, y)]. \quad (4)$$

After passing through the input objects, the complex light distribution becomes

$$O(x, y) O'(x, y) \exp[i\theta(x, y)]. \quad (5)$$

This expression shows that the phase distortion $\phi(x, y)$ of the input objects can essentially be removed, while the additional amplitude and phase modulation due to the nonlinearity of the BSO remain.

3. Phase distortion compensation

The phase distortion of the input objects (i.e. due to the SLM) can severely degrade the correlation characteristics. We have computer simulated some of these effects. The simulations were obtained with a test input pattern joint correlated with the same pattern added with random phase noise. We assumed that the random phase noise has a uniform probability distribution over a phase interval $[-\sigma, \sigma]$. Fig. 2 shows a plot of correlation peak intensity as a function of phase deviation σ . From this graph, we see that the normalized peak drop of 0.5 corre-

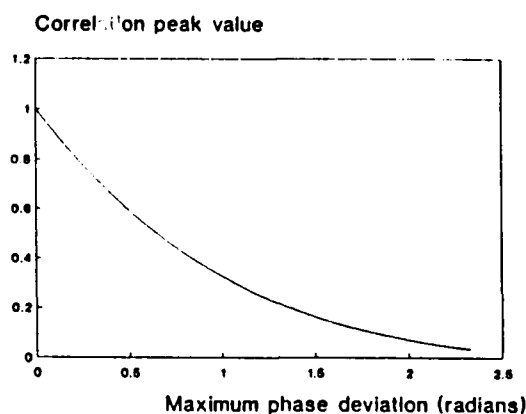


Fig. 2. Correlation peak intensity degraded by phase noise.

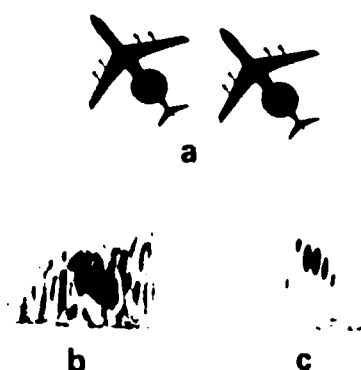


Fig. 3. Joint Fourier transform spectra. (a) A pair of input subjects with random noise. (b) Their joint transform spectrum. (c) The joint transform spectrum with phase compensation.

sponds to a phase deviation of 0.6 radians. In other words, the phase distortion of a SLM should not exceed $1/10$ wavelength, which corresponds to 0.6 radians, otherwise the correlation peak would be severely degraded. However, most SLMs do not meet this requirement.

In order to demonstrate the phase compensation with phase conjugate technique, a pair of input objects, shown in fig. 3a, is added with a random phase plate. Their joint transform spectrum is shown in fig. 3b. Notice that the spectrum is severely corrupted by the phase disturbances. However, with the phase compensation technique, the spectrum, obtained with the experimental setup described in fig. 1, is relatively free from the disturbance as shown in fig. 3c.

Fig. 4 shows the correlation spots reconstructed from these two cases. For no phase compensation, the correlation spots are heavily embedded in random noise, as pictured in fig. 4a, while with phase compensation, the correlation spots can clearly be seen in fig. 4b.

It is, however, necessary to stress the role played by the imaging lens L_1 . First, lens L_1 ensures that all the light scattered by the input objects can be directed toward the BSO crystal (assume that L_1 has a sufficiently large aperture.). Secondly, the reconstructed beam is not the exact phase conjugated beam, it has an additional phase modulation $\theta(x, y)$. Thus, it is apparent that if no imaging lens is employed, the light ray emerging from an arbitrary object point would not longer be reconstructed back at the same point. By using the imaging lens, it ensures that every light ray emerging from the objects would be reconstructed back. As long as all the light scat-

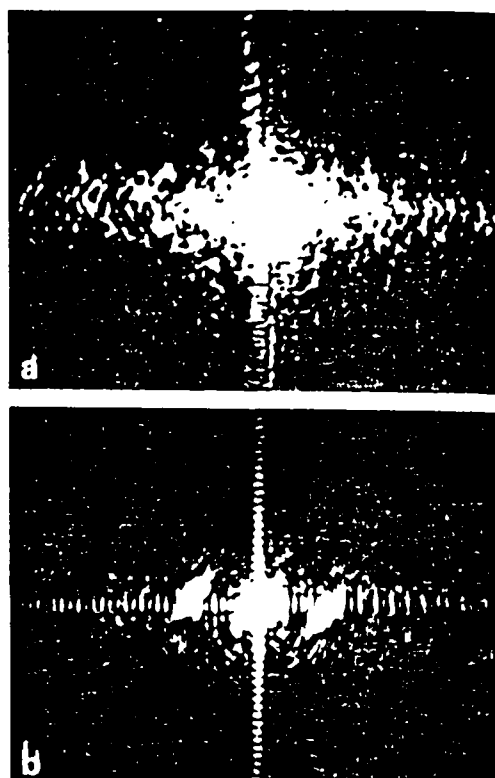


Fig. 4. Reconstructed correlation spots. (a) Without phase compensation. (b) With phase compensation.

tered by the phase distortion of the objects are collected by the aperture of L_1 , the phase distortion of the objects can be compensated by this technique. However, if the aperture is not large enough, the high spatial frequency components of the phase distortion could not be compensated.

4. Pre-encoding

The reconstructed beam, as expressed in eq. (5), is different from the object function $O(x, y)$. The additional amplitude and phase factors within the reconstructed beam can be used for object pre-encoding in a JTC, for which the correlation characteristics can be improved. These factors are dependent on object and reference beam ratio R [6], as defined by

$$R(x, y) = \frac{O^2(x/M, y/M)}{I_r}, \quad (6)$$

where I_r is the intensity of the reference beam.

The phase modulation $\theta(x, y)$ represents the phase difference between the conjugation of the object beam and the actual reconstruction beam (see expression (3)). This phenomenon is due to the interaction between the writing beams [7]. According to Vahey [8], the phase deviation between the writing beams varies along the propagation within the crystal and can be expressed as

$$\psi(z) = \psi(0) - \cotan(\phi_g) \ln \left(\frac{\cosh[Q(z)]}{\cosh[Q(0)]} \right), \quad (7)$$

where

$$Q(z) = 2\Gamma z \sin(\phi_g) + \tan^{-1} \{ (1-R)/(1+R) \}, \quad (8)$$

Γ is the coupling constant, ϕ_g is the phase shift between the writing interference pattern and the induced index grating, and $\psi(0)$ is the initial phase deviation between the writing beams. This phase variation would produce grating bending within the crystal. When a readout beam illuminates the crystal, the reconstructed wavefront from the bended volume grating would have a phase shift $\theta(x, y)$ relative to the conjugate wavefront of the object beam. From eqs. (7), (8) and (6), we notice that this phase

shift $\theta(x, y)$ is dependent on R and directly related to the object intensity distribution $O(x, y)$. Therefore the phase modulation $\theta(x, y)$ can be utilized to encode the object functions.

We have computer simulated the effects of pre-encoding the object functions in a JTC. Fig. 5 is the intensity distributions of two objects to be correlated. The autocorrelation curve (for the triangle object) and their cross correlation curve are shown in figs. 6(a) and (b), respectively. We notice that the wide autocorrelation curve and high cross correlation intensity are not desirable. However, if a phase encoding (assumed linear, that is $\theta(x, y) \propto O(x, y)$) is added to the objects the correlation characteristics are improved substantially, as shown in fig. 7, where the maximum encoded phase θ_{max} is 8 radians. By comparing fig. 6 with fig. 7, we notice that the width of the autocorrelation reduces and the cross correlation intensity decreases. Furthermore, fig. 8 illustrates how the autocorrelation width decreases monotonically as the increase of the linear phase encoding.

In view of expression (5), object encoding can also be accomplished with amplitude modulation. It is obvious that $O'(x, y)$ is proportional to the diffrac-



Fig. 5. Intensity distributions of the object to be correlated

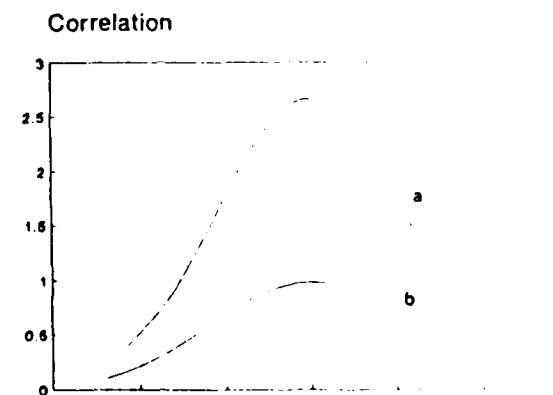


Fig. 6. Correlation without phase encoding. (a) Autocorrelation. (b) Cross correlation.

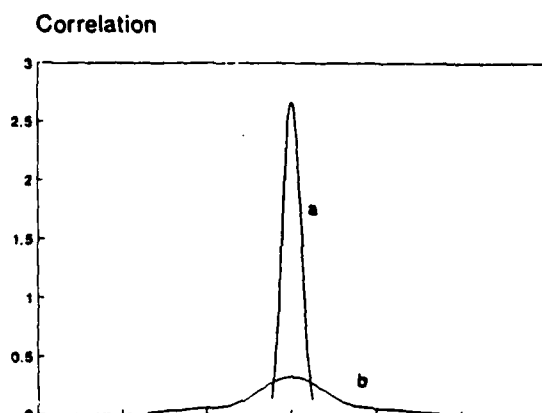


Fig. 7. Correlation with phase encoding, normalized by the cross correlation peak intensity in fig. 6. The maximum encoded phase θ_{max} is 8 radians. (a) Autocorrelation. (b) Cross correlation.

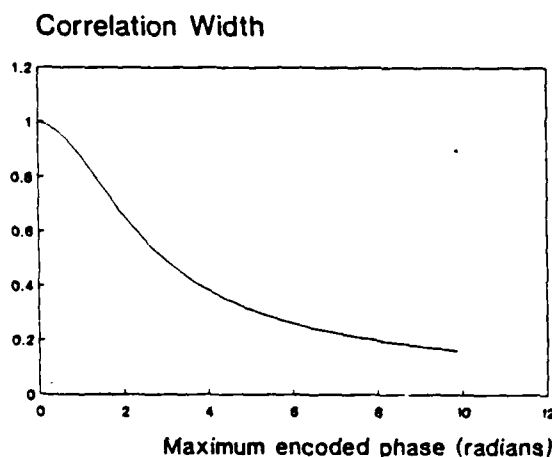


Fig. 8. Autocorrelation width (50% down width) decreases with the increase of linear phase encoding. X axis represents the maximum encoded phase θ_{max} .

tion efficiency η of the phase grating within the crystal. With reference to Ochoa et al. [6], the diffraction efficiency η of the phase grating in a photo-refractive material is related to the intensity ratio R of two writing beams as

$$\eta(x, y) \propto R, \quad R < 1, \quad (9)$$

$$\propto 1/R, \quad R > 1.$$

Thus, different amplitude encoding may be accom-

plished by controlling the intensity of the reference beam, for example, edge enhancement, which is a desirable pre-processing in a JTC [9]. Some discussion for amplitude encoding may be found in ref. [6].

5. Conclusion

Several applications of phase conjugation technique in a JTC have been investigated. It is shown that phase distortion in the input objects (due to SLM) in a coherent image processing system can be efficiently compensated by using phase conjugation technique. The additional amplitude or phase modulations produced by the nonlinearity of phase conjugation can be utilized to pre-encode the object functions, for which correlation characteristics can be improved. Computer simulations indicate that phase pre-encoded objects improve the accuracy of correlation detection, which is resulted from small autocorrelation spots and lower cross correlation intensity. This encoding technique would find application to the research of dynamic pattern recognition and robotic vision.

Acknowledgements

We acknowledge the support of the U.S. Air Force Rome Air Development Center, Hanscom Air Force Base, under contract no. F19628-87-C-0086.

References

- [1] R.A. Fisher, ed., *Optical phase conjugation* (New York: Academic Press, 1983).
- [2] J. Feinberg, *Optics Lett.* 7 (1982) 486.
- [3] C.S. Weaver and J.W. Goodman, *Appl. Optics* 5 (1966) 1.
- [4] F.T.S. Yu and X.J. Lu, *Optics Com.* 52 (1984) 47.
- [5] B. Loiseaux, G. Illiaquer and J.P. Huignard, *Opt. En.* (1985) 144.
- [6] E. Ochoa, L. Hesselink and J.W. Goodman, *Appl. Opt.* (1985) 1826.
- [7] N.V. Kukhtarev, V.B. Markov, S.G. Odulov, M.S. Soskin, V.L. Vinetskii, *Ferroelectrics* 22 (1979) 949.
- [8] D.W. Vahey, *J. Appl. Phys.* 46 (1975) 3510.
- [9] F.T.S. Yu, X. Li, E. Tam, S. Jutamulia and D.A. G. Rotational invariant pattern recognition with a program joint transform correlator, submitted to *Appl. Optics*.



MISSION of Rome Air Development Center

RADC plans and executes research, development, test and selected acquisition programs in support of Command, Control, Communications and Intelligence (C³I) activities. Technical and engineering support within areas of competence is provided to ESD Program Offices (POs) and other ESD elements to perform effective acquisition of C³I systems. The areas of technical competence include communications, command and control, battle management information processing, surveillance sensors, intelligence data collection and handling, solid state sciences, electromagnetics, and propagation, and electronic reliability/maintainability and compatibility.